12-2018

Live Load Distribution Factors and UHPC Shear Key Performance of SCDOT NEXT-D Beam

Samuel Edward Hess
Clemson University, sehess@clemson.edu

LIVE LOAD DISTRIBUTION FACTORS AND UHPC SHEAR KEY PERFORMANCE OF SCDOT NEXT-D BEAM

A Thesis
Presented to
the Graduate School of
Clemson University

In Partial Fulfillment
of the Requirements for the Degree
Master of Science
Civil Engineering

---

by
Samuel Edward Hess
December 2018

Accepted by:
Thomas E. Cousins, Committee Chair
Brandon E. Ross
Weichiang Pang

ABSTRACT

Several of the adjacent precast concrete bridge girders (APCBG) that the South Carolina Department of Transportation (SCDOT) currently use experience shear key cracking within their intended design lives. This leads to a decrease in the transverse load sharing capabilities of these sections. Shear key cracking also leads to reflective cracks developing on the bridge deck, which allows water and other corrosive agents access to the girder reinforcement.

APCBGs are often used by SCDOT for short to medium span, accelerated bridge construction (ABC) applications. Thus, SCDOT teamed up with Clemson University (CU) to seek an APCBG section that does not lead to the deficiencies the solid core, voided slab, and other APCBG sections currently used by SCODT experience. Northeast Extreme Tee (NEXT-D) girders were considered as a viable replacement to the currently used APCBG sections, and were implemented on the Hanging Rock Creek Bridge (HRB). The NEXT-D girder has proven to be successful in other states since it was first utilized in Maine in 2007. Its, wide, full depth shear key provides a robust transverse connection between the girders and its geometry makes inspection of the girder easier for state DOT officials. Additionally, utilities may be attached to the girder without sacrificing vertical clearance and it has been employed in ABC applications. The SCDOT/CU research team studied the NEXT-D girder span on the HRB to evaluate its performance.

Live load tests were conducted on the HRB NEXT-D span to evaluate the transverse load distribution and shear key durability of the NEXT-D girders. Additionally a live load test was conducted on the solid span to evaluate the shear key durability of the

solid core girders. Another purpose of the tests was to determine which (if any) of the AASHTO LRFD standard bridge sections should be considered when calculating moment distribution factors (DFM).

The NEXT-D and solid core girders in the test bridge have a 40 foot span length and utilize ultra-high performance concrete as the girder shear key fill. The live load tests consisted of crawling (< 5 mph) loaded dump trucks at several transverse locations across the tested bridge spans while simultaneously measuring bending strain, shear strain, and relative horizontal displacements in the girders. From this data, experimental interior and exterior girder moment distribution factors (DFM) were calculated for both one and two lanes loaded and compared to code-calculated DFMs, shear key deterioration (or lake thereof) was evaluated, and shear strains due to shear forces and torsion were evaluated for calculating experimental shear distribution factors.

The live load test results indicate that the solid core girder shear keys crack sooner than the NEXT-D girder shear keys under similar load conditions and that AASHTO LRFD section typology “k” be used when code-calculating moment distribution factors for NEXT-D girders. Finally, the live load test results suggest that strain transducer rosettes be used on either side of each girder web to calculate experimental shear distribution factors.

DEDICATION

I dedicate this thesis to the most important things in my life, my amazing God, my wonderful wife Jessie, and my loving family.

ACKNOWLEDGMENTS

First and foremost, I acknowledge and thank my God for His wonderful creation that we can explore and discover. I thank Him for His grace, mercy, and love for me.

I want to acknowledge and thank my advisers Dr. Cousins and Dr. Ross. I am incredibly thankful they provided me the opportunity to continue my studies at Clemson University and be a part of their research team. I appreciate the time they invested into me in building my education. Not only were they exceptional resources for this research, but they also helped me find post-graduate opportunities and demonstrated continued interest my life in addition to my work. I also want to acknowledge and thank Dr. Pang for his willingness to be on my defense committee and for his role as an educator to me.

Many others deserve acknowledgement and thanks for their help in this research. Frank Filosa was an incredible resource to me by teaching me the BDI system and by helping me better understand the project as a whole. I am appreciative of Scott Black, Carter Wertz, Sachin Sreedhara, and the Kershaw library for their help during the live load tests. I wish to thank the Federal Highway Administration and the South Carolina Department of Transportation for their role in funding my research.

Finally I am grateful for my family. I am extremely thankful for my parents for their support and love during my whole time at Clemson University. I am thankful to my wife for her love, patience, and encouragement throughout my graduate education. Without her it would have been a much bumpier “road”. For her I am always grateful.

TABLE OF CONTENTS

Table of Contents (Continued) Page

Table of Contents (Continued) Page

LIST OF TABLES

List of Tables (Continued)

Table Page

LIST OF FIGURES

List of Figures (Continued)

Figure Page

List of Figures (Continued)

Figure Page

List of Figures (Continued)

Figure Page

List of Figures (Continued)

Figure Page

List of Figures (Continued)

Figure Page

List of Figures (Continued)

Figure Page

List of Figures (Continued)

Figure Page

List of Figures (Continued)

Figure Page

Chapter 1: Introduction

According to the National Bridge Inventory (NBI), 39% of the United States' bridges exceed 50 years of age. Additionally, another 15% of US bridges are between the ages of 40 and 49, and in 2016 an average of 188 million trips were made across structurally deficient bridges daily (Bridges, 2017). Most of the nation's aging bridges were designed considering a 50-year life-span. The NBI provides a guide to the terms it uses to describe bridges and defines "structurally deficient" as "a status used to describe a bridge that has one or more structural defects that require attention" (A Guide, 2018). Within the state of South Carolina, 964 of the state's 9358 bridges are considered structurally deficient (Deficient, 2018).

In 2017, South Carolina passed a bill which raises the gas tax by a total of 12 cents in 2 cent per year intervals. With the passing of the aforementioned bill, the South Carolina Department of Transportation (SCDOT) is financially positioned to improve much of the state's infrastructure, including the state's bridge network. As part of the state's strategic plan for the next ten years, SCDOT plans to "increase the efficiency and reliability of our road and bridge network" and "focus our bridge replacement program to target our structurally deficient bridges" (Rebuilding, 2018). For many bridges, the state often employs accelerated bridge construction (ABC) techniques to quickly rebuild unsatisfactory bridges.

As a part of ABC, SCDOT will often use hollow core and solid core precast girders which are connected transversely by grouted shear keys. These girders are ideal since they can be immediately placed in the field rather than cast in place, which

significantly reduces construction time. As beneficial as these girders can be to ABC, the shear keys connecting these girders can be problematic, sometimes even soon after construction. Cracks often form at the shear key-precast interface as shown in figure 1a, which leads to longitudinal reflective cracks developing on the bridge deck as shown in figure 1b. Although initially these cracks are simple maintenance issues, they provide a route for water and deicing salts to access the mild reinforcement of the deck and girders and the pre-stressing strands of the girders.

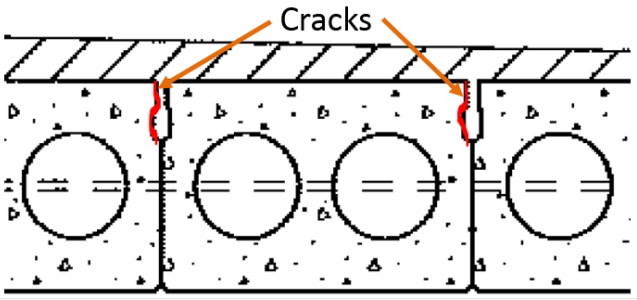

(1a)

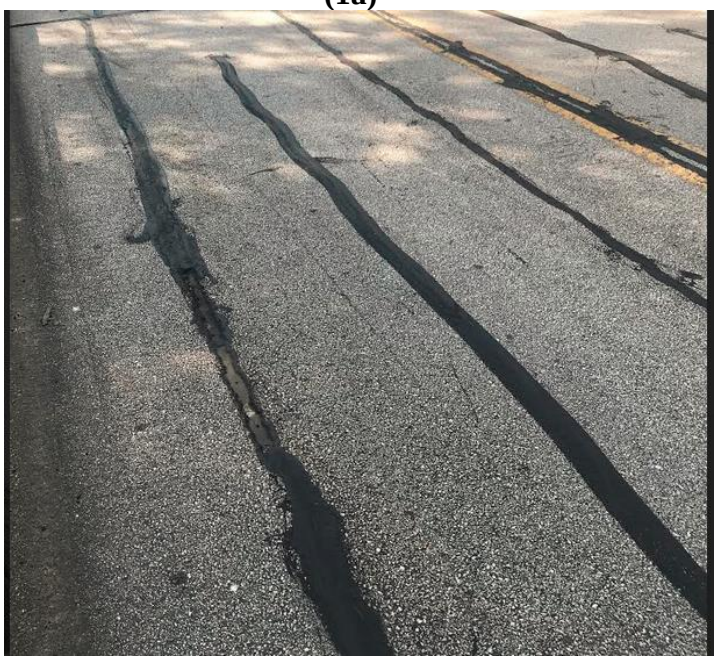

(1b)

Figure 1: (1a) displays where cracks may form at the precast-shear key interface and (1b) displays reflective cracks and reflective crack patching

Issues with shear key cracking led the SCDOT steering committee to explore a girder geometry that solves the reflective cracking problem while maintaining ABC applicability. After joining this venture with Clemson University, SCDOT settled on the Northeast Extreme Tee (NEXT)-D girder section because of its increased rotational and translational stiffness at the shear key, geometric adaptability, and ability to meet ABC among other benefits (Dreery, 2010). Additionally, several other states have begun employing the NEXT section and have observed improvement in its ability to resist reflective cracking as compared to other common girder sections employed. SCDOT is also exploring the utilization of UHPC as the "fill" for the shear key rather than traditional grout.

After determining the NEXT-D girder section as a strong candidate for short to medium span bridges, SCDOT is in need of further studies verifying its improved long-term performance, particularly at the transverse shear key. Studies are also necessary to evaluate the durability of the UHPC used at the shear key. Finally, the distribution factors of the NEXT-D girder section are not clearly defined in the American Association of State Highway and Transportation Officials (AASHTO) design code. Currently, only recommendations have been provided by a Precast Concrete Institute (PCI) technical committee and other researchers (Northeast, 2017). For this reason, further studies in transverse load distribution of the NEXT-D beam system are necessary.

1.1 Hanging Rock Bridge

The bridge selected for testing is the Hanging Rock Creek Bridge (HRB), displayed in figure 2, located over Hanging Rock Creek just south of Kershaw, South Carolina. The bridge consists of four simple spans; two 40 foot outer spans and two 70 foot inner spans. A cross section of each span is provided in figure 3. The southern outer span consists of pre-stressed solid slab girder sections and the northern outer span consists of pre-stressed NEXT-D girder sections. The inner spans consist of pre-stressed voided slab girder sections. Each span contains an asphalt overlay wearing surface varying transversely from approximately 2”-7” thick.

Figure 2: Hanging Rock Creek Bridge

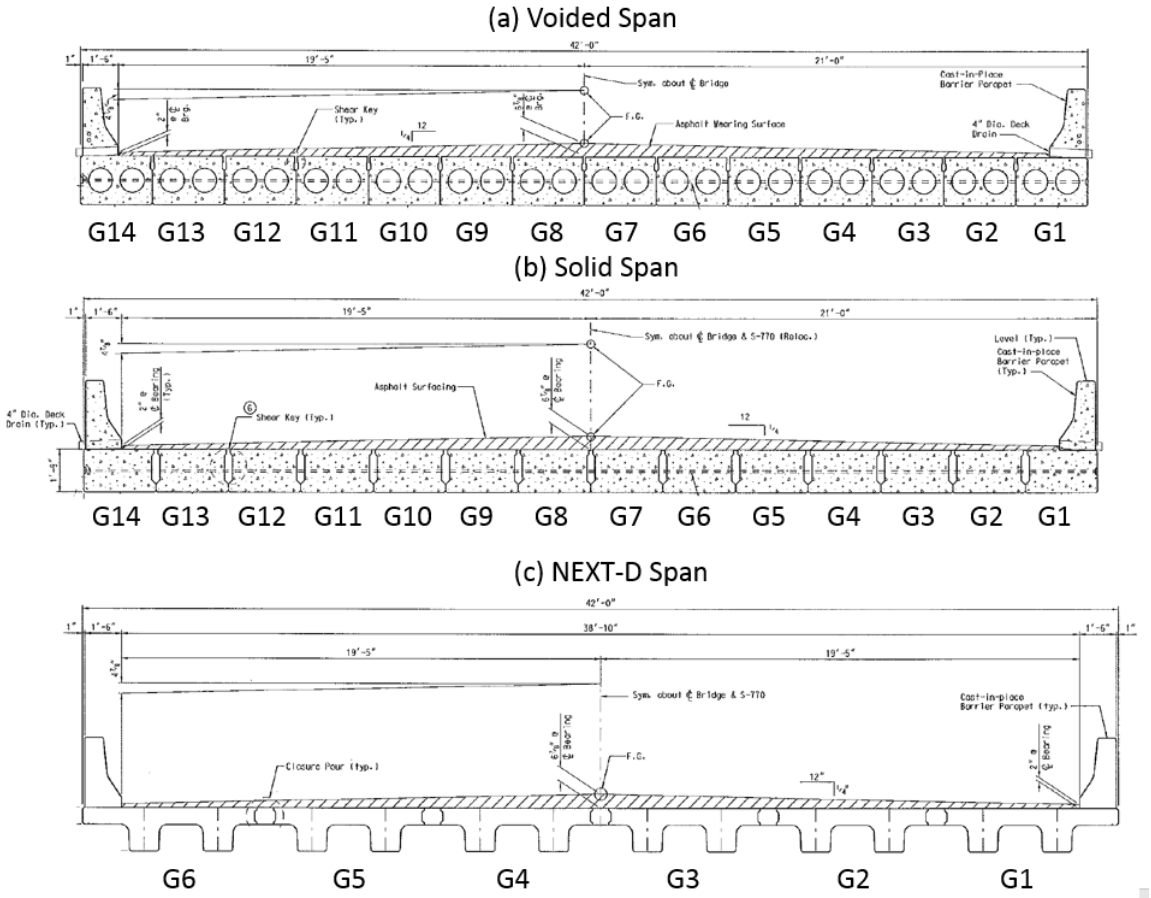

Figure 3: Cross-sections of the voided, solid, and NEXT-D spans looking north

The bridge is ideal for load testing because of its low average daily traffic (ADT), variance in girder section types, and inclusion of a NEXT-D span. This allows for live load tests to produce data conveying a direct comparison between the NEXT-D section and other sections of the bridge with little to no traffic "noise".

The girder sections of the different spans and their shear keys vary in width and depth. The voided and solid sections consist of similar geometries with the voided section containing a circular void through the middle of the section. Cross-sections of the interior voided and solid sections (girders 2-13 for both sections) are shown in figure 4. The

exterior sections (girders 1 and 14) have only minor geometric differences as compared to the interior sections and hence are not shown. The geometry of the NEXT-D section significantly differs from the voided and solid slab sections and provides some semblance of a double-tee section. Figure 5 provides a cross section of the interior (girders 2-5) NEXT-D section. Like the voided and solid sections, the NEXT-D exterior section also has only minor geometric differences from the interior section and thus is not shown. The shear key of the voided section is significantly smaller in depth than the shear key of the solid section as shown in figure 6. Neither the voided or solid sections' shear keys are over the full depth of their respective section. The widths of the solid and voided sections' shear keys are the same. The NEXT-D shear key is over the full depth of the section and the shear key width is much wider than the shear key widths of the voided and solid sections. Figure 7 displays the shear key of the NEXT-D section.

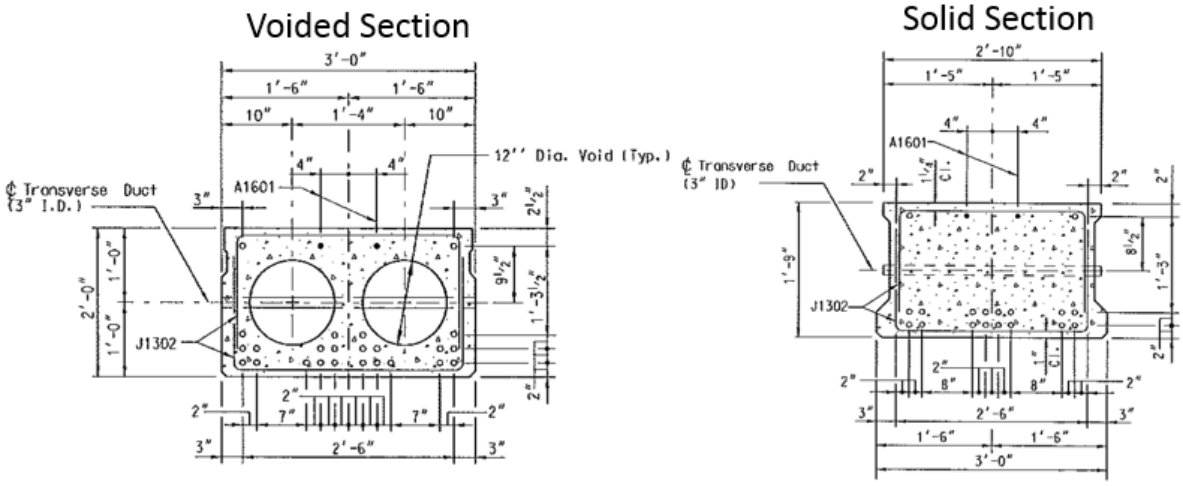

Figure 4: Interior voided and solid slab cross-sections

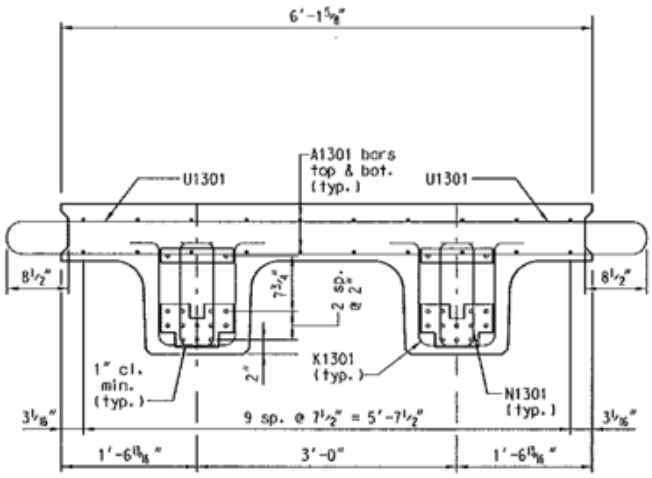

Figure 5: NEXT-D cross-section

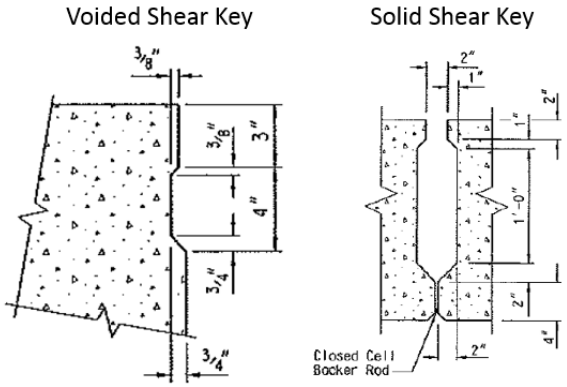

Figure 6: Voided and solid slab shear keys

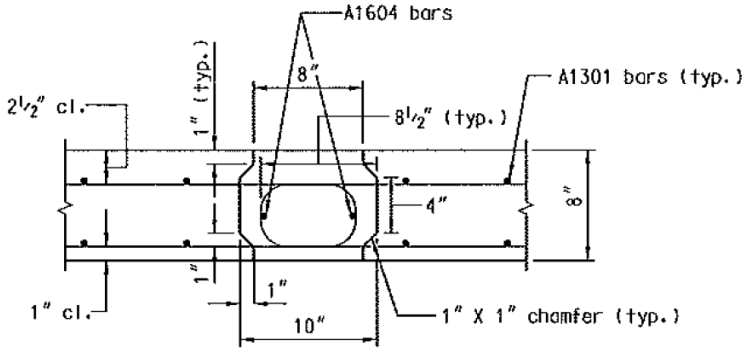

Figure 7: NEXT-D shear key

The bridge shear keys are filled with an ultra-high-performance concrete (UHPC) provided by Lafarge Ductal (a brand of UHPC) that contains steel fibers. Increased tensile and compressive strengths of UHPC significantly improve the strength and ductility of the transverse connection between the girders. The average tensile and compressive strengths of the particular UHPC mix used on the HRB were 3.29 ksi and 22.5 ksi respectively after 6 months (Filosa, 2017). Additionally, the UHPC-to-precast bond strength of this mix is approximately ten times greater than the bond strength of traditional grout. An increased bond strength improves the transverse connection by decreasing the likelihood for cracking between the UHPC and precast girder, thereby decreasing the likelihood for the bridge deck to experience reflective cracking. Additionally, the design load distribution of the girders is maintained when cracks do not form at the UHPC-precast girder interface.

1.2 Purpose and Scope

The purpose of this project is to evaluate the transverse durability of the UHPC shear keys over the first 16 months of the HRB life and to assess the transverse load distribution behavior of the spans containing NEXT-D and solid core girders. The transverse durability of the UHPC shear key is evaluated through live-load tests and continuous monitoring afforded by the Life-Span Technology (LST) sensors. The LST system provides remote long term monitoring of strains and temperatures at specific locations on a subject bridge. The load tests provide the response of the LST strain sensors under known loads and allow for a direct comparison to linear variable differential transformer (LVDT) data. The LST health monitoring system is evaluated for

effectiveness in determining the structural condition of the HRB via live load tests and a temperature-strain correlation analysis. The correlation analysis aids in determining the temperature effects on the HRB and how these effects influence the strain measurements of the LST system. This research aims to show how the LST system is used to monitor the HRB health and to provide insight into the health of the girder transverse connections at the shear keys of the NEXT-D and solid core unit on the HRB.

This research also aims to determine live load distribution factors for moment (DFM) and shear (DFV) on the NEXT-D span. The experimental distribution factors are determined via live load tests. Strain transducers are placed on the girders to aid in determining the experimental distribution factors while loaded trucks slowly (<5mph) drive across the spans tested on the HRB. Due to limited equipment, the NEXT-D girders could not all be instrumented with strain rosettes when measuring DFVs. Therefore, a calibration of the method to measure DFVs is first required.

1.3 Objectives

The following are the objectives of this thesis:

- Evaluate the effectiveness of the LST system for monitoring the condition of the HRB
- Determine if changes occur in the transverse behavior of the NEXT-D beams and the solid core units over time
- Evaluate the condition of the UHPC shear keys for the NEXT-D beams and solid core units

- Verify the DFMs determined for the NEXT-D beams during previously conducted live load tests and evaluate their AASHTO LRFD section type recommendations
- Determine the DFVs for the NEXT-D beams

1.4 Thesis Organization

This thesis is organized into five chapters. The literature review in chapter 2 surveys NEXT-D beams, experimental and code calculated distribution factors, adjacent precast bridge transverse behavior, long-term monitoring, previous live load tests, and non-destructive testing. Chapter three discusses the procedure of the research and chapter four presents the results of the research. Finally, chapter five provides conclusions and recommendations based on the results of chapter 4.

Chapter 2: Literature Review

2.1 Development and Background of NEXT Beam

The initial concept for the Northeast Extreme Tee (NEXT) beam (or girder) was based on a concrete section commonly used for train station platforms (Culmo and Seraderian, 2010). The concept was first idealized in Massachusetts and was motivated by the need for a more durable section that is compatible with accelerated bridge construction (ABC). The NEXT beam meets this objective by providing stronger transverse joints with wider, full depth shear keys, reducing transverse interfaces with larger width sections, and employing magnetic forms which allows for quick and efficient casting of different NEXT beam sizes. Additionally, other benefits of the NEXT beam includes the ability to hang utilities from a bridge without sacrificing vertical clearance and ease of inspection due to its large surface area (Dreery, 2010). Most of the aforementioned advantages are not achieved with traditional short to medium span hollow core or solid slab sections.

NEXT beam shear keys were designed to reduce cracking at the precast-shear key interface. Cracking at this interface has continued to be a significant maintenance issue for precast flat slab sections. Research has begun on stronger fill materials to be used in the shear keys to combat this problem as well.

In order to maintain ABC, several decisions and modifications were made to adjust the NEXT beam to be compatible with an expedited construction schedule (Culmo and Seraderian, 2010). The committee developing the NEXT section decided that intermediate diaphragms were not necessary. Also, a full-depth concrete slab on or as a

part of the beam was incorporated to allow for an easier connection to the abutment while maintaining the adjacent connectivity of the girders. The decision to use de-bonded strands instead of draped strands provided for the elimination of hold-downs, simplification of the forms used at precast plants (a result of the lack of hold-down forces), and implementation of self-stressing fabrication beds. Although some efficiency was sacrificed by not draping strands, the decrease in the materials required and the complexity of the beam was worthwhile to the committee developing the original NEXT beam.

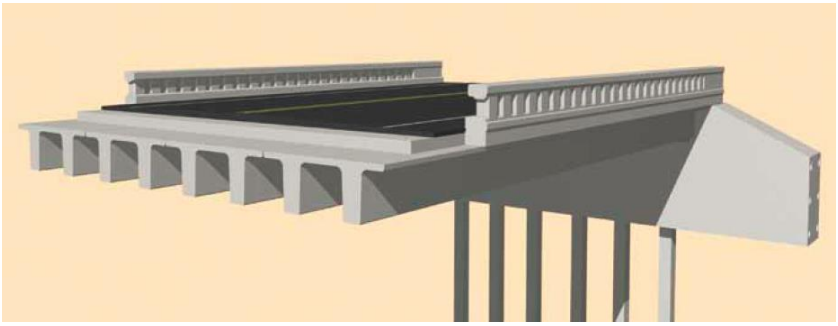

Figure 8: NEXT beam bridge concept constructed on a precast concrete integral abutment. Similar to a double-tee, each section contains two webs (Culmo and Seraderian, 2010)

The original NEXT beam was idealized by the committee to accommodate bridge spans from 45-90 feet, girder widths from 8-12 feet, and girder depths from 24-36 inches (Culmo and Seraderian, 2010). Figure 8 displays an early rendering of the NEXT beam bridge concept. When first designed, only a four inch top flange was available, however now with different types of NEXT beams, the top flange may vary in thickness. The full, top flange option has been adopted for use on short-span secondary road bridges with low average daily traffic (ADT).

The first NEXT beams fabricated for construction were used in a bridge in York, Maine in 2010. The bridge consisted of four NEXT F 36" beams (Culmo and Seraderian, 2010). Since the NEXT beam origin, several section types have been developed. Used in the first NEXT bridge as mentioned before, the NEXT F section includes an 8" cast-in-place concrete deck and best accommodates vertical curves and camber variations in members. The NEXT E section includes a 4" cast-in-place concrete deck and shares most of the benefits that a NEXT F section provides. Finally, the NEXT D section has no cast-in-place deck and is best used when ABC is essential (Seraderian, 2016).

The first NEXT beam bridge was successful and lead to the acceptance of NEXT beam construction in other states, however, further research is necessary to effectively categorize its section type in AASHTO LRFD. The section types given in AASHTO LRFD are used to determine live load distribution factors and are primarily differentiated by geometry and material. Hanging Rock Creek Bridge (HRB) in Kershaw, SC is an excellent test bridge for live load distribution factors and shear key durability. It is a four-span bridge that employs NEXT-D girders on one span and "traditional" box beams on the other spans. With low ADT, this is the selected flat slab girder bridge for SCDOT to test live load distribution factors and monitor transverse loading. Initial live load distribution factor experimental tests have already been completed by Filosa in July of 2017 and will be discussed in a later subchapter of this literature review. The cross section dimensions of the NEXT-D girder sections employed on the HRB are displayed in figure 9. Ultimately, the goal is for the NEXT beam to become a viable option for flat

slab bridge construction in South Carolina because of the decrease in construction time, the increase in durability, and the potential for economic savings.

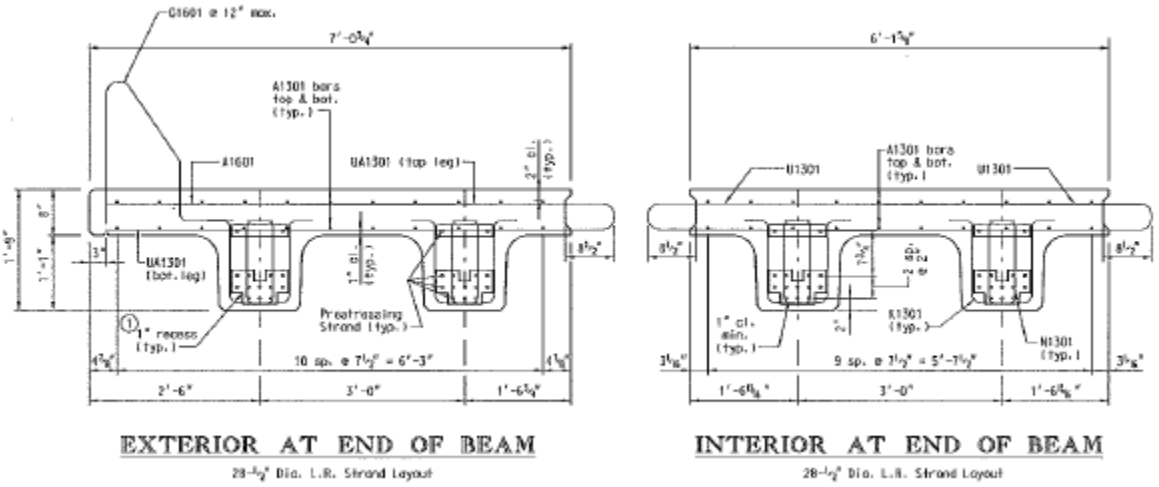

Figure 9: Hanging Rock Creek Bridge NEXT-D bridge section.

2.2 Transverse Load Distribution Factors

As live load is applied to a bridge deck, a portion of the load is imparted into each bridge girder. In theory, if a particular girder in the structure experiences ductile yielding, the other girders will support more of the load allowing the structure to be redundant. With the ultimate failure load much greater than the yield load, it seems simple enough to safely design bridge girders and begs the question: what is the need for such an in-depth analysis to develop distribution factors? The reason lies in the fact that sometimes failure may be brittle rather than ductile and that the limit states considered are often "related to serviceability and service-level loads" (Barker, 2007).

Vehicular traffic loads (live loads) are not all distributed to the girder closest to the wheel line, but rather follow the relative stiffness theory. As a result, a bridge deck distributes percentages of the traffic load to each of the girders according to relative

stiffness (Barker, 2007). The AASHTO live load distribution factors for shear and moment (DFV and DFM) are used to help determine what the maximum moment or shear an interior or exterior girder will experience. Generally, as a deck increases in stiffness the distribution factors decrease since load is more evenly distributed in a stiffer deck. The girder stiffness's also influence how load is distributed, however generally each girder in a bridge span has the same inherent stiffness. In addition to the deck, the diaphragms, barriers, bridge geometry, and other bridge components also contribute to the overall stiffness of the system and therefore contribute to how the load is distributed.

Once distribution factors are determined, they are multiplied by the maximum load effects and other various safety factors to determine the design moments and shears for the girder. The AASHTO LRFD design code provides the process for calculating the shear and moment distribution factors used to determine design loads. Next, the design load is multiplied by the dynamic load allowance factor to determine the design live load of a typical interior or exterior girder. On a bridge span, the exterior girders are located at the transverse edges of the bridge and the remaining girders are interior girders.

2.2.1 AASHTO LRFD Design Live Load Moment Distribution Factors

The AASHTO DFM calculation process will be outlined in this sub chapter for the AASHTO "i", "k", and "g" girder section types. These girder section types are shown in figure 10 (AASHTO, 2014, Table 4.6.2.2.1-1).

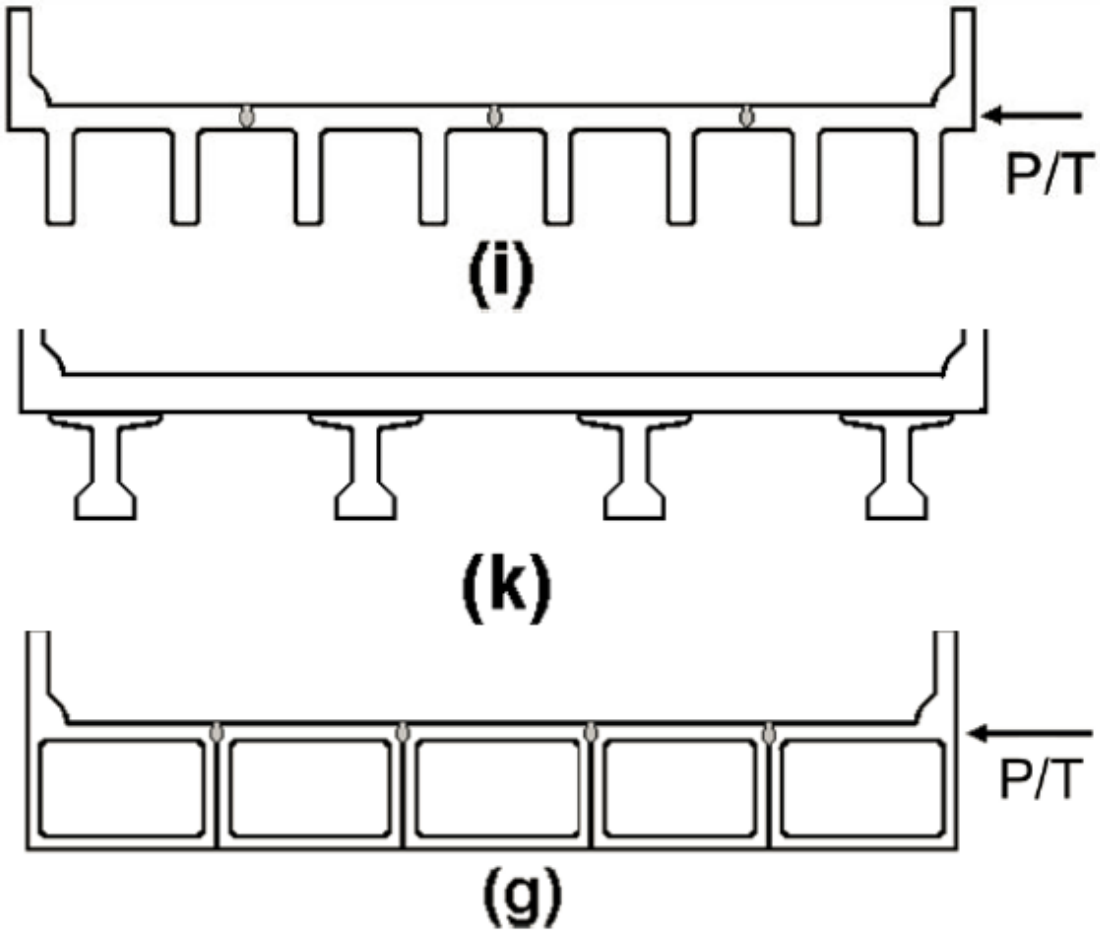

Figure 10: AASHTO section types "i", "k", and "g" (AASHTO, 2014)

The "i" and "k" girder section types are outlined in this subchapter since one purpose of this thesis is to evaluate whether girder section type "i" or "k" best represents the NEXT-D beam for design. The AASHTO type "i" and "k" sections are the PCI bridge technical committee recommended sections for NEXT beam transverse load distribution design (Guidelines, 2012). When calculating AASHTO DFMs for the Hanging Rock Creek Bridge (HRB) NEXT-D girders, the percent difference decrease from using section type "k" to using section type "i" for interior girder DFM design is 24.8% and 17.9% for

one design lane loaded and two design lanes loaded respectively. This difference leads to the reduction in calculated design moments for NEXT-D girders when considering AASHTO section type “i” vs “k”. Often moment controls girder designs, thus, if it compares reasonably to experimental DFMs, section type “i” would be the best section to consider when calculating AASHTO DFMs since it would lead to the most economic designs. The type “g” section type is outlined in this subchapter because experimental DFMs were calculated for the span on the HRB containing box girders during July 2017 (Filosa, 2017). The box girders employed on the HRB are best categorized as a type “g” section type in the AASHTO design code.

For a NEXT-D girder, to determine the design interior girder DFM using section type “i” or “k”, equations 1 and 2 are consulted in the AASHTO design code (AASHTO, 2014 Table 4.6.2.2.2b-1). Equations 1 and 2 are applicable considering section type “i” because the girders are assumed to be “sufficiently connected to act as a unit” (AASHTO, 2014). When considering section type “k”, the section properties of a single stem and the average stem spacing are considered in the calculation of DFMs. Additionally, the DFM calculated is doubled. Conversely, when considering section type “i”, the section properties of both stems of the beam and the beam spacing itself are considered in the calculation of DFMs. The final DFM is not doubled when considering section type “i”. For one design lane loaded:

$$\mathrm{GDFM_i}^1 = \quad 0.06 + \left(\frac{S}{14}\right)^{0.4}\left(\frac{S}{L}\right)^{0.3}\left(\frac{K_g}{12.0Lt_s^{\,3}}\right)^{0.1} \qquad \textbf{Equation 1}$$

For two or more design lanes loaded:

$$GDFM_i^2 = 0.075 + \left(\frac{S}{9.5}\right)^{0.6}\left(\frac{S}{L}\right)^{0.2}\left(\frac{K_g}{12.0\,Lt_s^3}\right)^{0.1} \qquad \textbf{Equation 2}$$

The variables in equations 1 and 2 are defined below (AASHTO 2014):

$$K_g = n(I_{bs}+A_{bs}+e_g^2)$$

$$n = E_{Beam}/E_{Slab}$$

K_g = longitudinal stiffness parameter for the composite girder (in^4)

S = girder spacing (ft)

L = bridge span length (ft)

t_s = depth of the concrete slab (in)

n = modular ratio between the girder material and deck material

e_g = distance between the centers of gravity of the stems and flange (in)

A_{bs} = cross sectional area of the stems (in^2)

E_{Beam} = elastic modulus of the NEXT beam (ksi)

E_{Slab} = elastic modulus of the deck slab (ksi)

I_{bs} = moment of inertia of the stems (in^4)

$GDFM_i^1$ = distribution factor for moment for one design lane loaded

$GDFM_i^2$ = distribution factor for moment for two of more design lanes loaded

AASHTO LRFD does not provide equations for determining exterior girder DFMs considering section types “i” or “k”. Instead, for calculating exterior girder DFMs for one and two design lanes loaded, the lever rule is used. The lever rule, described in AASHTO 4.6.2.2.2, is applied by assigning hinges where each interior girder supports

the deck and treating the deck as simply supported. Next, moments are summed about an interior support (girder) to find the reaction at the considered exterior support (girder). When using the lever rule, the multiple presence factors outlined in AASHTO 3.6.1.1.2-1 must be considered to calculate the factored moments. The exception for calculating exterior DFMs is considering section type "k" with two design lanes loaded if the system uses three girders, in which equation three may be used.

$g = eg_{interior}$ **Equation 3**

Where:

g = exterior moment distribution factor for two or more design lanes loaded

$g_{interior}$ = moment distribution factor for an interior girder

$e = 0.77 + d_e/9.1$

d_e = horizontal distance from the centerline of the exterior web of exterior beam to the interior edge of the curb or traffic barrier

A sample calculation for determining design DFMs of the HRB NEXT-D girders, considering section types "i" and "k", is provided in the appendix.

The interior moment distribution factors for box beams are determined from the equations for the type "g" section. To determine the interior girder moment distribution factor for the box girders, equations 4 and 5 are consulted in the AASHTO design code (AASHTO, 2014, Table 4.6.2.2.2b-1).

For one design lane loaded:

$$GDFM_i^1 = k\left(\frac{b}{33.3L}\right)^{0.5}\left(\frac{I}{J}\right)^{0.25}$$ **Equation 4**

Where:

$$k = 2.5(N_b)^{-0.2} \geq 1.5$$

For two or more design lanes loaded:

$$GDFM_i^2 = k\left(\frac{b}{305}\right)^{0.6}\left(\frac{b}{12.0L}\right)^{0.2}\left(\frac{I}{J}\right)^{0.06}$$ **Equation 5**

The variables in equations 4 and 5 are defined below (AASHTO 2014).

J = St. Venant's torsional inertia (in^4)

L = bridge span length (ft)

b = width of beam (in)

I = moment of inertia of beam (in^4)

N_b = number of girders

$GDFM_i^1$ = distribution factor for moment for one design lane loaded

$GDFM_i^2$ = distribution factor for moment for two of more design lanes loaded

It is important to consider that (I/J) can be simplified by using AASHTO table 4.6.2.2.1-3

where:

(I/J) = 0.54(d/b) + 0.16

d = depth of girder (in)

The exterior moment distribution factors for the type "g" section are determined using the equations 6 and 7. For one design lane loaded:

$g = eg_{interior}$ **Equation 6**

Where:

g = moment distribution factor

$g_{interior}$ = moment distribution factor for an interior girder

$e = 1.125 + d_e/30 \geq 1.0$

d_e = horizontal distance from the centerline of the exterior web of exterior beam to the interior edge of the curb or traffic barrier

For two or more design lanes loaded:

$g = eg_{interior}$ **Equation 7**

Where:

g = moment distribution factor

$g_{interior}$ = moment distribution factor for an interior girder

$e = 1.04 + d_e/25 \geq 1.0$

d_e = horizontal distance from the centerline of the exterior web of exterior beam to the interior edge of the curb or traffic barrier

2.2.2 AASHTO LRFD Design Live Load Shear Distribution Factors

The AASHTO shear distribution factor calculation process will be outlined in this sub chapter for the type "i" and "k" sections. For the purpose of this thesis, the NEXT-D section is the only section evaluated for shear distribution. As previously stated, the AASHTO type "i" and "k" sections are candidates for NEXT-D beam designs. The spacing when considering section type "i" is twice the spacing when considering section type "k" for calculating DFVs just as it was before in calculations of DFMs.

To determine the design interior girder shear distribution factor for the NEXT-D section, equations 8 and 9 are consulted in the AASHTO design code (AASHTO, 2014 Table 4.6.2.2.3a-1).

For one design lane loaded:

$$GDFV_i^1 = 0.36 + \frac{S}{25.0} \qquad \textbf{Equation 8}$$

For two or more design lanes loaded:

$$GDFV_i^2 = 0.2 + \frac{S}{12} - \left(\frac{S}{35}\right)^{2.0} \qquad \textbf{Equation 9}$$

Where:

S = girder spacing (ft)

$GDFV_i^1$ = distribution factor for shear for one design lane loaded

$GDFV_i^2$ = distribution factor for shear for two or more design lanes loaded

AASHTO LRFD does not provide equations for determining exterior girder DFVs considering section types “i” or “k”. Instead, the exterior shear distribution factor for the NEXT-D beam section for one design lane loaded (section types “i” and “k”) and two design lanes loaded (section type “i”) is determined using the lever rule (AASHTO, 2014). The exception for calculating exterior DFVs is considering section type “k” with two design lanes loaded if the system uses three girders. For this exception, equation three may be used, however “e” is defined differently when calculating the exterior distribution factor for shear as shown in equation 10 and d_e is as it was defined in equation 3.

$e = 0.6 + d_e/10$ **Equation 10**

2.2.3 Experimental Determination of Distribution Factors

Distribution factors have evolved significantly from the early 1990s to the factors in the AASHTO LRFD design code today. The evolution of these factors is highly influenced by experimental research which aids in the validation of these distribution factors and refinement of the finite element models that helped develop the factors.

Originally, equation 11 was used to determine distribution factors where "S" was the girder spacing, "D" was a constant dependent on the bridge type and material, and "g" was thought of as the number of lanes the girder carries (Barker, 2007). Compared to today's equations, equation 11 is quite simplistic.

$g=S/D$ **Equation 11**

Through finite element analyses conducted as a part of NCHRP project 12-26, Zoakie et al. (1991) and Nowak (1993) determined that the simple formula presented in equation 11 was not always accurate for certain bridge configurations. Through the same project, Zoakie researched additional formulas which considered more parameters, and developed methods for determining distribution factors that provide the basis for the current AASHTO LRFD distribution factors discussed in the preceding subchapter. Research included generating many computerized analyses on actual bridges and comparing those results to experimental field analyses. The most accurate computer analyses were further developed by determining the parameters that most strongly influenced load distribution. Finally, many rigorous finite element analyses (FEAs) determined the distribution factors utilized in the code today (Barker, 2007).

Although LRFD distribution factors have now far advanced, the need to experimentally test distribution factors (whether it is just a routine examination of how a bridge responds to the code factors, an examination of how a bridge behaves after a retrofit, or an examination of how a new type of bridge component behaves) strongly persists. Several methods have been used to conduct experimental tests for determining distribution factors.

2.2.3.1 Experimental Determination of Moment Distribution Factors

When calculating distribution factors for moment, the measured strain data used for the calculation is bending strain. To maximize bending strain measurements, gauges are placed on or near the bottom of tested girders.

Live load monitoring and testing was conducted on one span of the I-25 Bridge at the Dona Ana exit in Las Cruces, New Mexico. The superstructure consisted of prestressed concrete girders with sensors embedded (during fabrication of the girders) in the top and bottom flanges. The bridge was monitored for two years (beginning at the time of prestress release) for several purposes, one of which was to determine live load distribution factors. An optical fiber sensor system was used to measure strain during regular traffic loading and live load testing. Moment distribution factors were determined from the measured strains using equation 12 (Idriss, 2010).

$$GDF_i = \frac{ES_i \epsilon_i}{\sum_{j=1}^{k} ES_j \epsilon_j} \qquad \textbf{Equation 12}$$

Where:

GDF=girder distribution factor

E=girder elastic modulus

S=girder, section modulus

ε=bottom flange strain at midspan

i=ith beam

k=number of beams

In another study, external live load testing (the gauges were rigged after the construction of the bridge) was implemented on the Hanging Rock Creek Bridge (HRB) by Filosa (2017), to research how prestressed NEXT-D and solid slab beams distribute load. This project is of particular interest because it is closely related to part of the research described by this thesis in further chapters, which aims to supplement the research by Filosa. Strain transducers were used to measure the precast concrete surface strains and were oriented as displayed in figure 11 (Filosa, 2017).

Figure 11: Strain transducer orientation during live load testing of the HRB in July 2017 (Filosa, 2017)

Clemson University purchased the data acquisition system and strain gauges from Bridge Diagnostics Incorporated (BDI). The data acquisition system consisted of several nodes which were wirelessly connected to a base station. Loaded trucks were used to perform the live load tests. After live load testing was completed for one and two design lanes loaded, equation 13 was used to calculate the DFM for each girder (Fu et al., 1996).

$$g_i = \frac{\varepsilon_i}{\sum_{j=1}^{n} \varepsilon_j}$$ **Equation 13**

Where:

g_i = distribution factor for girder i

ε_i = strain experienced in girder i under a particular load

ε_j = strain experienced in all other bridge girders under the same particular load

Equation 13 is very similar to equation 12. The elastic and section modulus variables used in equation 12 can be removed in equation 13 since the girders within each respective span of the HRB have approximately the same elastic and section moduli.

2.2.3.2 Experimental Determination of Shear Distribution Factors

Just as distribution factors for moment are determined from bending strain, distribution factors for shear can be calculated considering shear strain data. Strain gauge rosettes are necessary to measure shear strain.

Using the strains measured by each gauge in a rosette, shear strain can be calculated using standard strain transformation equations (Boresi et al., 2003). Within a rosette, a diagonal gauge is intended to measure shear strain. It is virtually impossible to orient a diagonal gauge at the exact location and angle required to measure pure shear strain, therefore it is likely that bending strain and compressive strain will influence the strain measured by a diagonal gauge. This is why the other gauge(s) in a rosette are necessary to calculate the shear strain at the location of the rosette.

Several formations of rosettes have been used to measure experimental shear strain. Idress and Liang (2010) used long gauge (1 meter) fiber Bragg grating sensors in an "X" orientation, as shown in figure 12, to measure shear strains during their aforementioned live load test in Las Cruces, NM. They used the measured shear strain to calculate DFVs. They later compared these experimental DFVs to DFVs determined from a finite element model of the tested bridge and found that they closely coincided with each other.

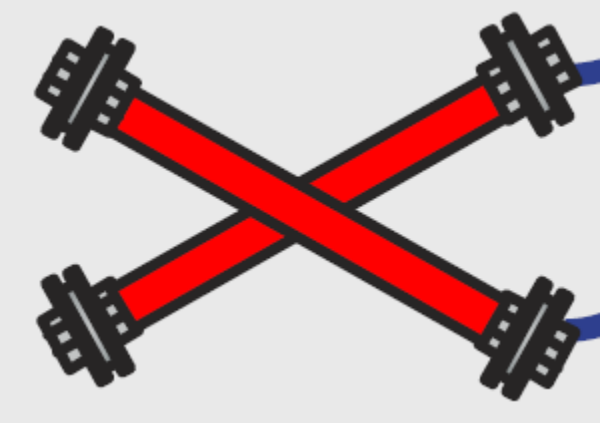

Figure 12: Rosette used by Ildress and Liang (2010)

Kassner (2012) used a rosette in an “asterisk” orientation using strain gauges and a “k” orientation using linear variable differential transformers (LVDT) to measure shear strains in order to determine the principle stresses of a subject girder within the shear span. Figure 13 shows the strain gauge and LVDT rosettes. Kassner determined that the strain gauge rosette did not provide accurate data for unknown reasons, although, the hypothesis discussed was the strains were inaccurate because the gauges were all attached simultaneously rather than allowing each gauge to cure before attaching the next gauge in the rosette. The LVDT rosette did provide enough sensible data to effectively determine the changes in principle stresses and their corresponding angles as load was applied.

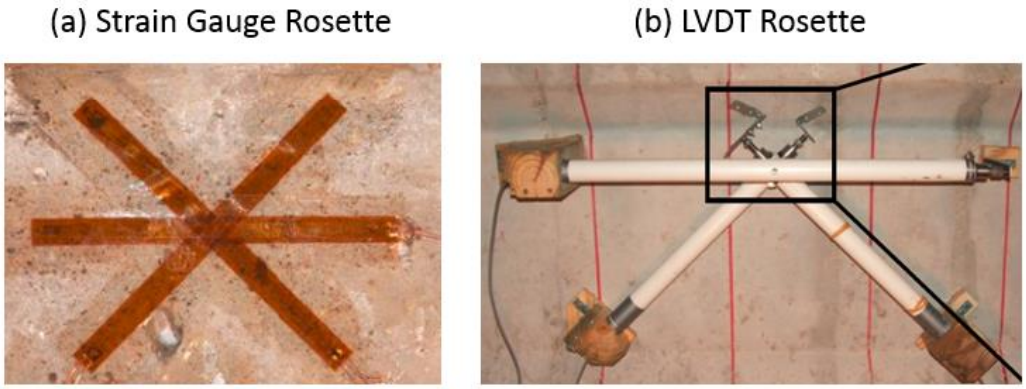

Figure 13: Rosettes used by Kassner (2012)

Dymond (2015) used a "box" rosette of foil and vibrating wire gauges, shown in figure 14, to measure the shear strain in girders as a part of bridge elastic testing in a laboratory. The reason for two horizontal gauges was to allow for linear interpolation of the horizontal strain between the two gauges since horizontal strain may vary along the depth of a beam. It was assumed the vertical strain would not vary along the length of the beam. Gauges that had previously shown similar measurements with the same loading, location, and orientation were mounted in the box rosette fashion on either side of the girder so as to eliminate the effects of torsion when measuring shear strain. Dymond determined at one location of the laboratory bridge apparatus (LBA) tested that the shear strain measured due to torsion was equal to 40% of the shear strain measured due to the vertical shear force. He also found that torsional shear increases in girders when the load deviates from their transverse center. The shear strains measured from the LBA compared well with the shear strains determined in a finite element model (FEM) of the LBA with most percent difference values within 10%.

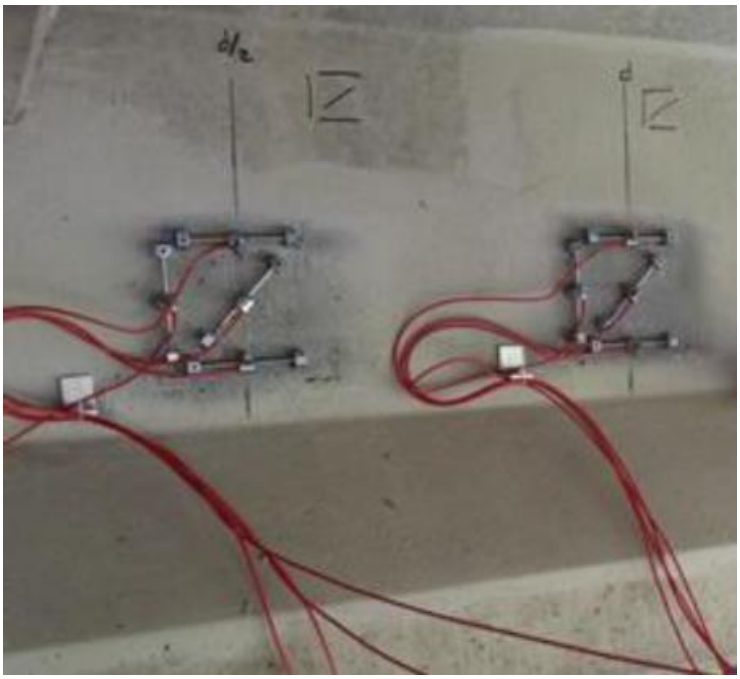

Figure 14: Strain gauge box rosette on subject girder (Dymond, 2015)

Dymond (2015) also used box rosettes to measure the shear strain of two field straight bridges. The shear strain measured was compared to the shear strain determined from a FEM. When comparisons between girder shear strains were made, Dymond was careful to compare shear strain data on the same side of the girder web between the field and FEM data so that torsion would not influence the comparison. It was determined that shear strain always compared within 9με, between the experimental and FEM data, which was generally within a 20% difference. Dymond also found from the FEM of the straight bridges tested in the field that torsion contributed to up to 9 με (a FEM was necessary to consider torsion since a rosette was not located on both sides of girders tested). Finally, Dymond mentioned that field measurements of shear strain can be challenging because of torsional effects on data and low signal-to-noise ratios in data.

2.3 Adjacent Precast Concrete Bridge (APCB) Transverse Behavior and Durability

Flat slab bridges constructed in most US states consist of slab girders connected transversely via grouted shear keys. Generally the precast girders are 3 to 6 feet wide and 1.5 to 3 feet deep. The girders share load transversely via their shear keys. The shear keys often start at the top of the girders and extend downward some partial depth of the girder. A problematic component of short to medium span flat slab bridges is the transverse connection between each girder slab. The following subchapters review the behavior and durability of these connections.

2.3.1 Transverse Behavior of Longitudinal Girder to Girder Connections

Several problematic behaviors manifest themselves at the transverse connection. Firstly, the grout in the shear keys is often prone to shrinkage cracks (Joyce, 2014). Additionally, the strength of the grout and size of the shear key often leads girders to develop cracks at the grout-precast interface. Interface cracks begin the process for reflective cracks to form on the bridge deck which can eventually lead to corrosion of the girder mild reinforcement and prestressing strands. With this level of exposure, flat slab girders cannot meet serviceability needs to their necessary potential, and although unlikely, could eventually fail catastrophically if left uninspected. As a result, researchers have begun to more closely study the poor transverse connection behavior of flat slab girders to develop streamlined solutions to the myriad of issues.

In a study by Kedar Halbe (2014) at Virginia Tech, live load (LL) tests of the Aden Road Bridge (ARB) were conducted. The results include data from sections with

similar geometries to the sections used on the solid and voided concrete girder spans of the Hanging Rock Creek Bridge (HRB). Figure 15 shows a dimensional comparison of the ARB and HRB sections. All three sections utilize transverse post tensioning.

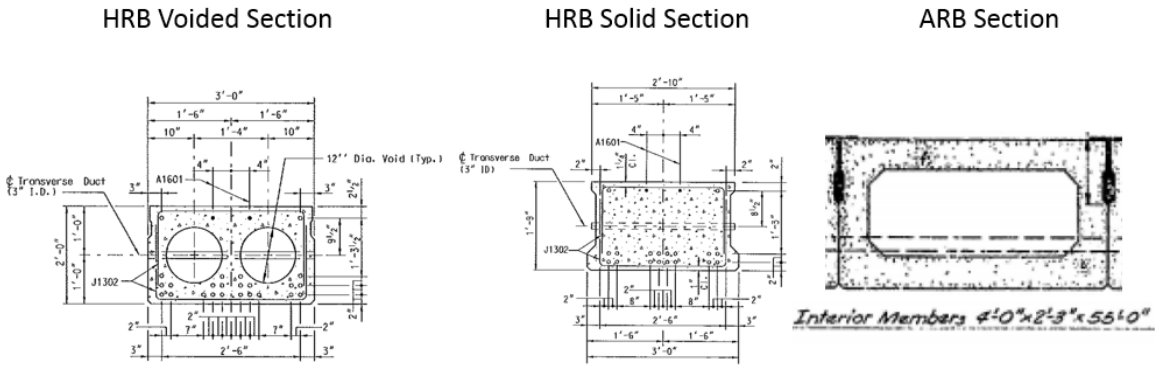

Figure 15: Dimensional comparison of HRB sections and ARB section (Halbe, 2014)

During the LL test of the ARB, many diagnostics of the bridge were collected, but of interest for this thesis is the relative horizontal gap displacements measured. These measurements allow researchers to understand the girder-to-girder connection behavior of an in-service flat slab bridge. To measure these displacements, linear variable differential transformers (LVDTs) were utilized. The three locations of the LVDTs are circled in figure 16 and their orientations are presented in figure 17.

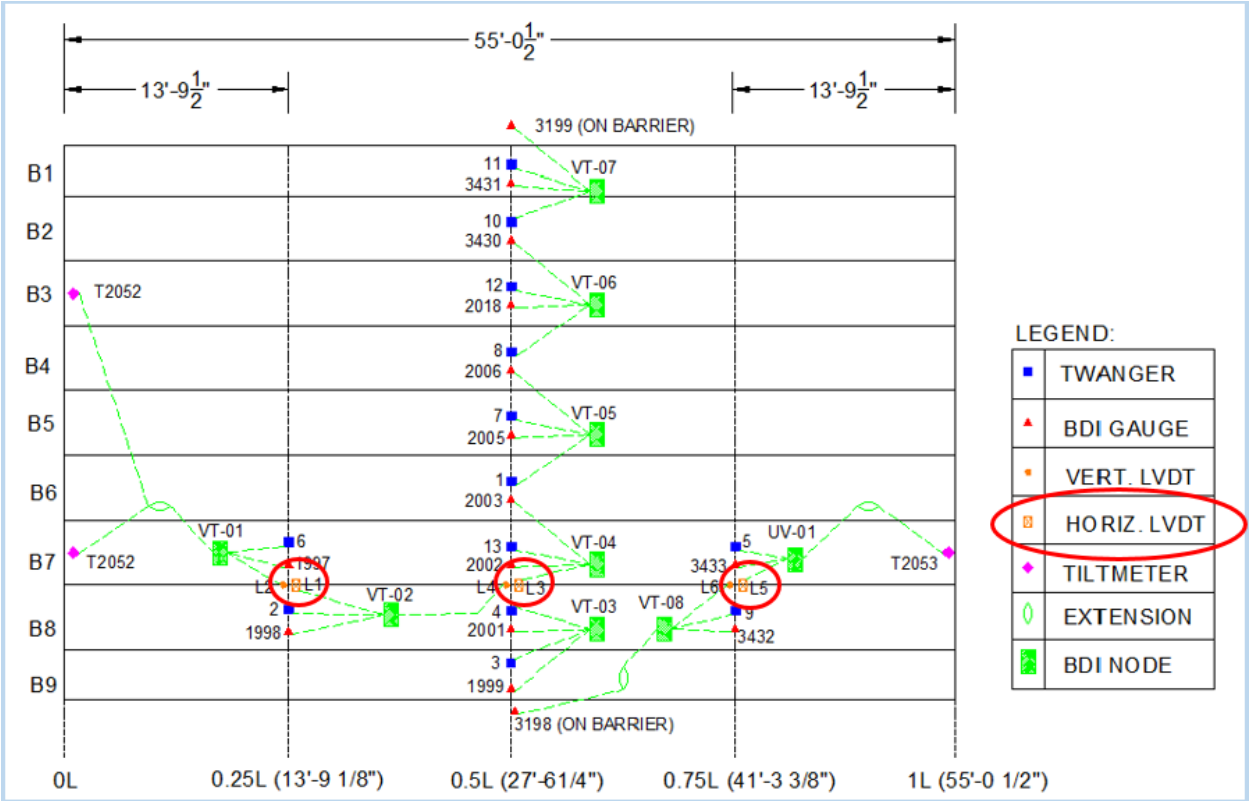

Figure 16: LVDT locations on ARB (Halbe, 2014)

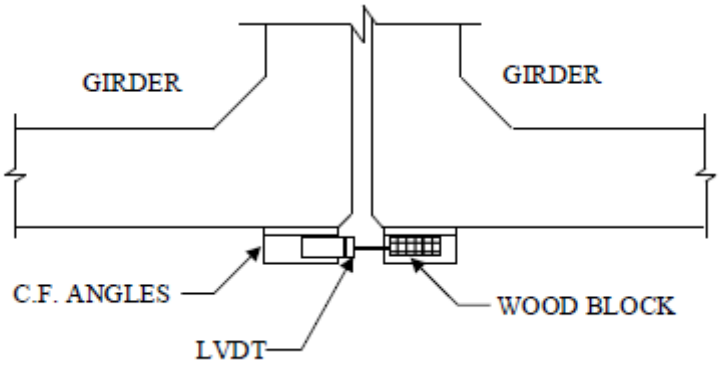

Figure 17: LVDT setup to measure relative horizontal displacements (Halbe, 2014)

Using the truck configurations presented in figure 18 for the live load test, relative horizontal gap displacements were measured.

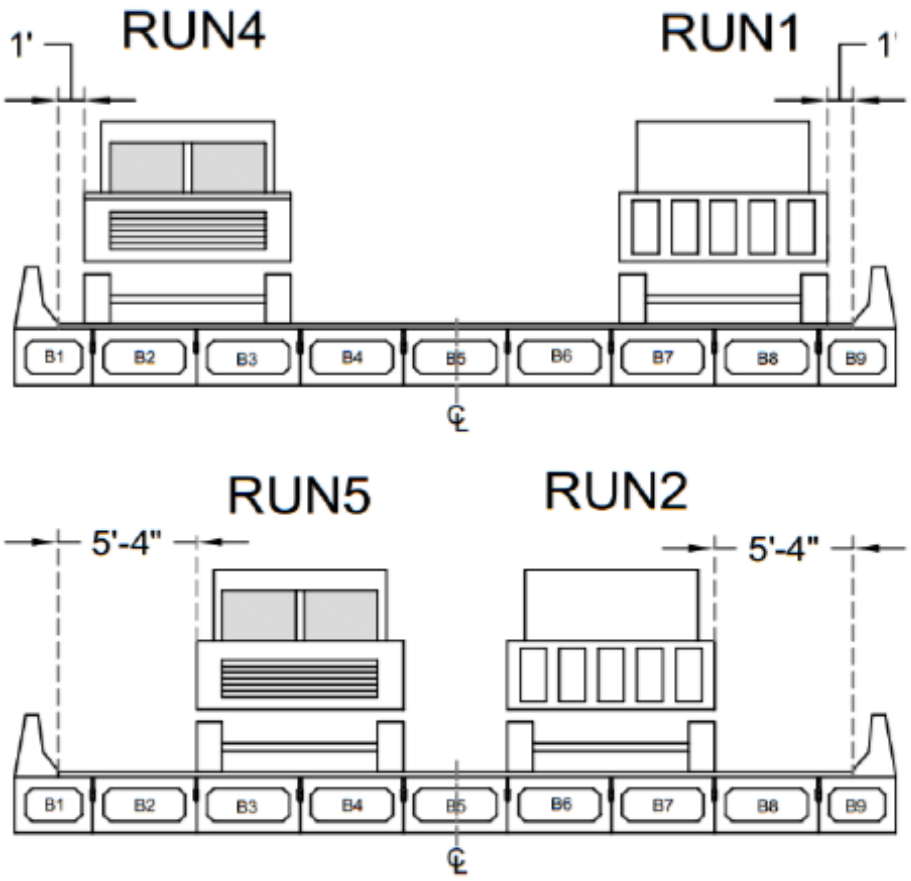

Figure 18: ARB test truck configurations (Halbe, 2014)

The gap displacements measured by the LVDTs in the ARB test are presented in figures 19-21. When the truck wheel line is transversely directly over the joint, the largest displacement is measured. Further, when the truck is away from the joint, a compressive displacement is observed (i.e. the joint closed). The observed behavior of the girder-to-girder connections provided researchers insight as to how the bridge behaves while serviceable traffic crosses the bridge.

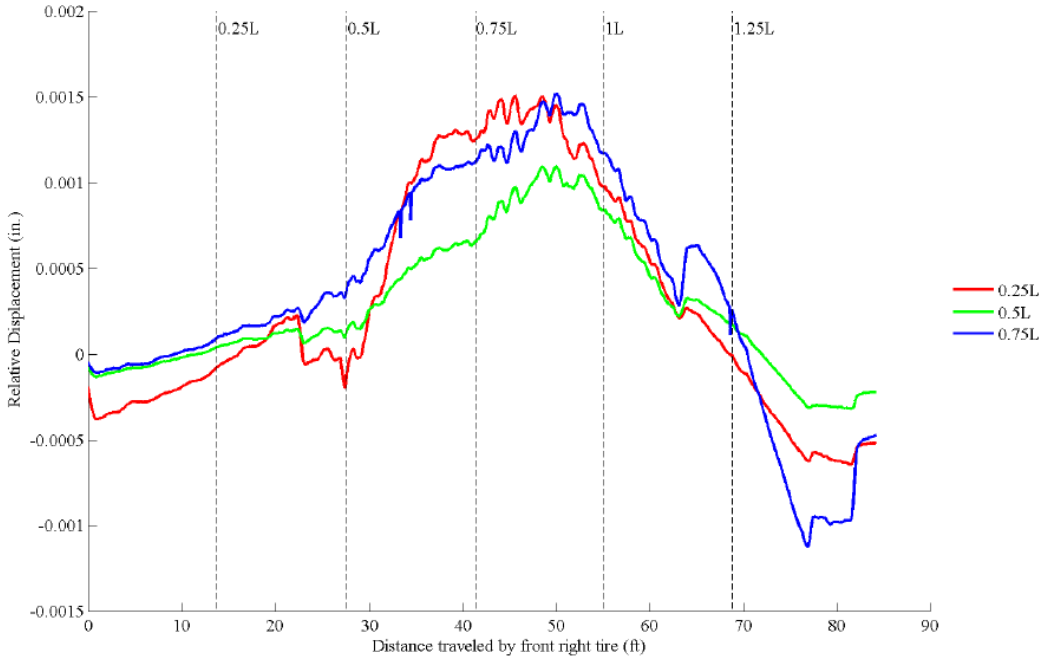

Figure 19: Typical horizontal displacements from Truck Run 1 (Halbe, 2014)

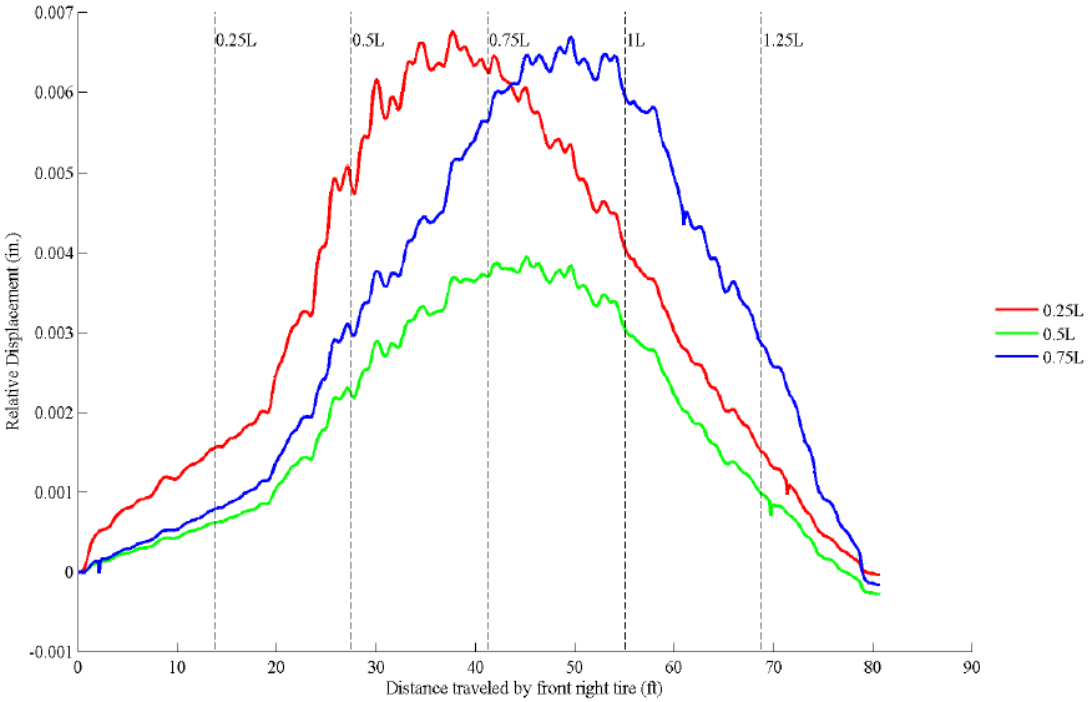

Figure 20: Typical horizontal displacements from Truck Run 2 (Halbe, 2014)

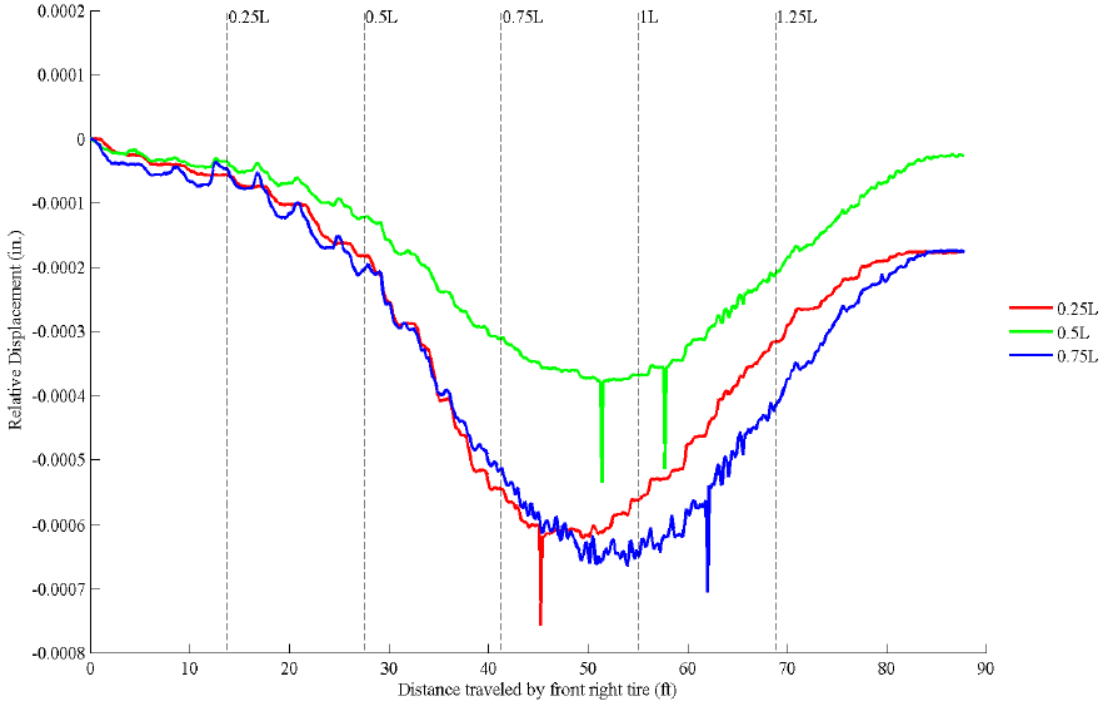

Figure 21: Typical horizontal displacements from Truck Run 5 (Halbe, 2014)

Relative horizontal displacements may be measured on the HRB as well to understand the bridge's behavior for the purpose of this thesis. Abnormal behavior on the HRB (i.e. large displacements, unexpected tension or compression in the joint) may be indicative of issues that should be further studied on the bridge. The magnitudes of the gap displacements as well as the general behavior (opening and closing of the transverse joints) of the ARB girders may be compared to the HRB solid slab girders to help determine if the HRB girders exhibit reasonably healthy behavior. Live load tests of the solid slab girders on the HRB should present similar results to the ARB live load tests due to the similar girder geometries and loadings. The NEXT-D beam behaviors will also be analyzed considering their horizontal gap displacements under load.

Researchers used sub assemblage (SA) testing models to also evaluate girder-to-girder connection behavior for flat slab bridges and to collect data providing direct comparisons between connection details. SA testing allows researchers to create specimens and evaluate these specimens as they would behave in the field. This is accomplished by creating enough specimens to capture the transverse behavior of an actual bridge and setting the specimens (which are typically 2 to 4 feet longitudinally) on steel beams which possess the stiffness and boundary conditions that allow the specimens to mimic the three-dimensional behavior of an in-service bridge.

Patrick Joyce (2014), a researcher at Virginia Tech, used SA tests to evaluate several girder-to-girder connection details' behavior and durability. The static behavior of the connections is discussed in this subchapter and the durability of the connections is discussed in the immediate following subchapter. Figure 22 shows the setup for a typical SA test.

Figure 22: Typical SA test setup (Joyce, 2014)

The specimens Joyce evaluated are presented in Table 1 and discussed for the remainder of this paragraph. Specimen 1 was a typical Virginia Department of Transportation (VDOT) shear key detail (7" depth) filled with conventional grout. Specimen 2 was the same detail as specimen 1 with the addition of Kevlar mesh reinforcement (Joyce, 2014). Specimen 3 was a detail similar to the VDOT detail with the addition of a 6" deep by 4" wide block-out to allow for transverse splice bars and allow for a large volume of UHPC to fill this connection. Very High Performance Concrete (VHPC), a mix created at Virginia Tech, was also tested as the fill for the detail considered in specimen 3. This detail with the VHPC was denoted as specimen 4. Finally, Joyce evaluated two more connections with the same details and fills as specimens 3 and 4 with the addition of a 5 inch concrete topping. These were denoted as specimens 5 and

6 mimicking specimens 3 and 4 respectively. VDOT requires for some bridges, depending on the average daily traffic of the bridge, a 5 inch concrete topping which prompted the necessity for specimens 5 and 6.

Table 1: Details evaluated by Joyce

Specimen 1	Typical VDOT Detail
Specimen 2	Typical VDOT Detail with Kevlar reinforcement
Specimen 3	Larger VDOT detail with added reinforcement and UHPC fill
Specimen 4	Larger VDOT detail with added reinforcement and VHPC fill
Specimen 5	Specimen 3 connection detail with 5 inch concrete topping
Specimen 6	Specimen 4 connection detail with 5 inch concrete topping

Joyce found that the connections with the block-outs and stronger fill (UHPC and VHPC) behaved more resiliently, displaying smaller joint openings than the typical VDOT detail under the same actuator displacement (effectively load) as displayed in figure 23.

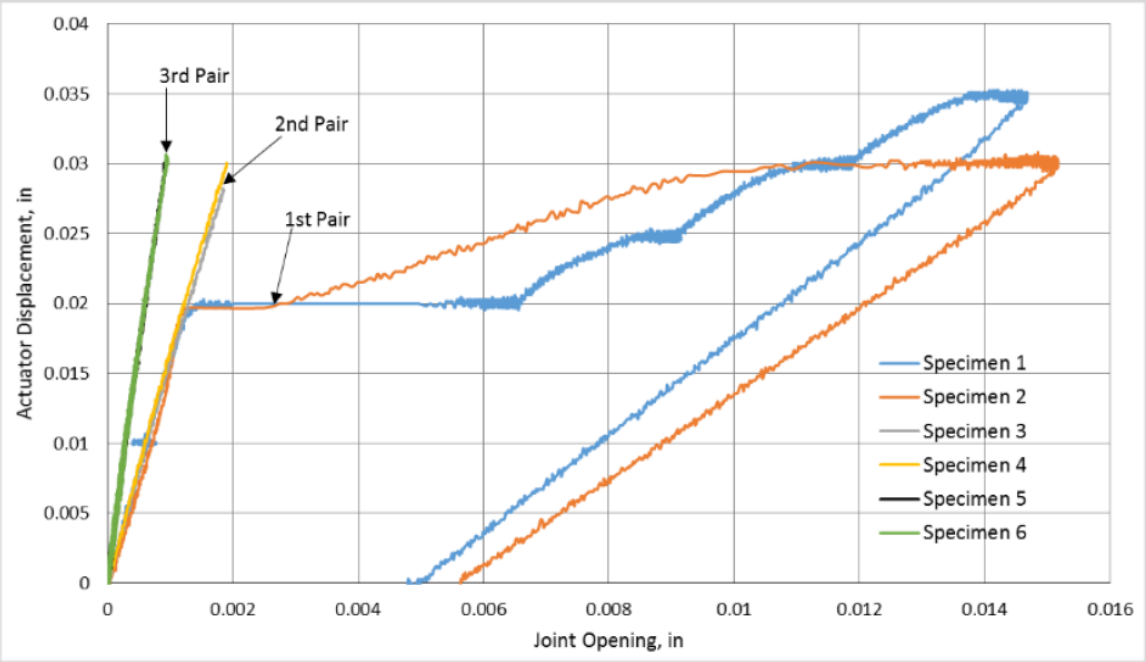

Figure 23: Connection behaviors tested in the laboratory (Joyce, 2014)

Expensive UHPC transverse connections are sometimes implemented in the field because laboratory results indicate stronger behavior, but research on the behavior of in-service UHPC filled transverse connections is limited, especially for NEXT-D girders. Data provided in the laboratory regarding transverse connection behavior may be compared to data gathered in the field, however the behaviors will likely not be exactly the same. Therefore, laboratory solutions must be tested in the field to determine if similar behavior is exhibited. Joyce developed several variations of high performance concrete solutions in the laboratory and found that this and transverse splice bars significantly improve the transverse connection behavior of flat slab girders. The girders on the HRB utilize UHPC shear key fill at their transverse connections and the NEXT-D girders have transverse splice bars in addition. This thesis will aim to determine if the

components of strong transverse connection behavior present in the laboratory manifests itself in the field through testing the HRB.

2.3.2 Transverse Durability of APCBs

The transverse durability of short to medium span US bridges has sparked the need for research as many bridges are structurally deficient due to the weak transverse connections of their flat slab girders. The durability of these bridges is tried as a result of the cycling of traffic across these bridges. The fatigue load induced by traffic weakens these transverse connections more quickly than the bridge design life because of their lack of durability. Research is ongoing to obtain a longer-lasting connection for these flat slab girders, which is currently often a partial depth shear key filled with standard grout. Several universities have begun to evaluate alternate connections at the transverse interfaces of APCB girders.

Halbe (2014) conducted SA tests of girders similar to the girders of the ARB with the aim of comparing six different transverse connection details. For the purposes of this thesis, the connection detail similar to that of the ARB connections and the connection detail similar to that utilized on the solid span of the HRB will be considered. The first connection considered (SA Test 1) consisted of a partial depth grouted shear key which mimics the shear key on the ARB. The second connection considered (SA Test 2) consisted of a partial depth UHPC shear key with a transverse splice bar connection located just above the shear key in a block out. The second connection somewhat mimics the shear keys on the HRB. A concrete topping was not included in either specimens 1 or 2.

An actuator applied a load to reach the target vertical displacement for each specimen (Halbe, 2014). Several components of the SA model were monitored, but for the purposes of this thesis just the horizontal gap displacements of the two specimens are of interest.

The SA tests were completed in cycles to monitor the fatigue of the specimens. The "baseline" tests are static tests completed during the fatigue testing. The horizontal gap displacements (denoted as "displacement") of SA test 1 are presented in figures 24 and 25.

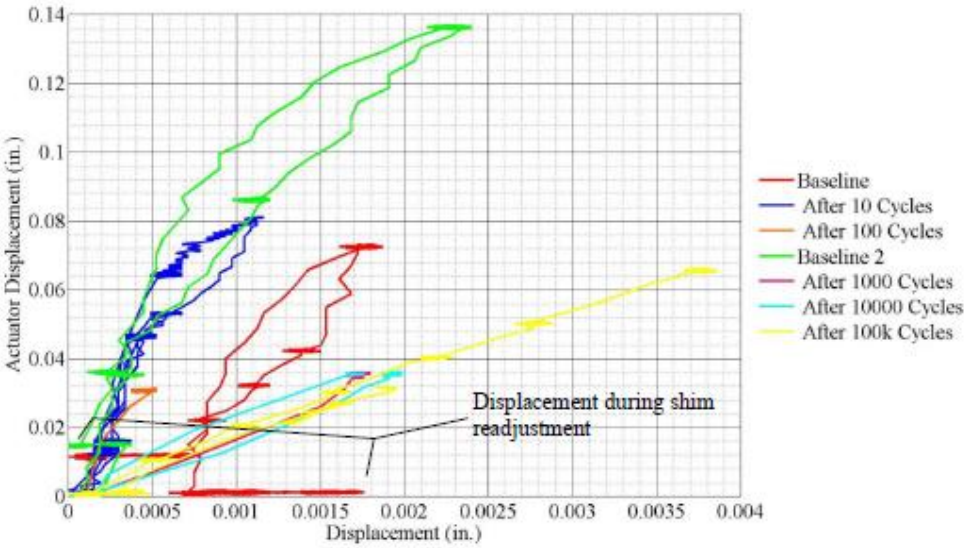

Figure 24: Variation in the northern joint displacements during fatigue testing for SA Test 1 (Halbe, 2014)

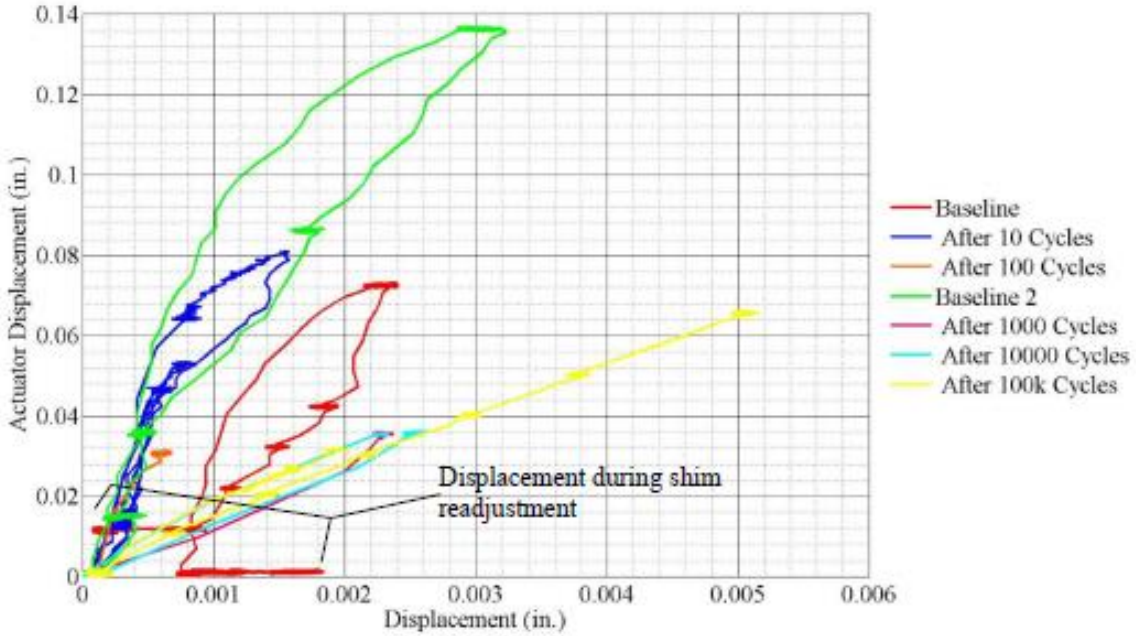

Figure 25: Variation in the southern joint displacements during fatigue testing for SA Test 1 (Halbe, 2014)

The horizontal gap displacements (denoted as "displacement") of SA test 2 are presented in figures 26 and 27. The results presented are typical of all northern and southern joints measured in the SA test 2.

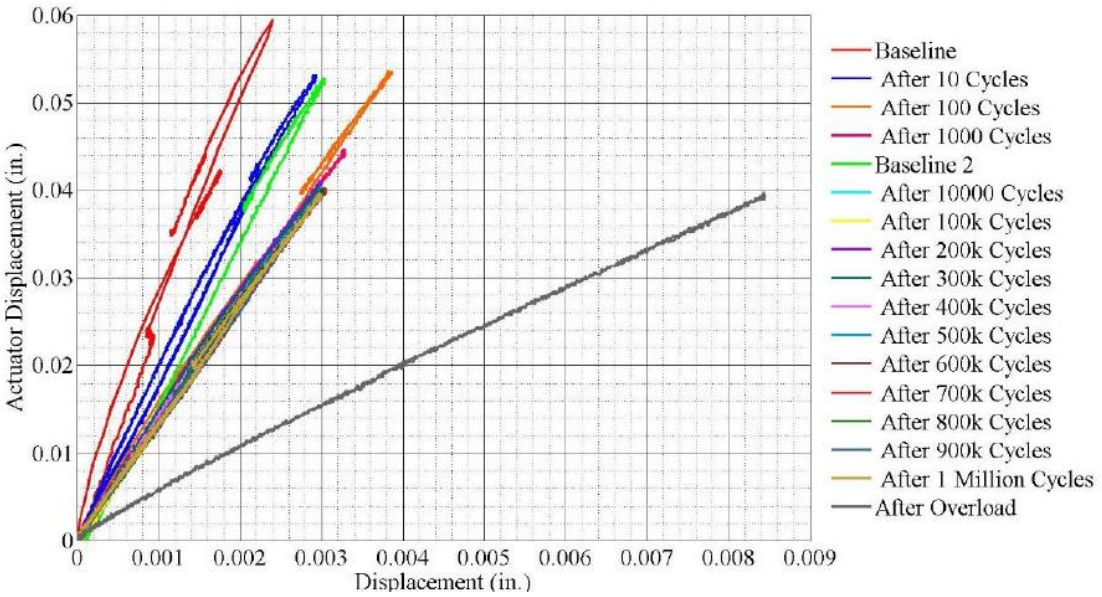

Figure 26: Variation in a northern joint's displacements during fatigue testing for SA Test 2 (Halbe, 2014)

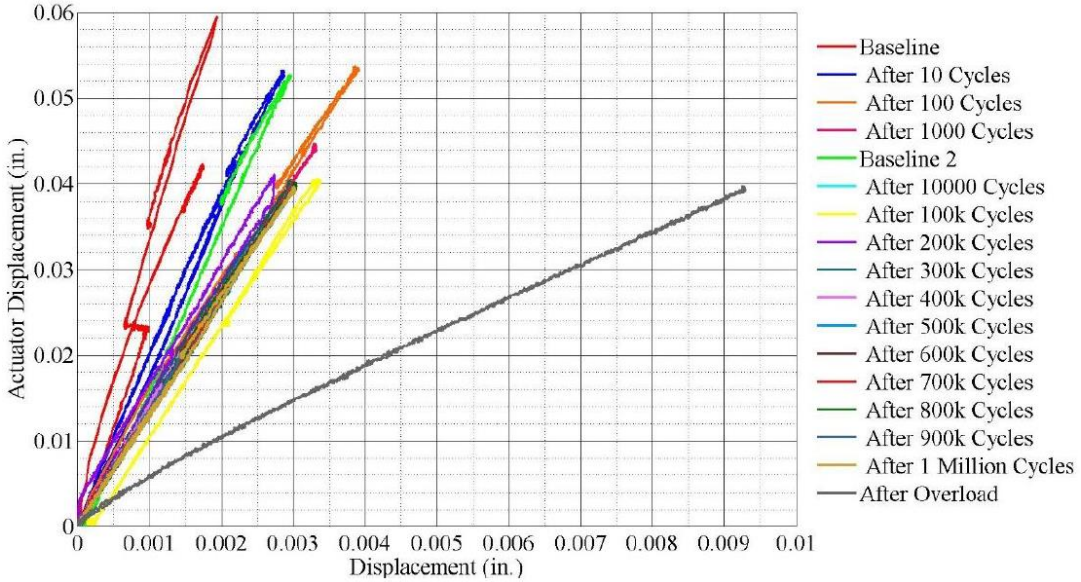

Figure 27: Variation in a southern joint's displacements during fatigue testing for SA Test 2 (Halbe, 2014)

Up to 1 million cycles of fatigue testing were performed on specimen 2 without displacements surpassing 0.004 inches as compared to up to 100,000 cycles of fatigue testing for specimen 1 displacing 0.005 inches, which displays the extensive durability of

UHPC as compared to grout. Specimen 1 could not sustain any additional fatigue tests after 100,000 cycles due to cracking. Although some of this cracking was initiated due to shim adjustments that were necessary during the testing of specimen 1, the weakness of the grout used as the fill in specimen 1 as compared to the UHPC used in specimen 2 also contributes to the durability of each joint. Finally, after initial fatigue testing was conducted on specimen 2, cracking was initiated due to purposeful overload, and a final fatigue test was run for 100,000 cycles which increased the maximum joint displacement by a factor of 2.4 (Halbe, 2014).

Joyce also found that transverse connections filled with UHPC or VHPC were more durable than grout filled connections (Joyce, 2014). Table 2 displays the results of Joyce's cyclic testing. The specimens in table 2 relate to the SA test specimens discussed in subchapter 2.3.1.

Table 2: Joint displacements before and after 1 million cycles (Joyce 2014)

	First Static Test		Post Million Cycle Static Test	
	Max North Joint Opening (in)	Max South Joint Opening (in)	Max North Joint Opening (in)	Max South Joint Opening (in)
Specimen 2	0.016	0.005	0.005	0.008
Specimen 3	0.002	0.002	0.008	0.002
Specimen 4	0.002	0.002	0.002	0.002
Specimen 5	0.001	0.001	0.001	0.001
Specimen 6	0.001	0.001	0.001	0.001

Specimen 1 is not included in this table because it could not sustain the cyclic loading without significant cracking. Specimen 2, which had a grout fill like specimen 1, developed full depth cracking to the point where only the Kevlar was sustaining the

connection. Specimen 3 was more durable than specimens 1 and 2, only developing some cracks which did not propagate for the full depth. Specimens 4-6 were the most durable experiencing minimal to no cracking during the fatigue tests.

Laboratory tests have repeatedly indicated that UHPC filled transverse connections are more durable than connections filled with traditional grout. This thesis aims in part to validate the durability of UHPC filled connections and evaluate the durability of other shear key geometries through field experimentation. Cracks forming in the transverse connections of the HRB would display of a lack in durability. Halbe's testing of specimen 2 allowed the author to learn a major indication of crack formation, namely an increase in joint displacement over time. Also, the displacement magnitudes of specimen 2 over "time" may be considered when analyzing the displacements of the HRB transverse joints.

2.4 Long-Term Evaluation of Bridge Components

Capturing and understanding long-term effects on bridges can be a difficult task. Instrumentation must be acquired for a long period of time and unwanted data, such as electronic noise, must be sifted out of data collected over many months or years. However, long term monitoring is necessary to understand how and when a subject bridge deteriorates over time. Sometimes load tests are unable to tell the whole story. One component of a bridge may become subpar due to another component's weakening. Long term monitoring allows experimenters to better understand bridge behavior which allows for more streamlined solutions to durability issues. A few methods of long term monitoring are discussed in the following subchapters.

Continuous long term monitoring in the field is difficult, therefore researchers often simulate pre-determined long-term effects in finite element models (FEM) and in laboratories to try to better understand why certain maintenance issues persist and in some cases, what long-term effects may cause failure. Adjacent box beam bridges (ABBB) are a particular area of interest for study by many state departments of transportation (DOT) and researchers because of the degrading that shear keys continue to endure. Before considering FEM and laboratory techniques, a brief review of field inspection is provided in the following subchapter.

2.4.1 Field Inspections for Long Term Evaluation

The most common method for the long-term monitoring of bridge components is field inspection. The National Bridge Inspection (NBI) program mandates states to periodically inventory, inspect, and rate all public highway bridges. The minimum requirements for these inspections are outlined in the NBI Standards which was published in 1971 (Moore, 2001). Visual inspection is a powerful tool and is the primary tool used for bridge inspection.

A survey of state DOTs, county DOTs, and contractors was completed by the US Department of Transportation Federal Highway Administration on practices for routine highway bridge inspections and published in 2001. In this study, the researchers focused on determining the composition of the inspection teams, the impact of administrative requirements on visual inspection, and the current and future use of Non-Destructive Evaluation (NDE) techniques (Moore, 2001). For the purpose of this review, just the administrative requirements on visual inspection and the NDE techniques are scrutinized.

Field bridge inspections are generally conducted once every two years (as NBIS requires) but if a bridge becomes suspect, it may be inspected more often. The inspection process is mostly determined by the inspector and previous inspection reports are permitted to be used during inspection (Moore, 2001). Surprisingly, vision tests are rarely assessed on inspectors. The quality of the reports is mostly maintained through office reviews of reports, rotation of inspectors, and field inspection programs to spot-check team's reports.

As stated before, visual inspection is the most utilized NDE technique by all agencies. Several questions were posed in the survey to determine how and when visual inspection is conducted on bridges, and the resources required to complete a thorough bridge inspection using visual inspection (Moore, 2001). It was determined that inspection units vary greatly in size, which is largely dependent on the size of the area that needs to be inspected (i.e. larger states have larger inspection units). Most members in these units are required to undergo a bridge inspection training course. The most significant components of visual inspection that those surveyed thought could be improved are the allowance of electronic data to be directly inputted into the bridge management system and the continuing education requirements for team leaders. When surveyed as to how additional resources should be used toward visual inspection, most responded that more personnel and more equipment should be acquired.

Several field techniques practiced in addition to visual inspection include Acoustic Emission, Mechanical Sounding, and Ultrasonics (Moore, 2001). A break-down

of several NDE techniques used by the survey responsive agencies is shown in figure 28. The "numbers" in figure 28 represent how many agencies responded to using the correlating NDE technique for the correlating material. A few NDE techniques were described as no longer in use including ultrasonics of pin/hanger connections, forms of pile testing, and radar. These techniques were only discontinued by a few agencies; therefore, discontinuation was not significant to the researchers.

NDE Technique	State DOT	County DOT	Contractors
Acoustic Emission			
Steel	5	1	2
Concrete	1	1	0
Timber	0	0	0
Mechanical Sounding			
Steel*	—	1	—
Concrete	32	31	4
Timber	35	19	3
Radiography			
Steel	7	0	1
Concrete	0	0	0
Timber	0	0	0
Thermal/Infrared			
Steel	0	0	0
Concrete	5	1	1
Ultrasonics			
Steel	34	0	4
Concrete (pulse velocity)	0	0	0
Concrete (impact-echo)	8	0	1
Vibration Analysis			
Steel	4	2	1
Concrete	0	1	0
Visual Inspection			
Steel	40	46	6
Concrete	38	46	6
Timber	36	46	5

*Write-in response.

Figure 28: NDE bridge inspection techniques used for different materials (Moore, 2001)

One aspect of the survey that was intriguing was the response to which bridge types require the most research for future NDE techniques. Concrete decks and

prestressed concrete superstructures were the two bridge types/components that inspectors feel have the most need for further research (Moore, 2001). Steel/concrete superstructures and timber decks/substructures were the other areas provided for response in the survey.

2.4.2 Finite Element Models (FEM) used for Long-Term Evaluation Techniques

In the particular study performed by Kedar Halbe (2014), proposed ABBB girder spliced connections filled with UHPC were studied for long-term shrinkage effects since shrinkage is a habitual contributor to shear key problems. Temperature effects on the proposed connections were studied as well. Long-term experimental monitoring was impossible for the researchers which is why a finite element analysis (FEA) approach was selected for the evaluation of the connection details.

FEMs were designed to simulate the behavior of these connections under stresses exhibited from shrinkage effects. Specifically, the bond (a perfect bond was assumed) at the interface of the beam and connection at the shear key was examined under these stresses. ABAQUS was the software selected to create the FEMs necessary, but this software is unable to detect cracks or determine the age at which cracks form, which is why just the stresses from shrinkage effects were studied.

Since shrinkage cannot be directly inputted as a load in ABAQUS, a method adopted by Sharpe (Sharpe, 2010) of applying a uniform temperature change to simulate the effects of worst-case shrinkage strains was selected by the researchers. The results of the shrinkage models displayed that “UHPC connections can be susceptible to cracking at

the interface due to differential shrinkage" (Halbe, 2014). A schematic of the stresses in the joints modeled after shrinkage loads were applied is presented in figure 29.

Figure 29: Schematic of joint stresses after shrinkage loads were applied (Halbe, 2014)

The researchers chose a simplified analysis of differential shrinkage since the FEM did not consider reinforcement, tensile creep, and other factors that contribute to shrinkage, but they were also not necessary. This is because it was concluded that the connections are durable in the long term regardless of interface cracking that may occur due to shrinkage. The defense for the resiliency of these connections lies in the fact that the range in the widths of the cracks (0.0009 in to 0.0127 in) that may form due to shrinkage are less than the AASHTO 2013 requirements, thereby allowing the connection to be considered durable in its resistance to shrinkage over a long period of time.

Temperature effects were simulated in ABAQUS as well (Halbe, 2014) The parameters required for the model (such as temperature gradients and temperature values) were acquired using the AASHTO design code, and using the state of Virginia for

determining location specific parameters from the AASHTO code. In addition, other public published papers were used as sources for parameters that were to be assumed. After the analysis was completed it was determined that temperature affects were not obtrusive to the system.

In summary, Halbe determined that a crack would almost definitely form at the beam to UHPC interface due to shrinkage, and therefore chose to monitor whether this crack would violate AASHTO requirements with the proposed connection types. It was determined that the new connection details considered would be sufficient for the long term in their resistivity to shrinkage and temperature effects. The Hanging Rock Creek Bridge (HRB) also utilizes UHPC to precast bonds at its transverse connections. A FEA of the shrinkage effects on the HRB is not in the scope of this thesis, but after considering Halbe's study of UHPC to beam interface bonds, it is likely that shrinkage effects at this bond on the HRB are minor.

2.4.3 Lab Simulations Used as Long Term Evaluation Techniques

Another method used to study long-term effects on bridges is to simulate the effects in a laboratory. Graybeal (2010) used the lab simulation method to study the long-term fatigue effects from truck wheel loadings on ultra-high performance concrete transverse connections in highway bridges.

To complete the transverse testing, four test specimens were created with each specimen consisting of two precast panels connected transversely using NYSDOT connection details and UHPC as the closure pour. In figure 30 shown below, one test specimen set-up is displayed.

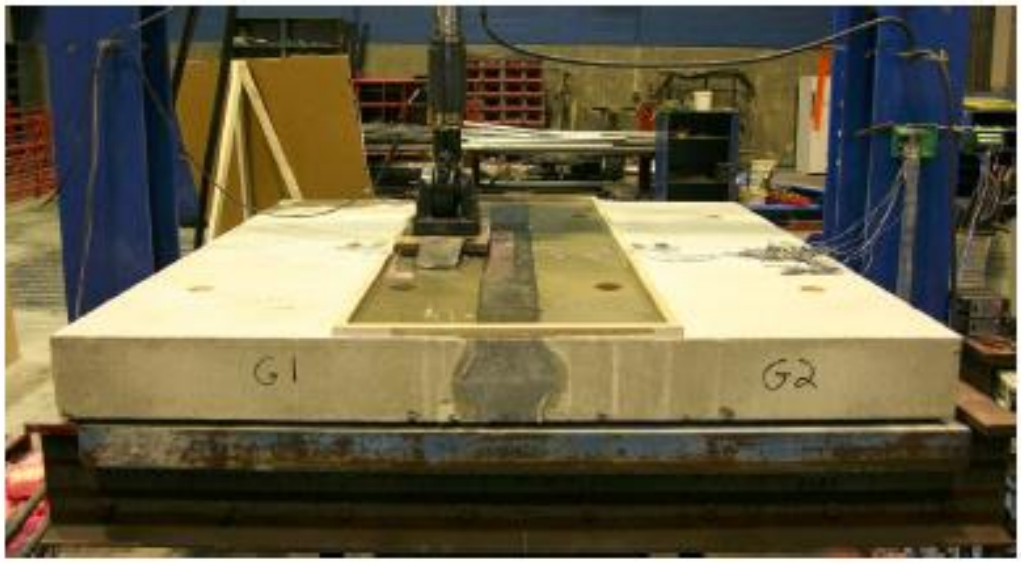

Figure 30: One of four transverse test specimens. G1 and G2 represent the two precast girders and the darker concrete between the two precast girders is the UHPC closure pour (Graybeal, 2010)

Cyclic loads were applied to the connection to simulate fatigue induced loads on the UHPC connections from continual truck wheel loadings (Graybeal, 2010). A load was applied to produce 100 microstrain which induced tension in the transverse joint. This was used conservatively as the upper limit produced from a service truck load. Monitoring techniques of the specimen for damage during the loading cycles included visual assessment of the concrete cracking, electronic monitoring to analyze the strain distribution and flexural stiffness, and leakage monitoring to analyze interface (precast to UHPC) debonding. If no damage appeared within the first 2 million cycles the load was increased by a factor of 1.33 and monitored for 5 million more cycles.

After the cyclic load testing was completed, the researchers determined that the precast to UHPC bond had not failed since no significant cracking occurred at the bond (Graybeal, 2010). Figure 31 displays the cracks that developed after the loadings in

which every crack runs perpendicular to the bond. The cracks in red were visually inspected with the naked eye and the cracks in blue were determined using volatile alcoholic spray. No cracks indicating joint debonding were evident.

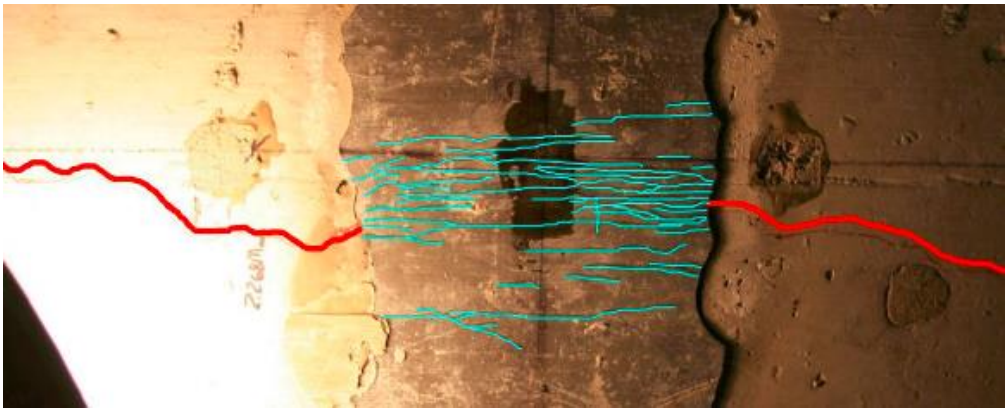

Figure 31: Cracking observed at tested joint (Grabeal, 2010)

The displacement results during the fatigue loading are plotted in figure 32. These displacements are likely larger than what would be measured in a live load test since the loading is fully maximized in the laboratory for an in-service truck which is difficult to do in the field. Strain per applied load measured during testing indicated that the UHPC is effective in distributing the load over the long-term since the researchers found the tensile strains to be mostly constant throughout the cyclic loading (Graybeal, 2010). This laboratory test indicates that fatigue service loads should not create debonding at transverse joints where UHPC is utilized as one of the bonding concretes, however, it is important to conduct long-term tests in the field via live loading to verify what laboratory tests have determined. Considering the consistency of strain and displacements over time will also aid in evaluating in-service joints on the HRB for debonding.

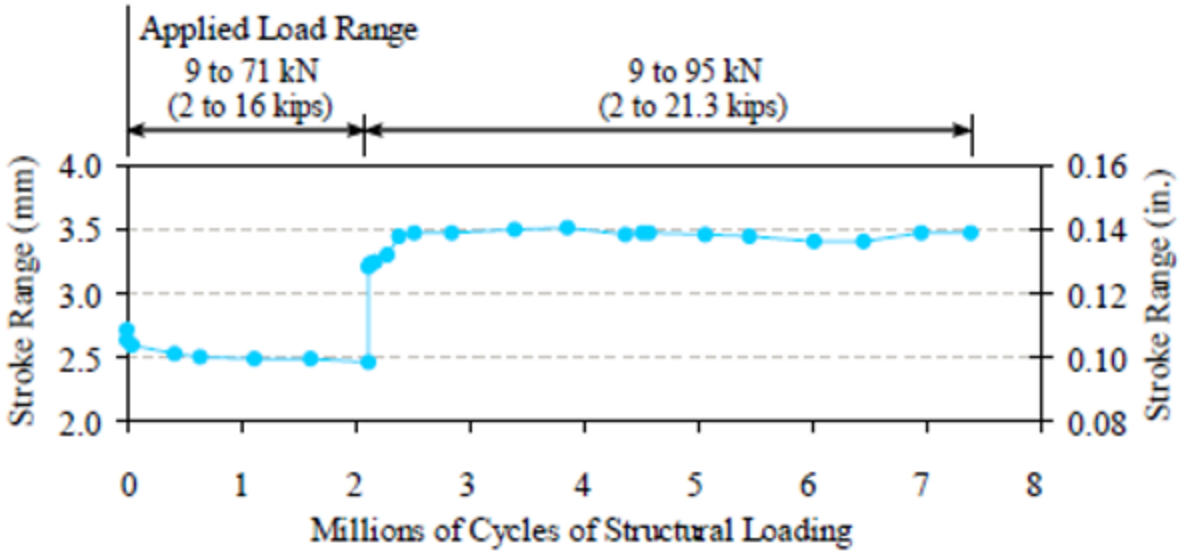

Figure 32: Displacements measured during cyclic fatigue loading (Graybeal, 2010)

In another lab simulation to analyze long-term effects, Sheng (2013) performed a simulation of cyclic loads on a proposed shear key detail by applying a sine-wave load to determine how the shear key would endure the long term effects of continual loading. This fatigue test was one of many tests applied to the shear key but is the primary test performed to analyze the shear key's durability over its expected service life.

The experimental specimen created was based on a shear key configuration proposed by PCI Northeast and is displayed in figure 33. Strain transducers, strain gauges, linear variable differential transformers, and string pots were all used to monitor the strain distributions through the shear key thickness, measure the specimen deflection, measure the relative rotation of the shear key with respect to the precast pieces, and measure the potential opening of the interfaces between the precast and shear key material during the fatigue tests. The specimens were loaded with the intention of capturing critical moment-shear ratios. A high shear test and a high moment test, as

shown in figure 34, was performed. Different mixtures of Quikrete Non-Shrink Precision grout, water, and Nycon-PVA-RECS15 fibers were tested as the shear key material (Sheng, 2013).

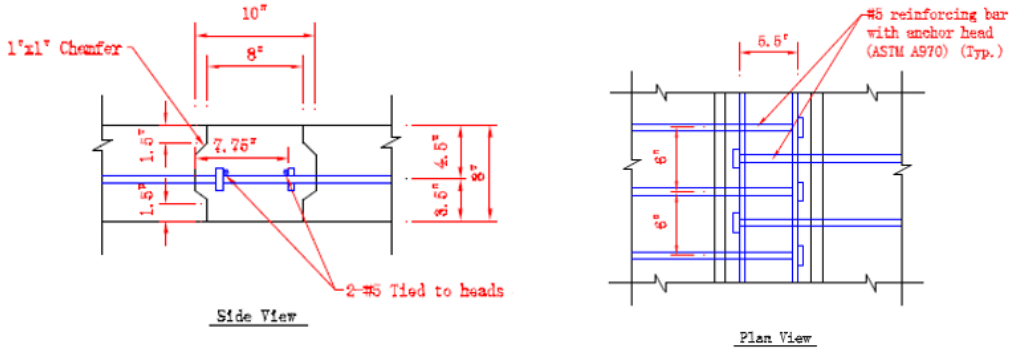

Figure 33: Shear key configuration (Sheng, 2013)

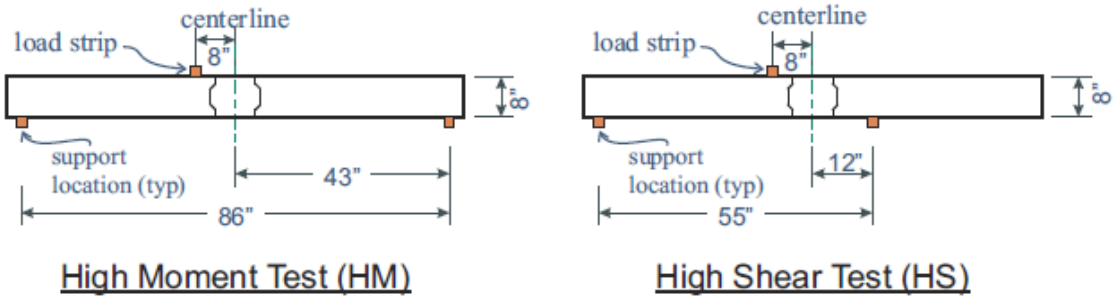

Figure 34: Loading configuration to test the shear key (Sheng, 2013)

It was determined that 10 million cycles were necessary to capture the shear key performance over its service life. The fatigue tests took approximately 25 days, and then another 2 million cycles were applied with a water pond above a shear key specimen to test for leakage.

MTS software was used to conduct the tests. The fatigue critical load levels for the high moment and high shear tests were determined by applying the design truck load specified in LRFD Art. 3.6.1.2.2 (AASHTO, 2012) with a constant spacing of 30 feet between the two 32 kip axles. Various factors from the AASHTO LRFD design code were applied to the fatigue loadings to determine the final fatigue load levels, and the shear key stiffness's were determined from previous static tests and finite element models. The fatigue loads that were required and the fatigue loads that were applied during testing are listed in Tables 3 and 4 (Sheng, 2013).

Table 3: Fatigue loads required (Sheng, 2013)

ID	Stiffness from Static Test		Stiffness in FEM		Fatigue Load	
	K_t (k/in)	K_r (k-in/rad)	K_t (k/in)	K_r (k-in/rad)	$IM = 1.33$	$IM = 1.75$
FAT-01	376.5	83879.0	56.5	12581.9	5.20	6.85
FAT-02	575.9	581473.5	86.4	87221.0	7.07	9.31
FAT-03	420.0	100000.0	63.0	15000.0	5.49	7.23
FAT-04	550.0	117890.0	82.5	17683.5	7.94	10.45

Table 4: Fatigue loads applied (Sheng, 2013)

Specimen ID	Load level Applied (Cycle/million)				
FAT-01	8.7(10.6)				
FAT-02	8.7(5.9)	9.7(4.1)			
FAT-03	4.9(1.8)	6.5(0.4)	5.4(0.4)	5.6(4.2)	7.3(3.3)
FAT-04	8.1(5.0)	10.6(5.0)			
FAT-01(redo)	5.3(5.0)	7.0(5.0)			

After running the simulation, the leakage tests did not indicate that any cracks had formed in any of the specimens. To determine crack formation from the strain transducers, the experimenters looked to see if there was a sudden drop in strain on any of the strain transducer readings. This is because at a tensile point in the bond of a shear

key, cracking allows for stress relief which corresponds to a reduction in strain. (Sheng, 2013). The strain transducer data showed that two of the specimens experienced minor cracking at the bond interface although it was not serious. The other two specimens did not experience interface cracking at all.

The shear key detail tested is very similar to the shear key utilized on the NEXT-D span of the HRB. This detail was proven to be excellent in the laboratory but must also be tested in the field to confirm its strong performance through long-term testing. Also of significance to the author, from the research conducted by Sheng, is the observation that a sudden reduction in strain is a major indicator of cracking. This important observation will be considered throughout the testing of the HRB transverse joint to aid in determining if its long-term behavior is indeed resilient.

2.4.4 Long Term Evaluation Using Life-Span Technology (LST)

LST sensors have been used for the past 10-15 years to perform long term monitoring of bridges. The bridge sections monitored thus far have mostly used LST sensors to monitor strains and temperatures at critical bridge locations. Many different girder systems and material types have been monitored. One such bridge that employed LST sensors is the I-80 Bridge over Canoe Creek.

This project utilized the LST system and other sensing technology to monitor for seven months fatigue prone details at fracture critical locations of its steel superstructure (Hartle, 2006). Acute inspections may be assigned to bridges, but inspections are quite costly and do not always address fatigue prone details. These details are the focus of the long-term research performed on the I-80 Bridge over Canoe Creek.

The field condition-monitoring system implemented on this bridge consisted of 20 LST dual channel sensors which measured both peak and active tensile strains (Hartle, 2006). In addition, three PZT sensors were installed to detect anomalies, and four temperature sensors were installed to measure ambient temperature changes. The system also included a data collection system and a data acquisition controller which sends data to the secure Network Operation Center (NOC). Interrogation of each sensor was conducted at a frequency of 1x per minute and uploaded to the NOC eight times per day.

Figure 35 shows the bridge on which research was conducted. Figures 36 and 37 display a representative example of the location and orientation of the LST sensors utilized during testing.

Figure 35: I-80 East-bound bridge on which research was conducted (Hartle, 2006)

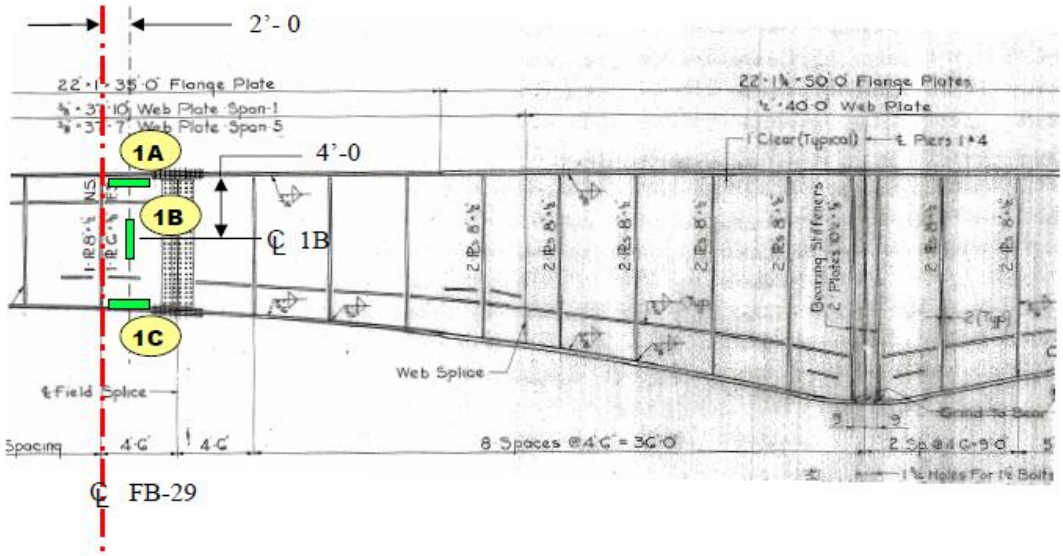

Figure 36: Example location of LST sensors (Hartle, 2006)

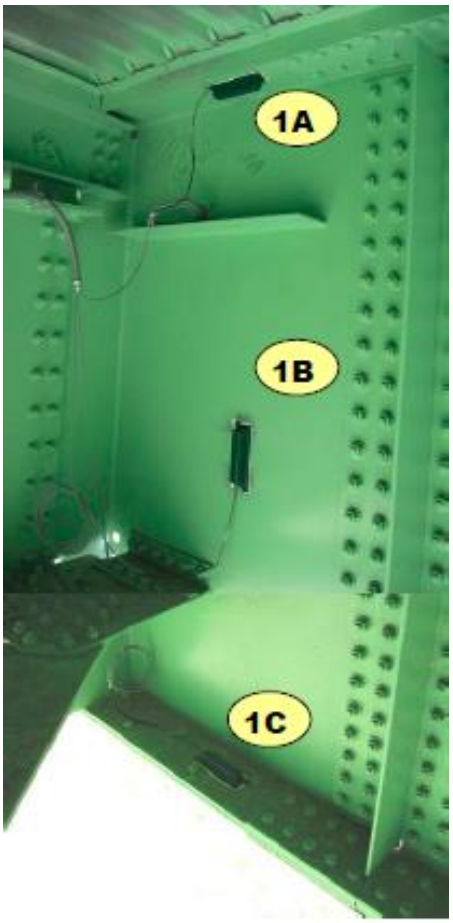

Figure 37: Example orientation of LST sensors (Hartle, 2006)

Figure 38 details the different components of the LST sensors used. The sensors operate by converting measured deflections to strains, taking the gauge length at the time of release as the initial length (Hartle, 2006).

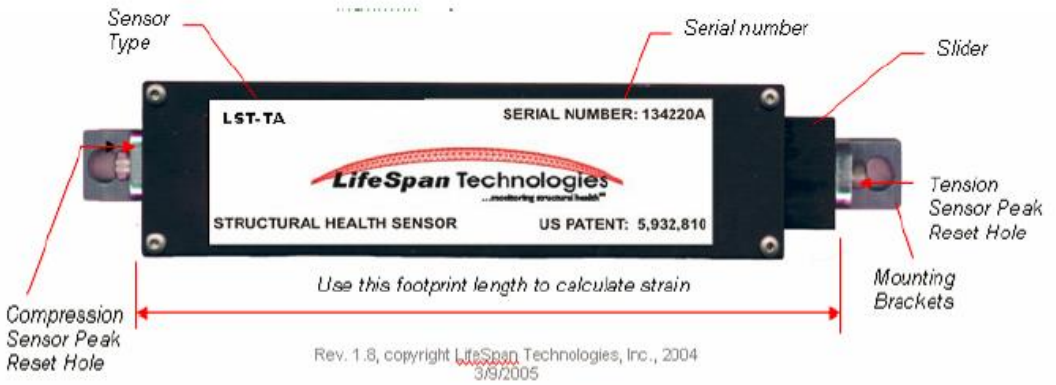

Figure 38: Components of LST sensors (Hartle, 2006)

A strong correlation between the measured strains and the ambient temperature readings was observed in most of the sensors. This correlation was quantified by calculating an r-squared value for each sensor with a value of 1.0 representing a perfect correlation. In Table 5, the r-squared values calculated for each sensor are displayed (Hartle, 2006).

Table 5: Quantification of active channel sensitivities to temperature (Hartle, 2006)

sensor	location	active sensor range με	r = active sensor correlation to T2	r^2
CCB-001	#1A	579	(0.896)	0.80
CCB-002	#1B	933	(0.621)	0.39
CCB-003	#1C	628	(0.319)	0.10
CCB-004	#2A	494	(0.909)	0.83
CCB-005	#3A	538	(0.970)	0.94
CCB-006	#3B	434	(0.973)	0.95
CCB-007	#4A	578	(0.982)	0.97
CCB-008	#4B	512	(0.981)	0.96
CCB-009	#4C	402	(0.861)	0.74
CCB-010	#5A	504	(0.921)	0.85
CCB-011	#5B	628	(0.866)	0.75
CCB-012	#5C	494	(0.063)	0.00
CCB-013	#6A	737	(0.971)	0.94
CCB-014	#6B	698	(0.962)	0.92
CCB-015	#6C	59	(0.226)	0.05
CCB-016	#7A	77	(0.372)	0.14
CCB-017	#7B	481	(0.910)	0.83
CCB-018	#7C	72	(0.893)	0.80
CCB-019	#8A	873	(0.875)	0.77
CCB-020	#8B	1285	(0.820)	0.67

Additionally, several plots of strain vs time were formed from the data collected. Although the live load strains determined are presumed to be relatively accurate, "definitive values of live load strain can only be measured if the bridge is closed to all traffic long enough to establish a baseline (or "0" value) for dead load only deflection, without the vibration interference produced by truck traffic. These values can be further refined by performing static and rolling load tests under the same closed bridge condition" (Hartle, 2006).

The plot of strain over the seven month period of one such sensor is displayed in figure 39. The first and longest flat portion of the peak channel data curve in this plot indicates a zone of "compression only" occurring in the steel during that time. This is because positive increases in strain measured are tensile strain increases or a reduction in compressive strain. Additionally, the researchers determined from the plot a significant

correlation between strain increase and temperature decrease, confirming the temperature correlation analysis results. Finally, researchers concluded abrupt positive changes in the peak channel strain curve correlating with abrupt positive changes in the active channel strain curve are likely due to the active channel capturing in-service loads (Hartle, 2006).

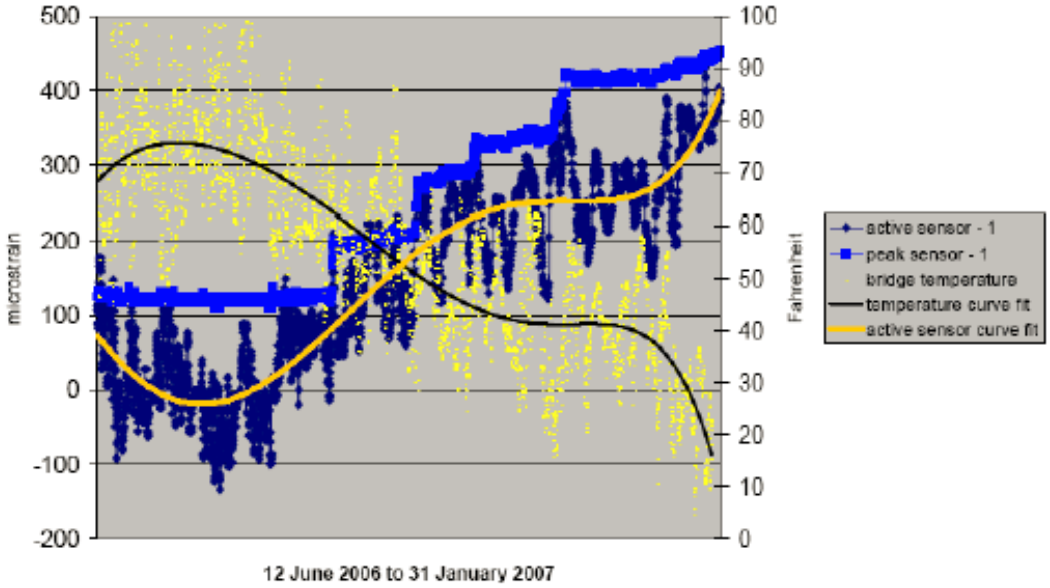

Figure 39: Strain vs Time-Plot of a subject sensor on the I-80 Bridge over Canoe Creek (Hartle, 2006)

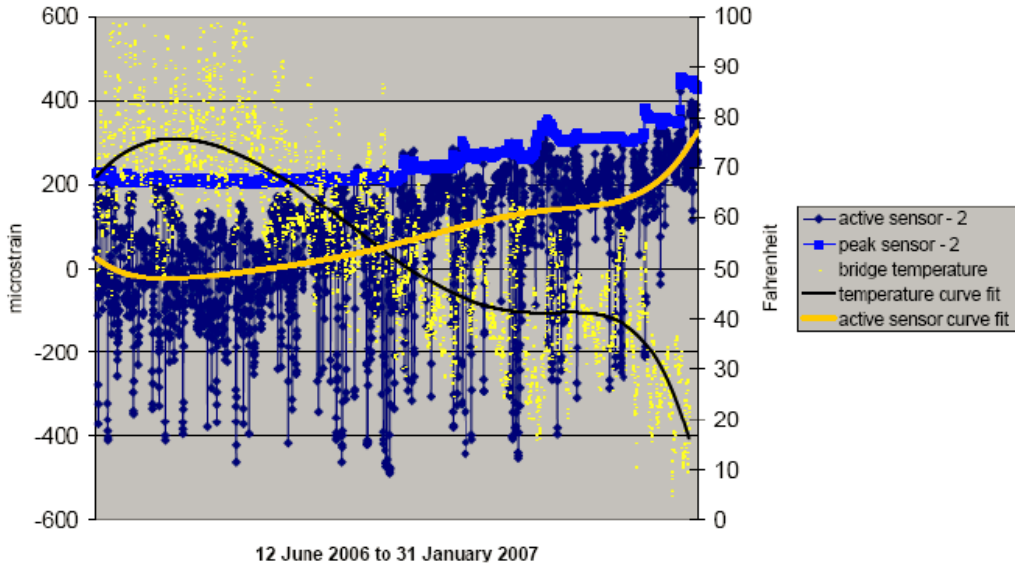

Figure 40: Sensor with large range of active strain (Hartle, 2006)

Figure 40 reveals a sensor in which there was a large range of strain in the active channel. The researchers concluded that this indicates a strong influence of in-service loads on the steel at the location of this sensor (Hartle, 2006).

The final comments regarding the strain measurements of the LST sensors for this project are related to concerning strain readings. The idiosyncratic strain readings were not prevalent (allowing the majority of the sensor measurements to be deemed acceptable) but did occur during the research. Sometimes peak channel strain readings do not commence at the same value as the active channel strain readings. This is due to timing differences in release and initial data capture (Hartle, 2006). Additionally, very large strain ranges were sometimes measured (up to 1285 microstrain) in this study. This was of "significant concern" to the researchers (Hartle, 2006). Only two of the twenty strain plots recorded ranges of significant concern.

2.5 Review of July Evaluation of Hanging Rock Creek Bridge

In July of 2017, when the Hanging Rock Creek Bridge (HRB) was approximately one month old, load tests were conducted by Clemson researchers to evaluate the transverse condition and load distribution factors of the solid slab and NEXT-D girders. Loaded dump trucks were slowly driven across both the solid slab and NEXT-D spans while strain transducers and linear variable differential transformers (LVDTs) recorded bending strains and relative horizontal deflections respectively (Filosa, 2017). A schematic of the strain transducer and LVDT locations for the solid slab and NEXT-D spans are shown in figures 41 and 42 respectively.

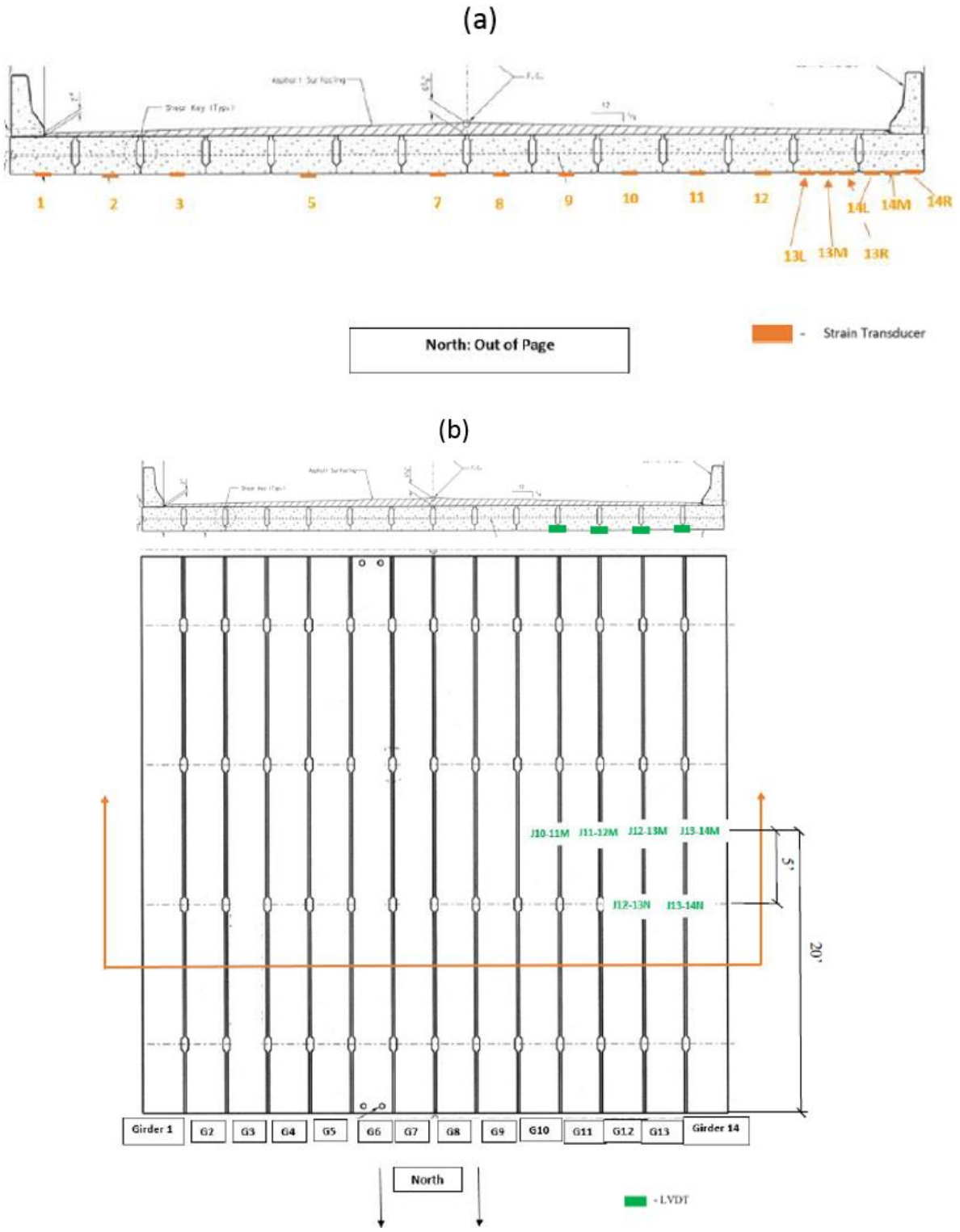

Figure 41: (a) strain transducer locations and (b) LVDT locations on the solid slab span of the HRB (Filosa, 2017)

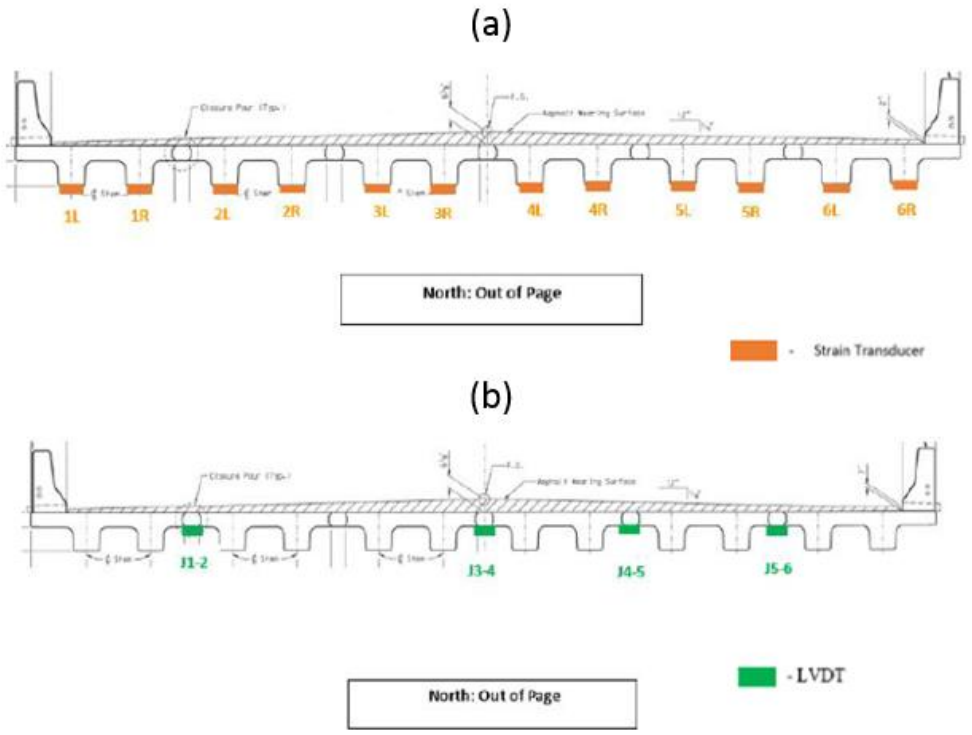

Figure 42: (a) strain transducer locations and (b) LVDT locations on the NEXT-D span of the HRB (Filosa, 2017)

Several transverse truck locations were selected for testing the two spans. The truck locations were selected considering the evaluation of both interior and exterior distribution factors for moment (DFM) for both single lane loading and multiple lane loadings (2 trucks). The DFMs were calculated considering the bending strain measured during live load testing. Additionally, LVDTs were placed at critical transverse joints close to the truck locations to evaluate the condition of the joints at 1-month old.

The DFMs calculated for the solid slab beams are presented and compared to DFMs determined using AASHTO section type “g” in table 6. It was concluded that in some cases the solid slab span may not be distributing load as designed since the experimental DFMs were sometimes larger than the design DFMs.

Table 6: 1-month old experimental DFMs calculated and comparisons to AASHTO DFMs (Filosa, 2017)

	Single Truck		Side-by-Side Truck	
DFM Method	Exterior Girder	Interior Girder	Exterior Girder	Interior Girder
AASHTO - type g	0.27	0.21	0.25	0.24
Experimental DFM	0.16	0.20	0.20	0.27

The relative horizontal deflections measured by the LVDTs on the solid slab span are presented in table 7. The data indicated that some of the displacements were relatively large, especially in comparison to the NEXT-D LVDT data presented in table 9 (Filosa, 2017).

Table 7: 1-month old relative horizontal deflections of the solid slab girders during live load testing (Filosa, 2017)

		Load Scenario									
		#1	#2	#3	#4	#5	#6	#7	#8	#9	#10
LVDT	J10-11M	-0.00063	0.0023	0.0051	0.00054	0.0017	0.0045	-0.00011	-0.00014	-0.00036	-0.00055
	J11-12M	0.0060	0.0046	0.0027	0.0056	0.0039	0.0018	-0.00015	-0.00016	-0.00042	-0.00055
	J12-13M	0	0.00083	0.0017	0	0.00092	0.0018	0	-0.00001	-0.00005	-5.5E-05
	J12-13N	0	0.00082	0.0015	0	0.00092	0.0017	0	0	-2.3E-05	-3.5E-05
	J13-14M	0.012	0.0086	0.0053	0.012	0.0097	0.0064	-2.3E-05	-0.00003	-0.00048	-0.00055
	J13-14N	0.012	0.0085	0.0053	0.011	0.0095	0.0064	0	0	-0.00038	-0.00039

In table 8, the DFMs calculated for the NEXT-D beams are presented and compared to DFMs determined using AASHTO section types “i” and “k” and DFMs determined using finite element model (FEM) analyses of NEXT-6 and NEXT-8 girders (Filosa, 2017). The NEXT-6 and NEXT-8 FEMs were created by Clemson researchers preceding Filosa’s research (Sheng et al., 2013). After testing the bridge at 1-month old, it was concluded that the AASHTO type “k” section is the best option to consider when calculating DFMs for NEXT-D girders.

Table 8: 1-month old experimental DFMs calculated and comparisons to AASHTO and FEM DFMs (Filosa, 2017)

	Single Truck		Side-by-Side Truck	
DFM Method	Exterior Girder	Interior Girder	Exterior Girder	Interior Girder
AASHTO type k	0.62	0.55	0.62	0.67
AASHTO type i	0.62	0.43	0.62	0.56
NEXT-6 FE Model	0.25	0.29	0.27	0.44
NEXT-8 FE Model	0.37	0.41	0.37	0.59
Experimental DFM	0.42	0.34	0.40	0.56

The relative horizontal deflections measured by the LVDTs on the NEXT-D span are presented in table 9. From the horizontal displacement data, it was concluded that the transverse joints of the NEXT-D span were likely not cracked at 1-month old (Filosa, 2017).

Table 9: 1-month old relative horizontal deflections of the NEXT-D girders during live load testing (Filosa, 2017)

		Load Configuration							
		#1	#2	#3	#4	#5	#6	#7	#8
LVDT	J4-5	0.00017	0.00090	0.00088	0.00092	0.00069	-0.000063	-0.00012	0.00078
	J3-4	-0.0001	3.31E-05	0.00068	0.00063	0.00082	-0.00010	-0.00006	0.00076
	J1-2	-0.000024	1.16E-05	-0.00015	-0.00019	-0.00013	0.00079	0.001	-0.00017

The DFMs of the HRB NEXT-D span and relative horizontal shear key deflections of both HRB spans tested by Filosa are compared for when the HRB is 1-month and 7-months old. NEXT-D DFMs and horizontal deflections are also compared for when the HRB is 11-months old. Testing of the HRB at 7 and 11 months of age is conducted by the author. These comparisons provide insight to the author of the NEXT-D and solid slab shear keys' durability and ability to distribute live loads to other girders over time. Additionally, the NEXT-D and solid slab shear key conditions may be directly compared considering the live load tests conducted by Filosa and the author.

2.6 Non-Destructive Evaluation through Live Load Testing

Live load testing is a non-destructive technique executed for the assessment of bridges. Non-destructive testing is defined by Fu (Introduction) as "the use of noninvasive techniques to determine the integrity of a material, component or a structure or quantitatively measure some characteristic of an object". Often bridges lack original structural drawings, carry permit truck loads (loads greater than what is typically allowed), implement new girder geometries, or contain new materials (ultra-high performance concrete, fiber reinforced polymers, etc.) which, among other reasons, provide the need for live load testing. Monitoring of subject bridges via live load tests leads to a better understanding of overall bridge behavior and offers a "useful reference for designers, contractors, and researchers" (Yang, 2003). After live load tests are conducted, future bridges may be designed with an increase in safety or savings, depending on the level of conservatism of the analyzed bridge's current design. Although live load tests can be more costly than tests conducted in laboratories, they provide the most comprehensive knowledge of bridge behavior to researchers which aids in the refinement of finite element models, updating of design codes, and determination of weaknesses of bridge components.

A live-load test provides "a real evaluation of bridge behavior since it includes all the parameters that affect the behavior" (Fu, 1996) When conducting live load tests, researchers apply known loads at known locations on a subject bridge to determine a known structural response. Static and dynamic tests may be conducted. Some static tests involve parking trucks at critical locations while others involve "crawl tests" where

trucks slowly drive across a bridge's critical locations (Smolenski, 2004). Dynamic tests involve trucks moving at typical travel speeds. While the trucks are in position, instrumentation collects characteristic information of a subject bridge.

Many different instruments are available to researchers for studying bridge behavior. Strain gauges and strain transducers are among the most common instruments utilized and are used for measuring the strain in bridge girders or bridge decks. Linear variable displacement transformers and string pots may be used to measure bridge deflections. Rotations of bridge components may be measured using tiltmeters. Data acquisition systems collect and store data from the instrumentation during testing to later be evaluated by researchers. Adjustments of the instrumentation by researchers may be performed during testing using the data acquisition system, such as the sampling rate of gauges.

Live load testing of a bridge is critical and provides data to understand a bridge's response to vehicular loading initially and, depending on how many tests are conducted, as a function of time (Neely, 2004). A well planned live load test will place loads at the bridge's critical locations, resulting in conclusions and recommendations that provide streamlined solutions to sub-par bridge behavior. Although laboratory tests are beneficial, "when determining a safe and accurate load-carrying capacity for a bridge, the best model of the structure to use is the bridge itself" (Chajes, 2000).

2.7 Literature Review Summary

This chapter reviews several topics of interest for this thesis. Firstly, the origin of the Northeast Extreme Tee (NEXT) beam is discussed to understand the motives for its

invention and how it may be an advantageous replacement to traditional box beams. The following subchapter in the literature review discussed both theoretical and experimental distribution factors. The review of distribution factors aided the author in understanding how they have changed over time and effective methods for determining them experimentally.

The transverse behavior and durability of girder-to-girder connections was reviewed to outline the current issues at these transverse connection points. The data provided by the live load tests and laboratory tests reviewed considering the behavior and durability of girder-to-girder connections may be compared to the experimental data of the HRB. Also, the durability tests reviewed provided a valuable insight to the author that a considerable increase in strain or displacement over time is indicative of cracking. Methods of long-term monitoring in practice were also surveyed for the author's understanding of their effectiveness and their shortcomings. Finite element models and laboratory tests allow researchers to quickly evaluate the long-term behavior of transverse bridge components, but only symbolize the behavior that occurs in the field. Precise in-service behavior may only be determined via long-term monitoring in the field. LST is one tool that is used to conduct long-term monitoring in the field. This tool was reviewed by the author and it was determined that a temperature correlation analysis and live load tests are useful for calibrating LST sensor data. Also, data indications of live load crossings while a bridge is in-service were reviewed. Finally, some of the common glitches that may occur while LST sensors collect data were discussed for the awareness of the author.

A brief review of the research conducted in July of 2017 on the HRB provided the author some insight of the advantages and disadvantages of UHPC shear keys, solid slab girders, and NEXT-D girders on the HRB spans. Data is also provided in the thesis authored by Filosa (2017) that may be compared to data from further load tests conducted by the author for the purpose of evaluating the durability of the shear keys' on the spans of the HRB. Finally, a review of non-destructive live load testing is presented since the majority of the author's research is conducted via live load tests. With the information provided in this literature review and in the remainder of this thesis, the author aims to present conclusions and recommendations regarding the implementation of the NEXT-D beam for short to medium span bridges and regarding the implementation of UHPC for the fill of flat slab girder shear keys at their transverse connections.

Chapter 3: Research Methodology

The Hanging Rock Creek Bridge (HRB) has been the subject of research for the evaluation of the NEXT-D and solid slab girders and the UHPC shear key fills it employs. The long-term behavior of the shear keys of the NEXT-D, solid slab, and voided slab spans were continuously monitored using instrumentation supplied and installed by Life-Span Technologies (LST). Live load (LL) tests were performed in July of 2017, and January, May, and October of 2018 on the spans of the HRB to compare the LL test data to the LST software data, and to evaluate the shear keys and LL distribution factors (moment and shear) of the NEXT-D and solid spans. The LL test in July of 2017 was performed by Filosa (2017), while the remaining LL tests were performed by the author and are reported herein. Additionally, visual inspections were conducted to evaluate the condition of the HRB spans.

3.1 Methodology Purpose

Three methods of evaluation were utilized to assess the Hanging Rock Creek Bridge (HRB) behavior. The methods are visual inspection, use of Life-Span Technologies (LST) long-term monitoring system, and live load (LL) testing. The purpose of each method is given in the following subchapters.

3.1.1 Visual Inspection Purpose

Visual inspections of the HRB were conducted to assess and document the bridge condition. Visual inspections were conducted at approximately six month intervals beginning with an inspection at the time of the bridge's opening and concluding about 18 months later. During the final assessment, a photo survey of the bridge was organized to

provide visual documentation of the bridge health. Another purpose of visual inspection was to identify components of the bridge that needed to be closely evaluated with instrumentation in addition to the bridge components already selected to be instrumented.

3.1.2 LST Purpose

LST sensors were utilized to monitor the transverse strain and temperature of the Hanging Rock Creek Bridge (HRB). LST provides a website on which selected users (username and password are required) can access the daily online strain and temperature data of the in-service wireless sensors at any time, thereby providing a long-term monitoring system. Since strain and temperature data is collected simultaneously on the NEXT-D span, the heating and cooling effects on the transverse strain in and around the longitudinal girder joints may be evaluated.

The drawback of the LST system is the data provided is somewhat difficult to interpret. Many factors may contribute to changes in strain in the joints over time including temperature, creep, shrinkage, and live load. It is difficult to pinpoint how the loads directly influence the strain data and to determine what the quantified strain data means in terms of the bridge health. Thus, LL tests aided in determining a known structural response of the bridge due to LL, thereby providing a calibration of the LST strains to a known load.

3.1.3 Live Load Tests Purposes

Four LL tests were performed on the HRB. The first was performed in July of 2017 by Filosa (2017). The purpose of this test was to evaluate the moment distribution factors (DFM) and the relative horizontal displacements of the girders on the NEXT-D

and solid spans just after the bridge opened. This provided an initial assessment of how well these two spans distributed LL transversely. The results Filosa outlines in his thesis (2017) are compared to the appropriate results of this thesis.

The other three LL tests were performed in January, May, and October of 2018. The January test was performed when the bridge was 7 months old to specifically evaluate the response of the LST sensors due to LL on the NEXT-D, solid, and voided spans. This was a calibration of the LST system to a known load. The test in May was performed when the bridge was 11 months old. This test evaluated the DFMs and relative horizontal displacements of the NEXT-D girders. Also during the May test, some of the instrumentation was placed on the NEXT-D span to directly compare to the transverse data obtained from the LST sensors. This allowed the researchers to determine the response of the bridge due to LL using two different systems and ensure the data was reasonable since the LST sensors may be influenced by other factors in addition to LL.

In the LL test conducted in July of 2017, relative horizontal displacements measured on the solid span were much larger than those measured on the NEXT-D span (0.012 inches compared to 0.001 inches). For this reason, the joints on the solid span are believed to be more prone to crack at the precast to UHPC bond (Filosa, 2017). Additionally, one of the joints on the solid span recorded much larger displacements than the other joints on the same span under similar loading. As a result, during the May LL test the researchers measured the relative horizontal displacements of the girders on the solid span to evaluate the health of the transverse joints.

The final purpose of the May LL test was to address the objective of determining distribution factors for shear (DFV) on the NEXT-D span. Instrumenting a bridge to collect shear strain can be difficult due to the influence of moment, torsion, and bridge barriers on the strain data collected. For this reason, a study was performed to determine if it was reasonable to calculate DFVs on the NEXT-D span of the HRB with the equipment available to the researchers. The May LL test evaluated the effectiveness of using one strain transducer per web for determining DFVs.

The purpose of the October live load test was to determine if DFMs and relative horizontal displacements change over time on the NEXT-D span by comparing to the appropriate data from the other LL tests. Additionally, a torsion test was performed to evaluate the effect of torsion on shear strain measured when determining DFVs. Table 10 summarizes the LL tests conducted with their purposes and the instrumentation utilized for each test. The instrumentation and evaluation procedures of all of the 2018 LL tests are discussed in more detail in the further subchapters.

Table 10: Live Load Test Summary

Live Load Test Number	Live Load Test Date	Instrumentation	Purpose
1	July 2017	Strain Transducers (ST), Linear Variable Displacements Transformers (LVDT)	Measure relative horizontal displacements and DFMs of the girders on the NEXT-D and solid slab spans
2	January 2018	LST Sensors	Evaluate the LST sensors under a known live load
3	May 2018	ST, LVDT, LST sensors	Measure relative horizontal displacements on the NEXT-D and solid spans, measure DFMs on the NEXT-D span, directly compare LST sensor data to LVDT data, evaluate effectiveness of using one ST per web to measure DFV
4	October 2018	ST, LVDT, LST sensors	Measure relative horizontal displacements and DFMs of the NEXT-D girders, evaluate torsion influence on experimentally measured shear strain

3.2 Instrumentation and Instrumentation Plans

A discussion of the Life-Span Technologies (LST) sensors and website, and the instrumentation and data acquisition (DAQ) system used during the live load (LL) tests is provided in this subchapter.

3.2.1 LST Website and Sensor General Function

LST provides strain and temperature data that may be downloaded by select researchers on their password protected website. The collection and calibration of the data is performed by LST alone, and therefore the availability and quality of the data is controlled by LST. In order to navigate the LST website, a user will first log in to gain access to their project's data and select their project. Next, the user may select either a

single sensor's data plots to view, or can select all of the sensors' data plots to view. After sensors are selected, the user has the option of viewing the active channel data plot(s), the peak channel data plot(s), or both the active and peak channel data plot(s). A flow chart of how the site is navigated is presented in figure 43.

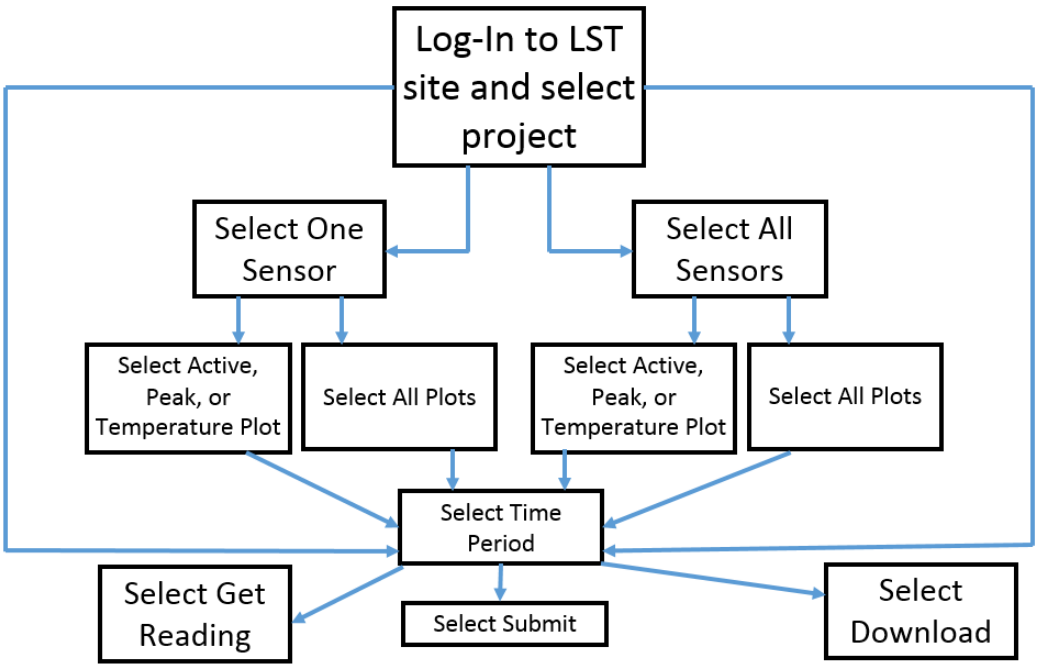

Figure 43: Flow-chart of how to navigate the LST website

Figure 44 displays what a user would view when initially logged into the site.

Figure 44: Initial screen after log-in

"The on-structure LifeSpan controller sends a complete set of measured data to the LifeSpan Network Operations Center (NOC) at 03:00, 05:00, 07:00, 08:00, 12:00, 16:00, 17:00, and 18:00, with system restarts at 06:30 and 18:30 daily" (Hartle, 2006).

The active channel of a sensor presents real-time strain readings of the bridge at the aforementioned times. The peak channel of a sensor presents, at the aforementioned times, the largest tensile strain reading since installation. The lines connecting the data points in the active plots are assumed trends of the real-time strain in the component measured. The peak channel measures continuously, so if a new maximum tensile strain is measured, the new maximum data point is recorded whenever the next "round" of data is sent to the NOC (i.e. whenever the next aforementioned time of data retrieval occurs). Otherwise, if there is no recording of tensile strain greater than the previous maximum, the same strain data point previously retrieved is sent to the NOC at the next time of data retrieval. This means that the specific time of abrupt strain change is not captured, but within up to 9 hours of this abrupt change, the data will be recorded (generally it would be within 1-4 hours, only in the middle of the night would this time increase beyond 4 hours). Figure 45 shows an example of active and peak strain data readings from the LST website for the NEXT-D girder.

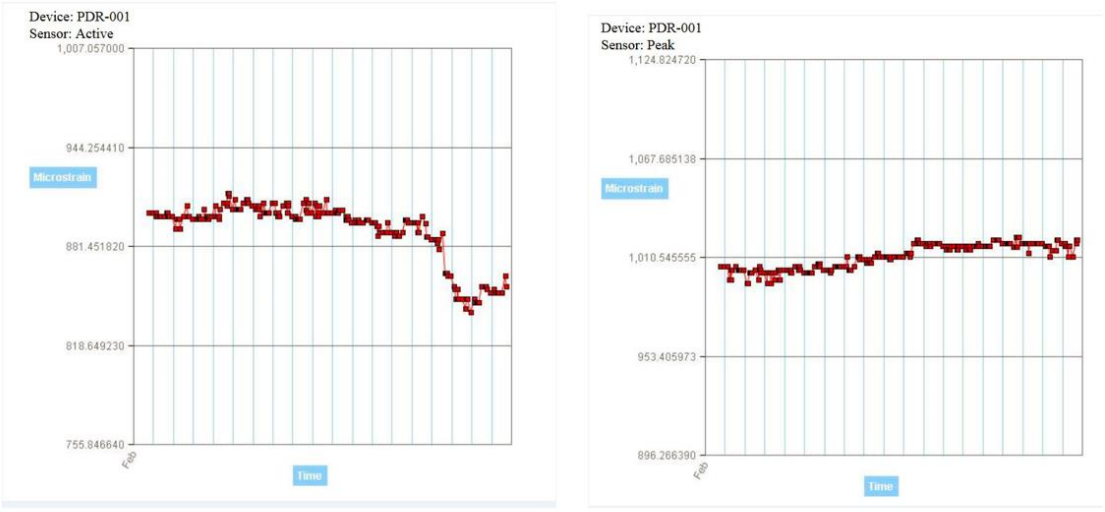

(a) (b)

Figure 45: (a) is an active strain plot and (b) is a peak strain plot from the LST site

As discussed before, the LST sensors located on the NEXT-D span collect temperature data in addition to strain data. Figure 46 displays an example of a LST temperature plot on one of the NEXT-D girders. The selection of the temperature function is noted in figure 43.

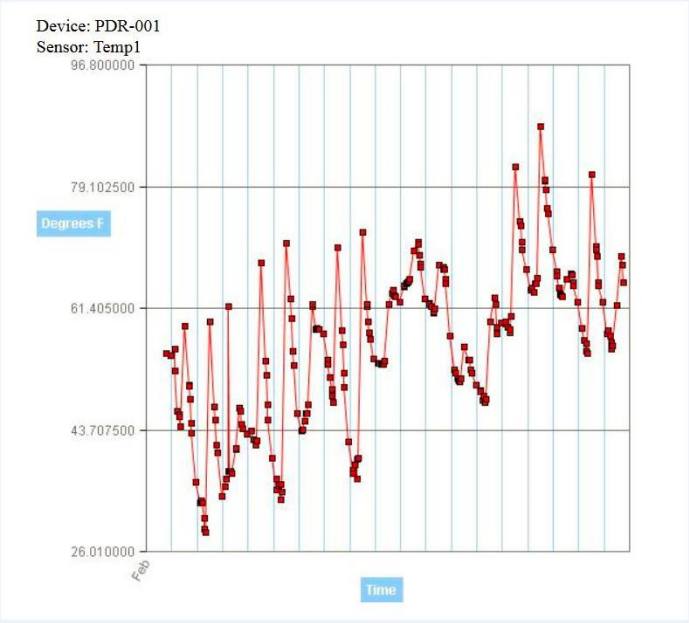

Figure 46: Temperature plot from the LST site

Lastly, LST provides a "Get Reading" function. If this function is selected, the sensors will add a data point for both the active and peak channel in addition to their eight daily measured data points. Figure 47 displays the "Get Reading" function on the LST site. Also in this figure it is evident that LST allows the user to download any supply of data the sensors have measured. This data is used to create all of the LST plots. The "Get Reading" and "Download" functions are also noted in figure 43.

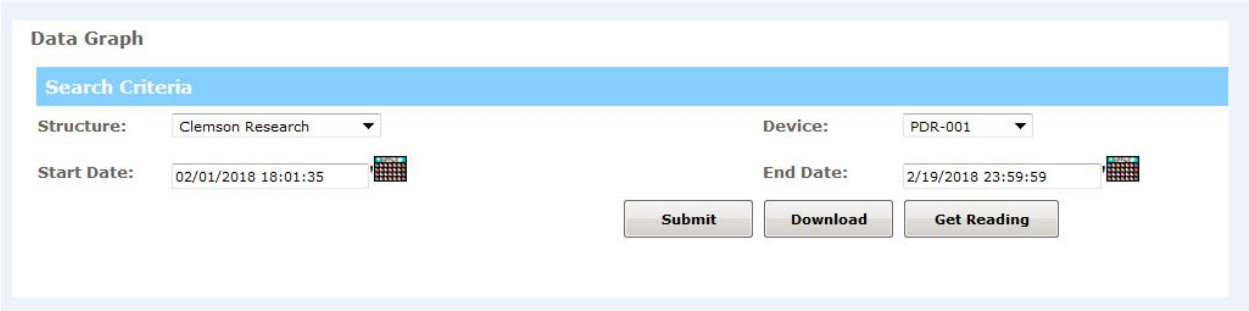

Figure 47: "Get Reading" and "Download" function on the LST site

3.2.2 LST Sensor Locations and Orientation

The HRB has a total of twelve LST sensors: four on the NEXT-D span, four on the solid span, and four on the northern voided span. The sensors are mounted at several of the critical transverse joints of the bridge and measure the strain across the respective transverse joints. The sensors on the NEXT-D span are at mid-span while the sensors on the solid and voided spans are at both mid-span and at the locations of transverse post-tensioning. All of the sensors were installed in May of 2017. Figures 48-50 show the locations and nomenclatures of the sensors on the different bridge spans.

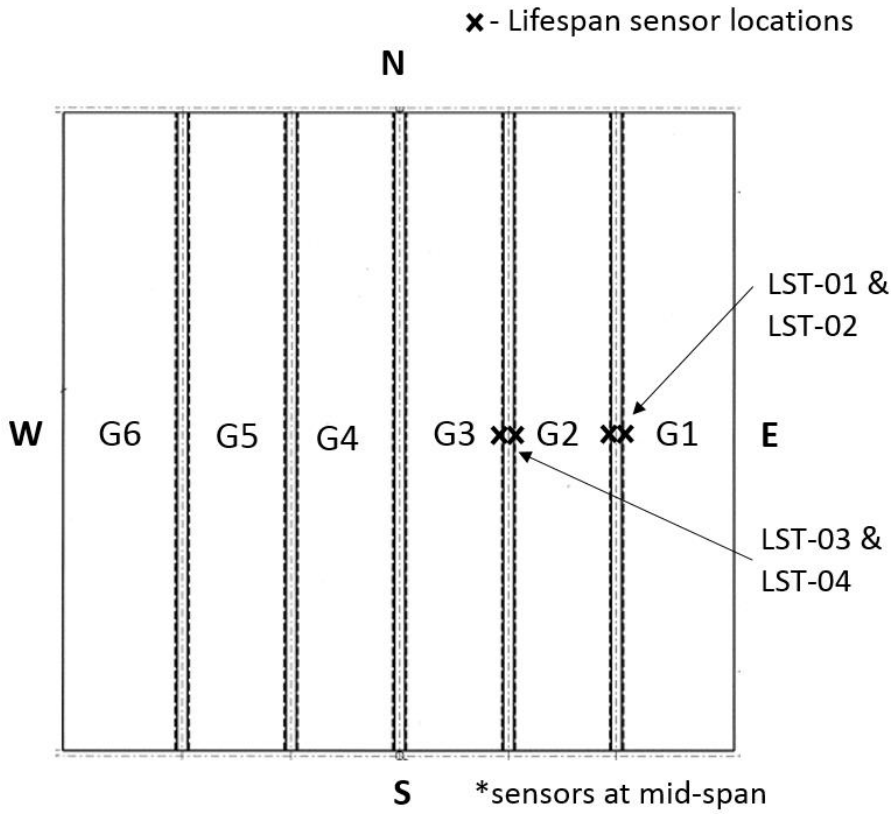

Figure 48: Sensor locations on the NEXT-D span

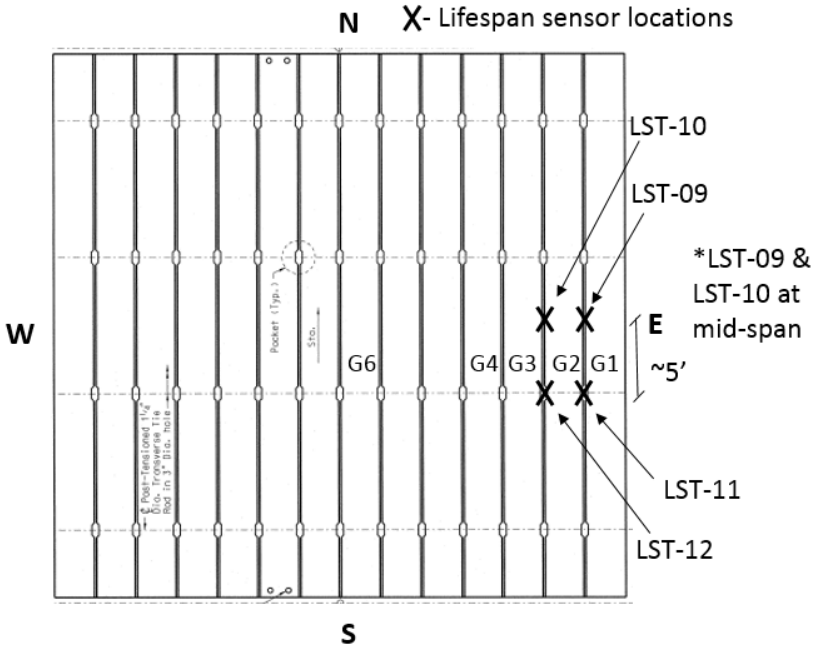

Figure 49: Sensor locations on the solid span

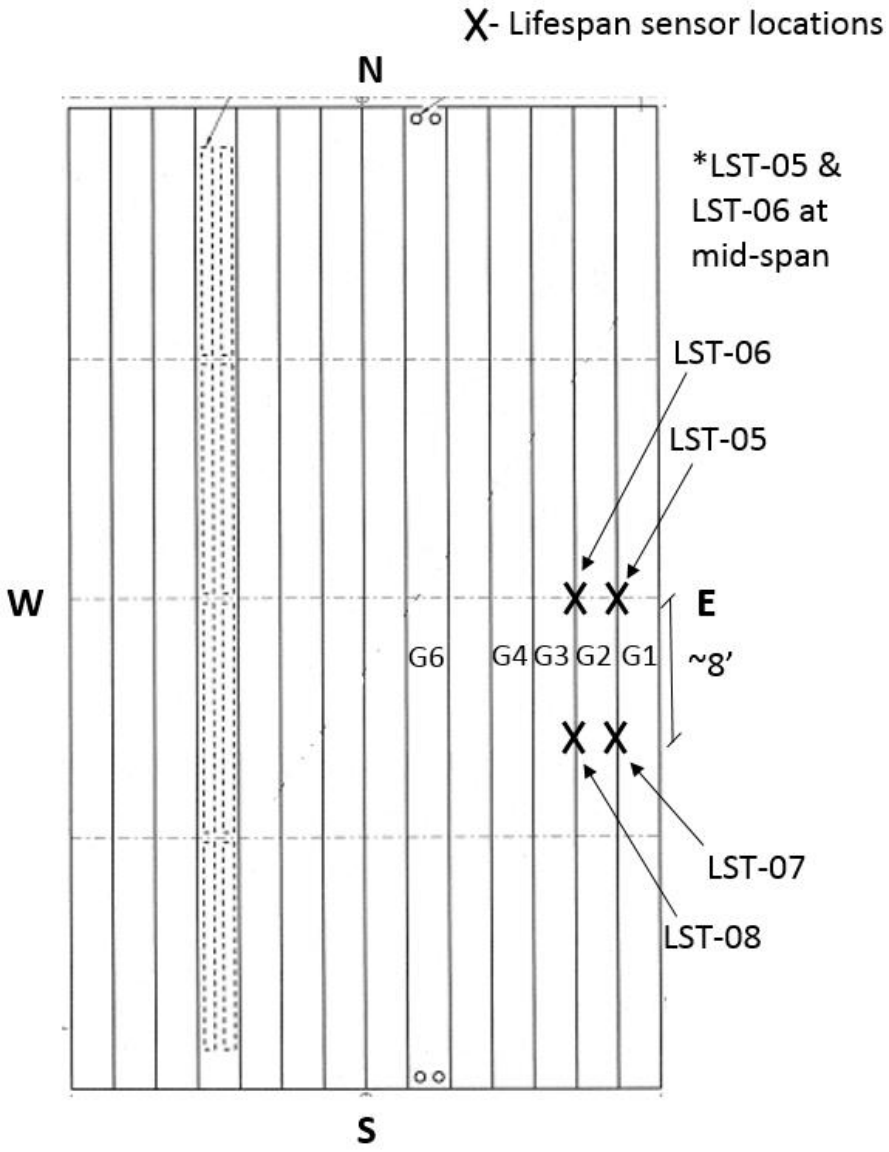

Figure 50: Sensor locations on the voided span

The sensors are each denoted with the letters "LST" followed by the number corresponding to each individual sensor. This allows the users of the LST website to navigate each individual sensor's recorded data and plots. Figure 51 displays the orientation of the sensors at the transverse joints.

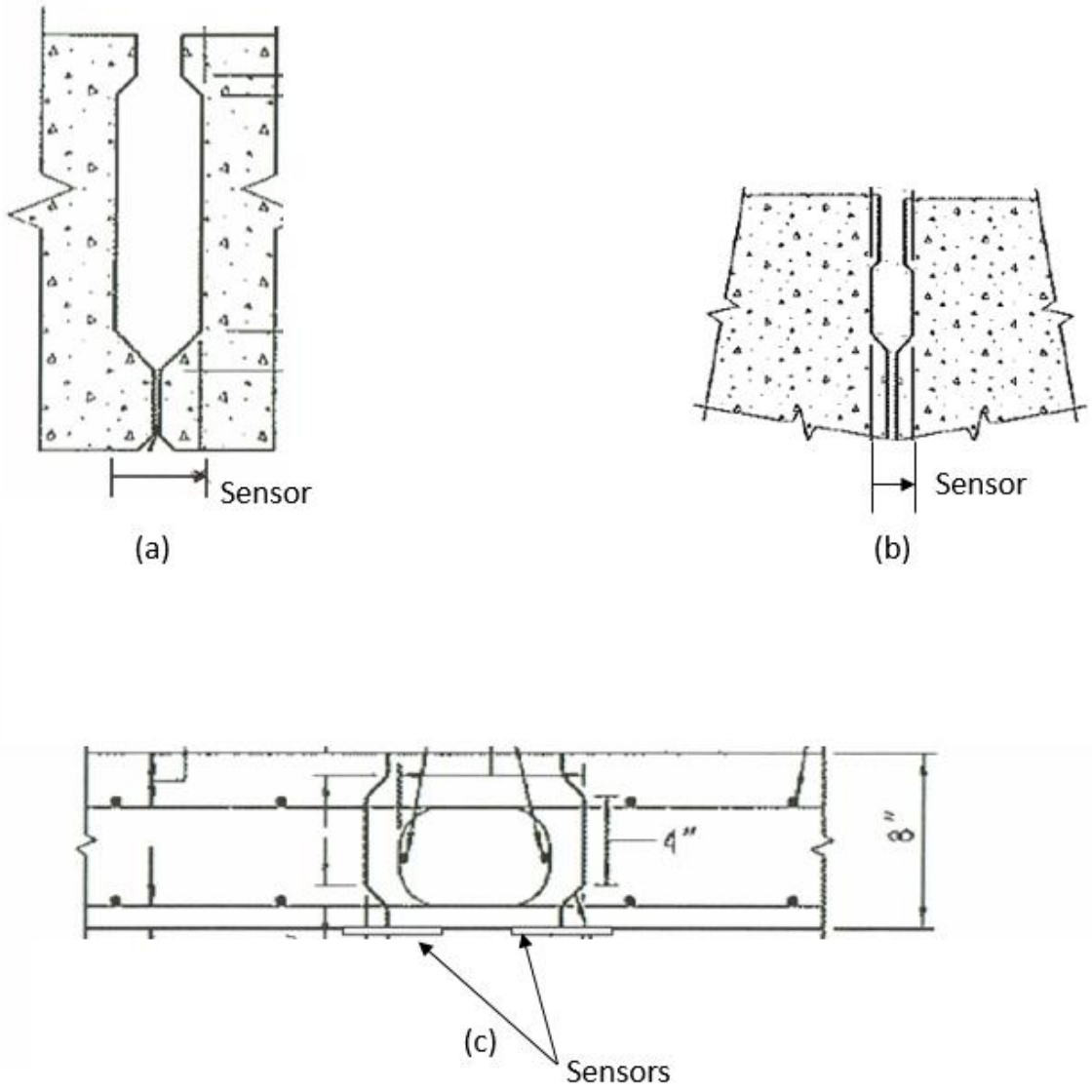

Figure 51: LST sensor orientations for (a) the solid span, (b) the voided span, and (c) the NEXT-D span

3.2.3 Strain Transducers and Linear Variable Displacement Transformers

The instrumentation used during the LL tests consisted of strain transducers and linear variable displacement transformers (LVDT) purchased from and calibrated by Bridge Diagnostics Incorporated (BDI). LVDTs were utilized to measure the relative horizontal displacements of the girders. The LVDTs were screwed into a casing and

attached by sticking the casing, with Loctite glue, to a girder surface. Before the casing was attached, accelerant was sprayed onto the glue that was applied to the LVDT casing so that researchers would not have to press the LVDT against the girder for a long period of time before it was secure. The LVDTs were attached near girder transverse joints so that the LVDT arm stretched over the transverse joint and made contact with a wood block that was glued to the adjoining girder. In this way, the LVDTs measured the horizontal displacement of a girder relative to its adjoining girder. The LVDTs were attached longitudinally at mid-span on both the NEXT-D and solid spans, which on the NEXT-D span placed the LVDTs directly next to LST sensors. The LVDT measurements were of importance because they provided insight to the condition of the UHPC shear key joints and provided data that allowed for a direct comparison to the LST data. A close-up of an attached LVDT next to a LST sensor is shown in figure 52. The transverse locations and orientation of the LVDTs used during the LL tests is discussed in further sub-chapters.

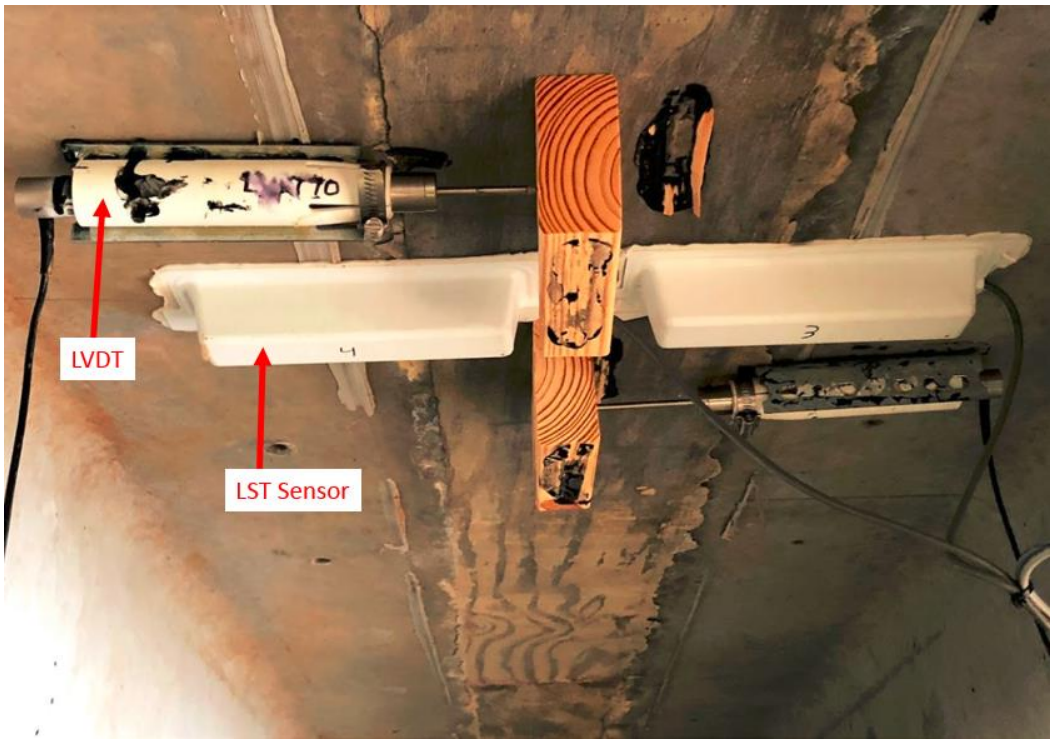

Figure 52: LVDT and LST Sensor attached at transverse joint of NEXT-D girders

Strain transducers were attached to the bottom surfaces of girders to measure the girder bending strain. They were attached by screwing on metal feet to the bottom of themselves and applying Loctite glue on to the "feet" to which they were attached. Next, accelerant was sprayed on the glue and the strain transducer was attached to the bottom of the beam by a researcher. The accelerant allowed the instrument to quickly adhere to the surface of the girder. Strain transducers were always attached at girder mid-spans since this is where the bending strain under the load would be close to maximum. The bending strain data collected allowed the researchers to calculate girder DFMs. Figure 53 displays a close-up photograph of an attached strain transducer located to measure bending strain. Strain transducers were also utilized to measure shear strain, and for this purpose were located closer to the supports and placed near the web-flange intersection in

a rosette orientation. The location and orientations of the strain transducers used during the LL tests is discussed in depth in further sub-chapters.

Figure 53: Strain transducer attached to a NEXT-D girder

3.2.4 LVDT Instrumentation Location and Orientation

During the LL tests in July of 2017, and May and October of 2018 (LL tests 1, 3, and 4 respectively), Linear Variable Displacement Transformers (LVDT) were attached at selected transverse joints on the HRB. The locations of the LVDTs used during LL tests 3 and 4 on the NEXT-D span are presented in figure 54. The location of the LVDTs during LL test 1 is referenced in subchapter 2.5 of the literature review. The typical orientation of the LVDTs on the NEXT-D span is displayed in figure 52. As discussed before, LVDTs were always located longitudinally at mid-span.

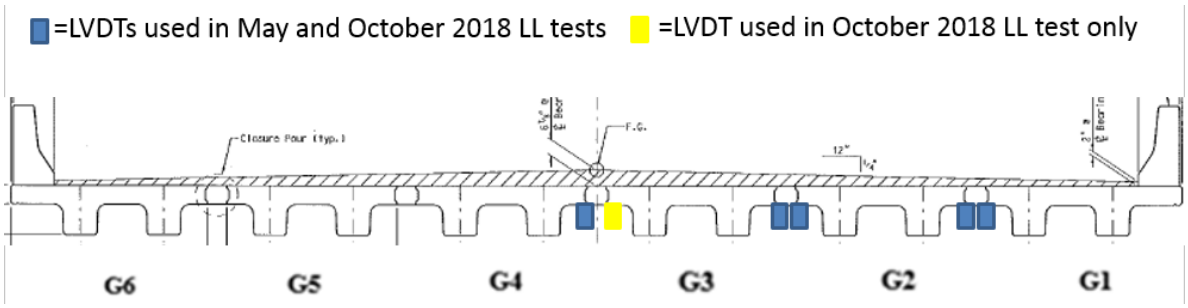

Figure 54: LVDT locations on the NEXT-D span for the LL tests 3 and 4

Transverse joints on the solid span were also evaluated by measuring the relative horizontal displacements of the girders. The location and typical orientation of the LVDTs instrumented on the solid span are presented in figures 55 and 56.

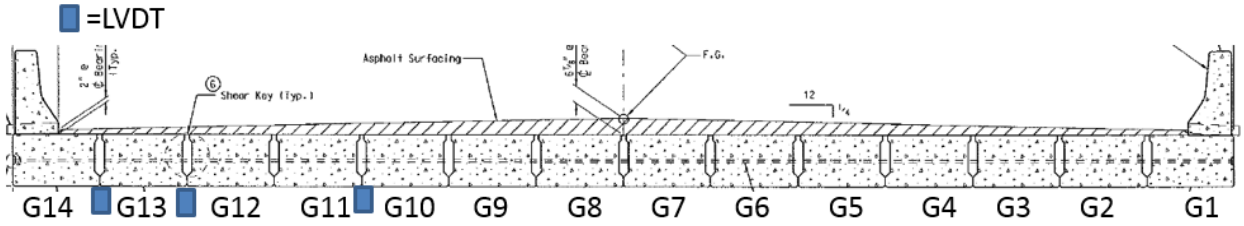

Figure 55: LVDT locations on the solid span for LL test 3

Figure 56: LVDT installed on the solid span (Filosa, 2017)

3.2.5 Strain Transducer Instrumentation Locations and Orientation

Strain transducers were attached at mid-span of the NEXT-D girders during LL tests 1, 3, and 4. The location and typical orientations of the strain transducers on the NEXT-D span during the LL tests 3 and 5 is presented in figures 57 and 58 respectively. The location of the strain transducers during LL test 1 is referenced in subchapter 2.5 of the literature review.

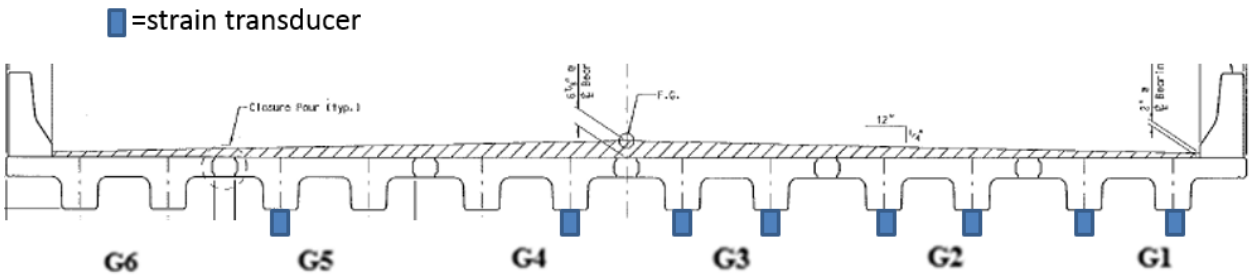

Figure 57: Strain transducer locations for the NEXT-D DFM LL tests

Figure 58: BDI strain transducers attached to the NEXT-D span

A previous LL test by Filosa indicated that approximately 5% of the load was distributed to the girder furthest away from the applied LL in all load configurations, which is considered negligible. Since the load configurations (which are presented later in this subchapter) for LL tests 3 and 4 are very similar to those utilized in LL test 1 by Filosa, it was deemed acceptable to not instrument girder 6. By considering the load on the girder furthest from the applied load as negligible, conservative DFMs were calculated. Additionally, it was evident from LL test 1 that the unloaded girders displayed a linear trend as to how the load distributed to them. For this reason, a web in girder 5 and a web in girder 4 was not instrumented, and instead the bending strain experienced by these webs was linearly interpolated. By using minimal strain transducers during the DFM LL test, moment and shear distribution LL tests could be conducted simultaneously.

During LL test 3, three webs of the NEXT-D span were selected to be instrumented with strain transducer rosettes to determine the effectiveness of using one strain transducer per web for determining DFVs. The rosettes would allow the researchers to determine the extent to which moment and compression influenced the strain readings of the diagonal strain transducers in the rosettes and determine if data from diagonal strain transducers alone is reasonable for calculating DFVs. The locations of the rosettes on the NEXT-D span are shown in figure 59. Two of the rosettes utilized three strain transducers and one of the rosettes utilized two strain transducers. The strain transducer rosette with just two transducers was utilized due to limited instrumentation. The orientation of the strain transducer rosettes are shown in figure 60. In all locations

the vertical strain transducer was placed two feet from the face of the bridge end bent (support). If there was no vertical transducer, the intersection of diagonal and horizontal strain transducers was approximately 2 feet from the face of the bridge end bent. The rosette was positioned as close to the flange as possible based on the calculated estimate of the neutral axis location (appendix).

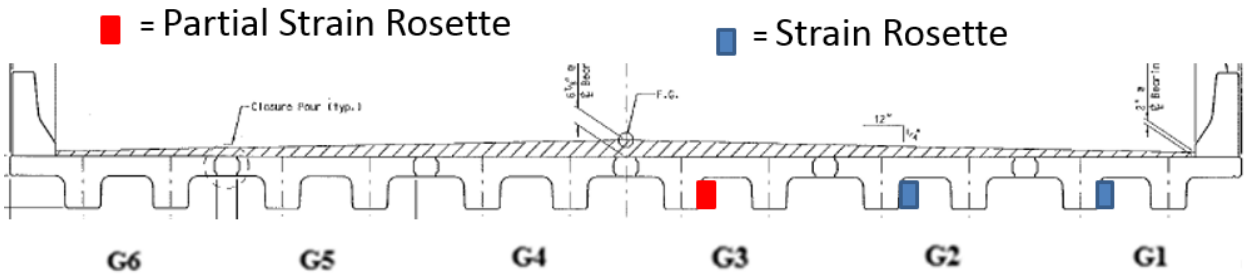

Figure 59: Strain transducer rosette transverse locations

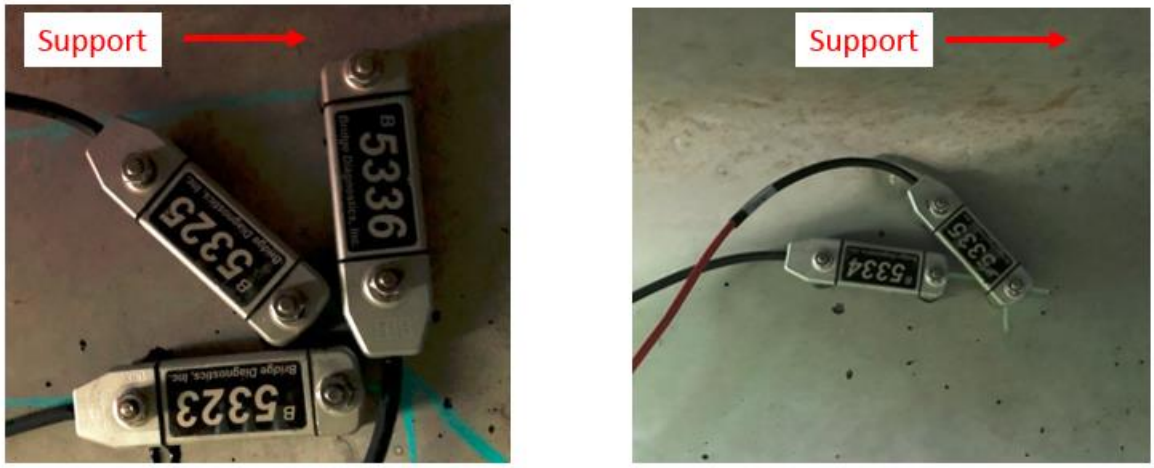

Figure 60: (a) three strain transducer rosette orientations and (b) two strain transducer rosette orientation

After review of the data from LL test 3, it was surmised that torsional shear strain may be influencing the total shear strain measured in the strain transducer rosettes during LL test 3. The researchers determined that the available equipment was not adequate to

effectively determine DFVs with the potential of strong torsional shear strains, and thus decided to conduct a torsion LL test to determine the level of torsion induced on the NEXT-D girders due to LL. Strain transducer rosettes were instrumented on either side of a subject girder web during LL test 4 to determine the torsion in the subject girder. The location of the strain transducer rosettes is shown in figure 61. The orientation of the eastern strain transducer rosette is shown in figure 62a and the orientation of the western strain transducer rosette is shown in figure 62b. In both locations the vertical strain transducer was placed two feet from the face of the bridge end bent (support). The rosette was positioned as close to the flange as possible based on the calculated estimate of the neutral axis location (appendix).

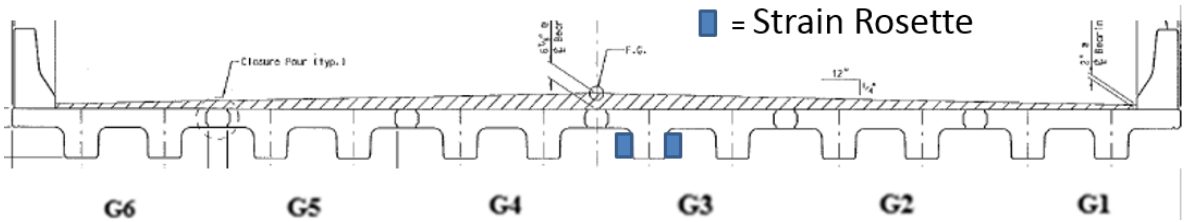

Figure 61: Torsion test strain transducer rosette locations

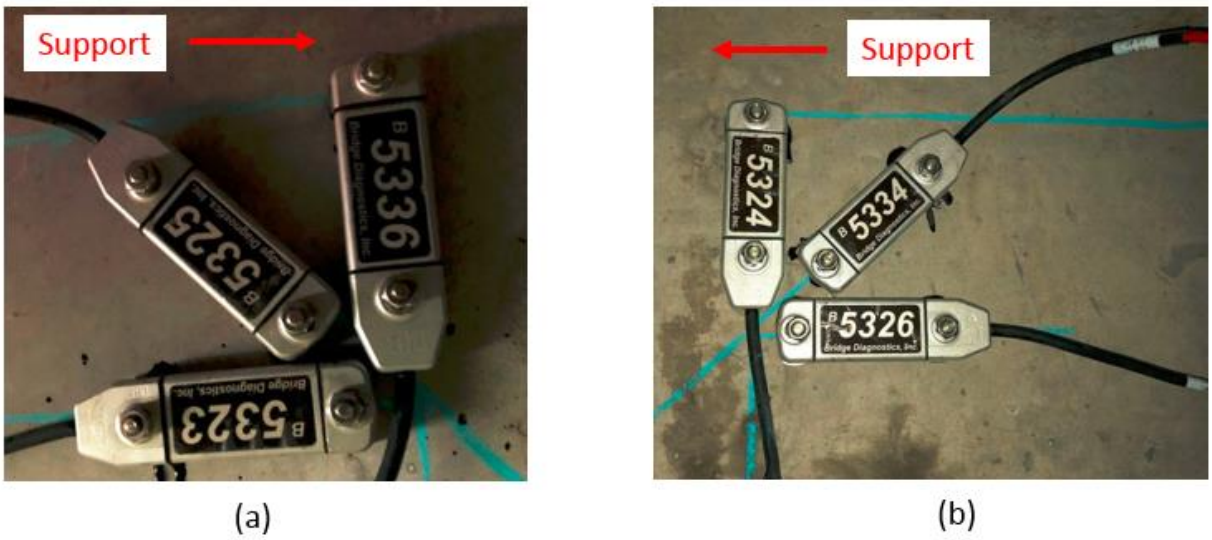

Figure 62: (a) eastern strain transducer rosette orientation and (b) western strain transducer rosette orientation

By instrumenting a strain transducer rosette on each side of a girder web, the torsional shear strain experienced by the instrumented web may be calculated. The calculation will be outlined in chapter 4.

3.2.6 LL Test Data Acquisition System

The LVDTs and strain transducers were the only instrumentation connected to the LL DAQ system. These instruments were connected to 4-channel nodes, which wirelessly sent the measured displacements and strain to the base station located onsite. Instruments need to only be attached to one channel and thus up to four instruments may be attached to each node. A laptop on which the measured data could be accessed and saved by the researchers was remotely connected to the base station. Also, the STS-Live software utilized to conduct the live load testing was managed from the laptop.

3.3 Evaluation Procedures

Visual inspection, Life-Span Technologies (LST), and live load (LL) test evaluation procedures are discussed throughout the remainder of this subchapter.

3.3.1 Visual Inspection and LST Bridge Evaluation

Visual inspections of the Hanging Rock Creek Bridge (HRB) NEXT-D and solid spans were conducted at the time of each live load test. Additionally, a visual inspection of the same spans accompanied with a photo survey was performed in September of 2018. Researchers especially inspected for reflective cracking on the bridge deck and cracking underneath the bridge that would be indicative of the UHPC to precast bond failing at the girder transverse joints.

Throughout the first year of the HRB life, experimenters accessed the online data of the LST sensors to discern any trends and piece together an evaluation of the health of the bridge. The LL tests were necessary to accompany the LST data and calibrate the LST data to perform a complete evaluation of the HRB NEXT-D and solid span girders.

3.3.2 LL Testing for LST Data Calibration and Girder Horizontal Displacements

Two LL tests were conducted considering the LST sensors. The first was conducted in January of 2018 (LL test 2) when the bridge was 7 months old and the second was conducted in May of 2018 (LL test 3) when the bridge was 11 months old. During, LL test 3 LVDT measurements alongside the LST sensor measurements were considered. Only LST and LVDT data generated from the single truck load cases was considered.

In figure 63 the truck weight and dimensions from LL test 2 are presented.

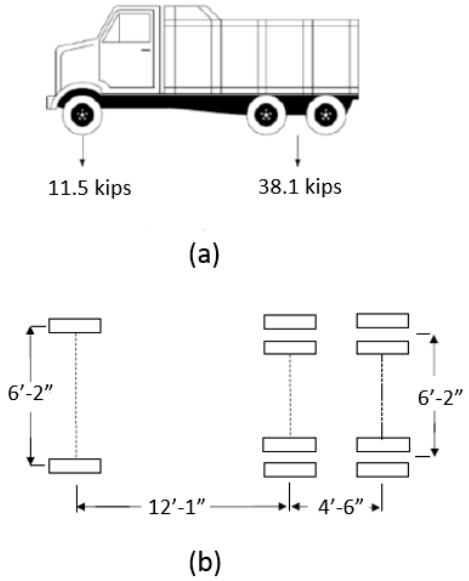

Figure 63: Truck weight (a) and dimensions (b) of truck used for LL test 2

In figure 64 the truck weight and dimensions from LL test 3 are presented.

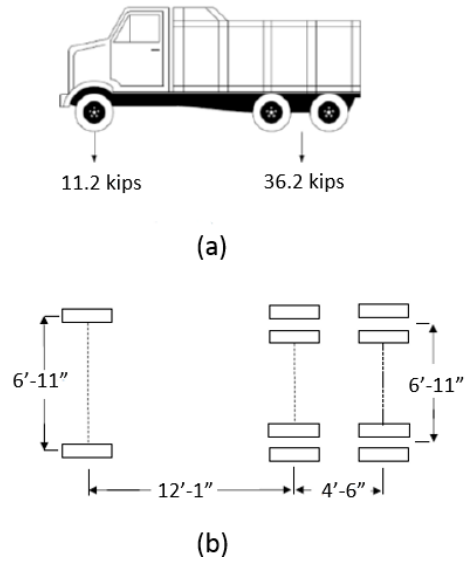

Figure 64: Truck weight (a) and dimensions (b) of truck used for LL test 3

In figures 65-67, the truck locations for LL test 2 are presented.

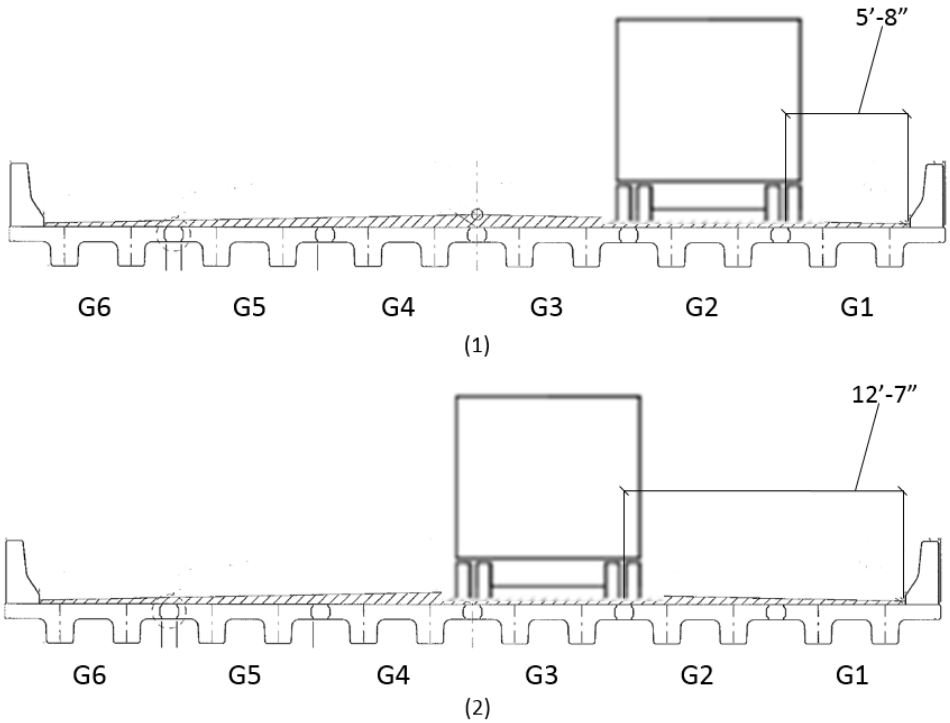

Figure 65: Truck locations on the NEXT-D span for LL testing of transverse joints

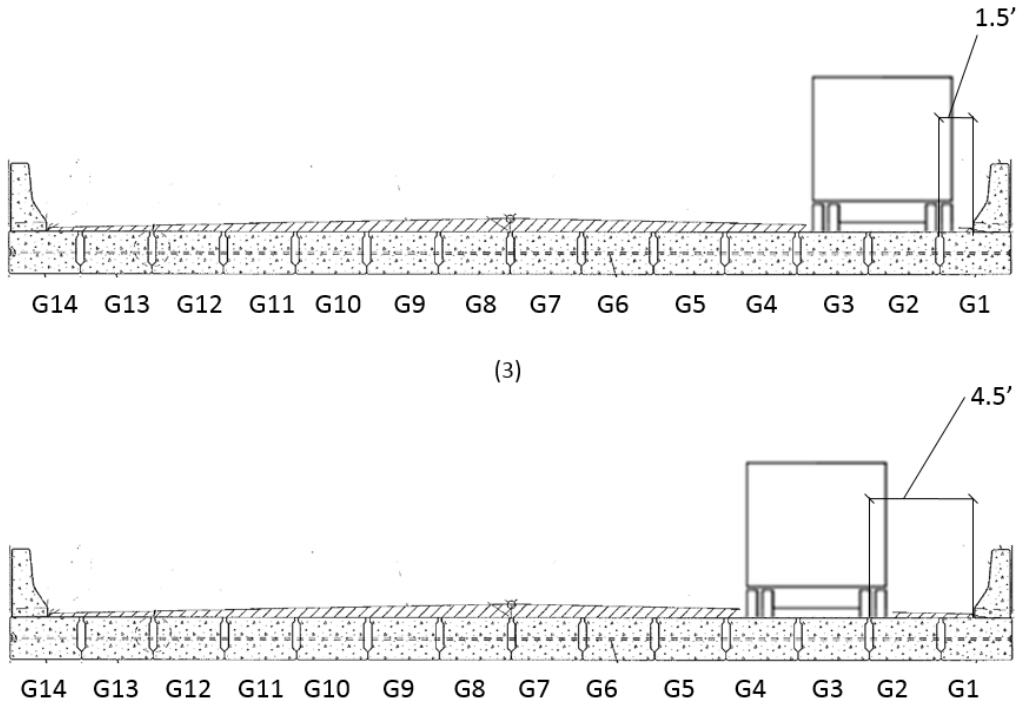

Figure 66: Truck locations on the voided span for LL testing of transverse joints

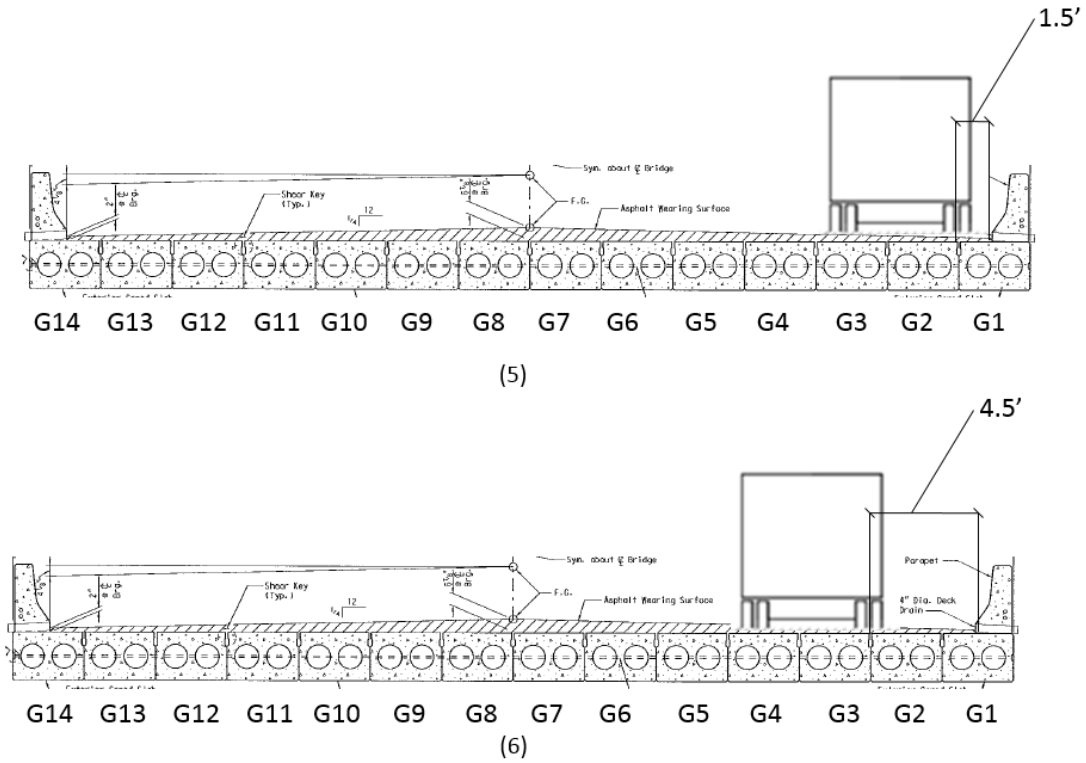

Figure 67: Truck locations on the solid span for LL testing of transverse joints

Figure 65 also displays the truck locations, for the acquisition of transverse data, during LL test 3. As mentioned before, LVDTs were attached directly next to the LST sensors during this LL test, as shown in figure 52, for a comparison of data between the LST sensors and LVDTs.

The LST LL tests (LL tests 2 and 3) were handled by measuring the response of the bridge before, while, and after being loaded. The loaded conditions were considered when the truck was parked at one of the critical locations along the bridge. The LST "Get Reading" function was used to collect data both while the bridge was in an unloaded state and loaded state.

During LL tests 2 and 3, researchers were on the bridge directing the truck to its respective static (parked) locations while one researcher was at a nearby local library (in order to access wifi) on the LST website collecting data. Figure 68 presents the loaded truck parked at one of the critical locations on the marked bridge during LL test 2. As discussed before, during LL test 3, LVDTs on the NEXT-D span were collecting data continuously while the truck was parked at and moving from each static location.

(a) (b)

Figure 68: Truck parked at one of the critical locations tested on the HRB

The LL testing of the solid span, during LL test 3 of the HRB, considered the displacement data of the LVDTs mounted at the girder to girder joints. Only single truck load configurations were considered for this LL test. The truck weight and dimensions of this LL test are presented in figure 64. The truck locations for this LL test are presented in figure 69. Visual inspection of the solid span in September of 2018 deemed it acceptable to cease LL testing of the solid span. Thus, during LL test 4 the relative horizontal displacements of the solid span were not tested.

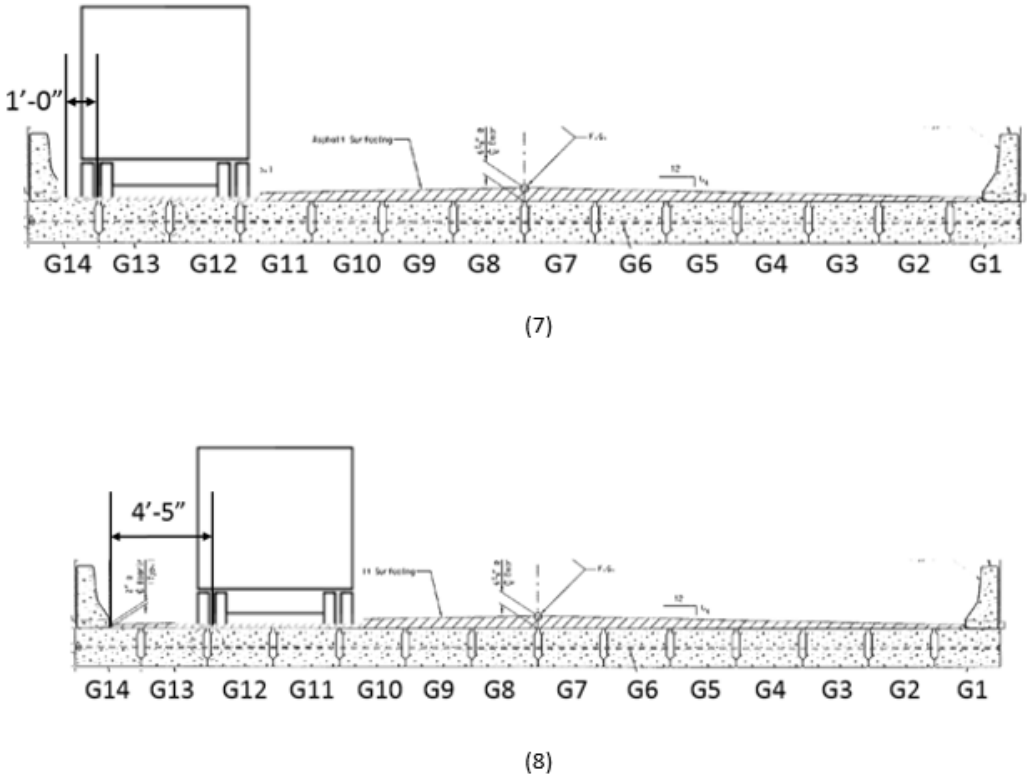

Figure 69: Truck locations on solid span for LL testing of transverse joints

During LL test 3, to evaluate the transverse condition of the solid span a crawling LL test was conducted; meaning, the truck drove slowly (less than 5 mph) along the span at its respective critical locations while data was collected.

The final transverse displacement LL test was conducted in October of 2018 (LL test 4) on the NEXT-D span only and considered data from the attached LVDTs alone. The truck weight and dimensions from this test are shown in figure 70. Figure 65 displays the truck locations for this final transverse displacement test.

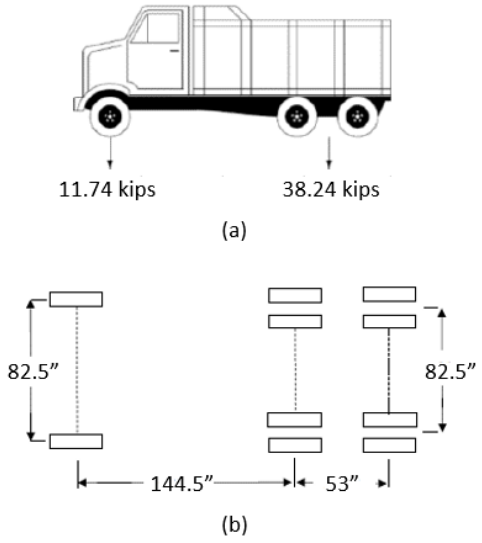

Figure 70: Truck weight (a) and dimensions (b) of truck used for LL test 4

During this final transverse displacement LL test, the LVDTs collected data as the truck crawled (traveled at speeds less than 5 mph) across the NEXT-D span.

3.3.3 Distribution Factor for Moment LL Testing

One aspect of the research for the purpose of this thesis was to measure distribution factors for moment (DFM) of the NEXT-D beams at different points in the Hanging Rock Creek Bridge (HRB) life. These DFMs were compared to those determined during LL test 1 conducted by Filosa (2017). DFMs of the NEXT-D beams were determined using data from the strain transducers attached during the LL tests conducted in May and October of 2018 (LL tests 3 and 4).

The weight and dimensions of the trucks used during LL test 3 to determine DFMs are presented in figures 64 and 71. The truck depicted in figure 64 was used for all single truck loading cases. During the double truck loading cases, the truck depicted in figure 64 was always closest to the barrier.

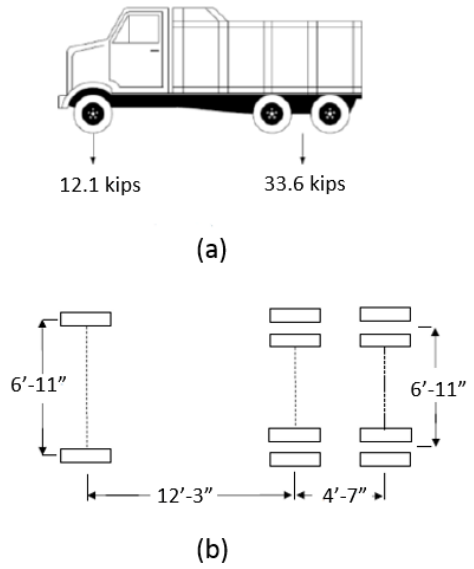

Figure 71: Truck weight (a) and dimensions (b) of truck used for LL test 3 DFM load tests

The truck weights and dimensions during LL test 4 are presented in figures 70 and 72. The truck depicted in figure 70 was used for all single truck loading cases. During the double truck loading cases, the truck depicted in figure 70 was always closest to the barrier.

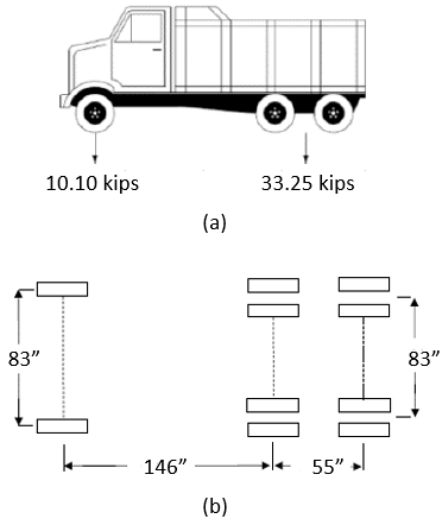

Figure 72: Truck weight (a) and dimensions (b) of truck used for LL test 4

The truck locations for determining DFMs during LL tests 3 and 4 are shown in figure 73.

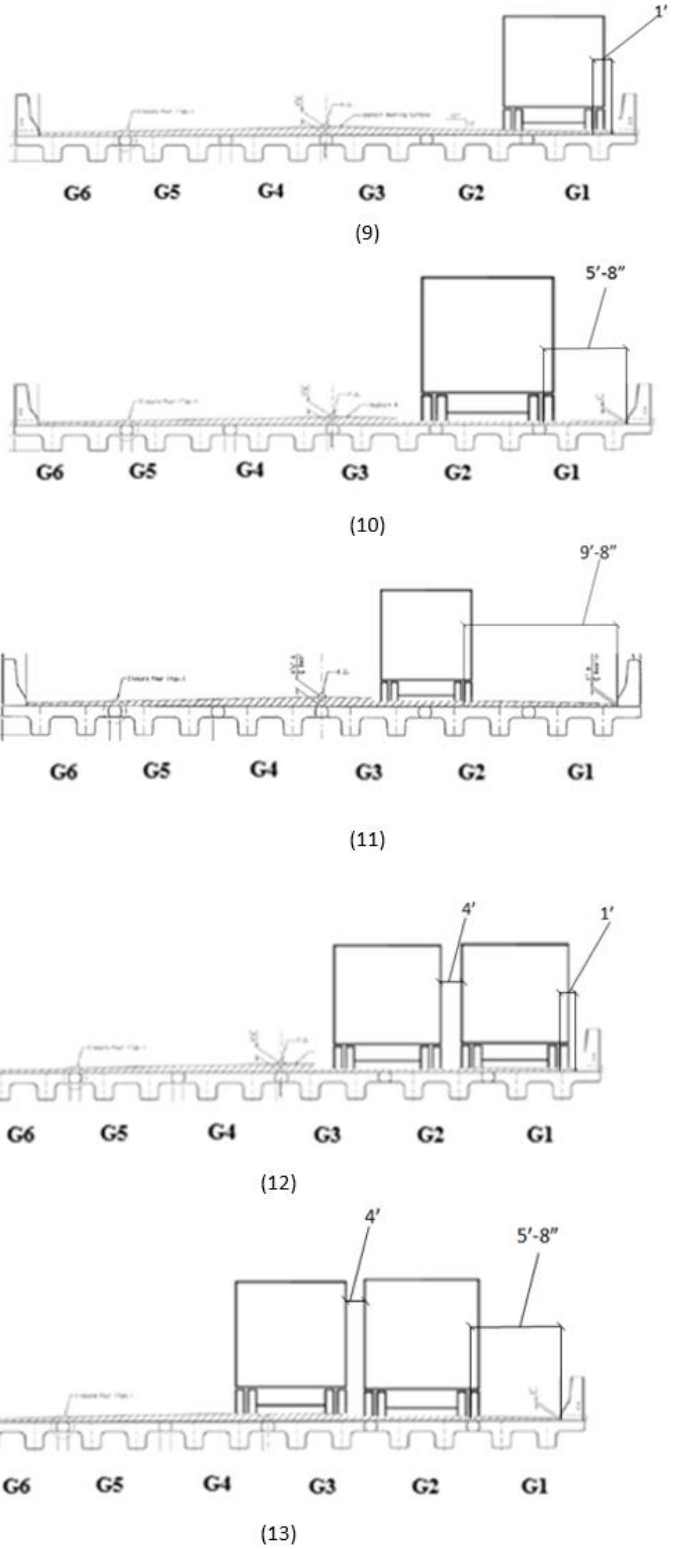

Figure 73: Truck locations for DFM and DFV calibration LL tests

The bending strain of the girders was collected during the DFM LL tests in May and October as the trucks traveled at speeds less than 5mph across the NEXT-D span. Using the strain data collected, researchers were able to calculate DFMs. This calculation process is outlined in chapter 4.

3.3.4 Distribution Factor for Shear Calibration and Torsion Test Testing

The LL test conducted for the calibration of the DFV strain data on the NEXT-D span was administered during LL test 3. During this LL test the collection of bending strain data (for the calculation of DFMs on the NEXT-D span) and the collection of shear strain data (for the calibration of DFV calculation methods on the NEXT-D span) was simultaneous. Thus, the truck weights and dimensions in figures 64 and 71 are the same trucks used for the DFV calibration LL test. The truck used in the double truck cases and the truck closer to the barrier rail in the double truck cases are the same as discussed in subchapter 3.3.3. Additionally, the truck locations for the DFV calibration LL test is the same as shown in figure 73.

The truck dimensions and weights used in LL test 4 for the torsion LL test are shown in figure 70. The location of the truck during the torsion LL test is shown in figure 74.

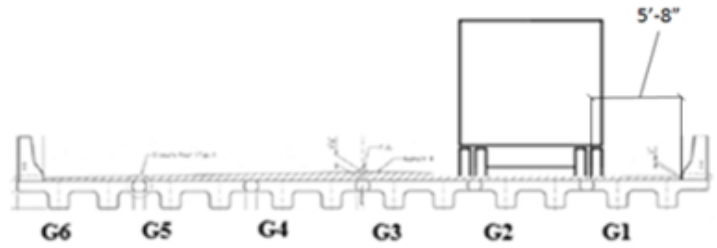

(14)

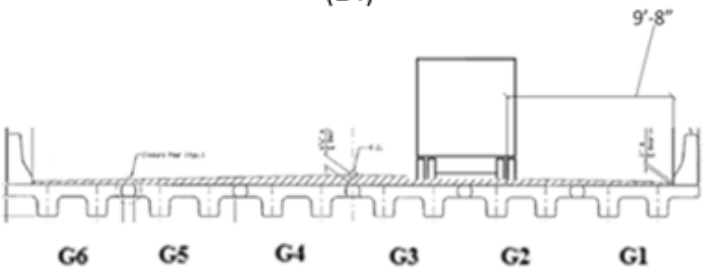

(15)

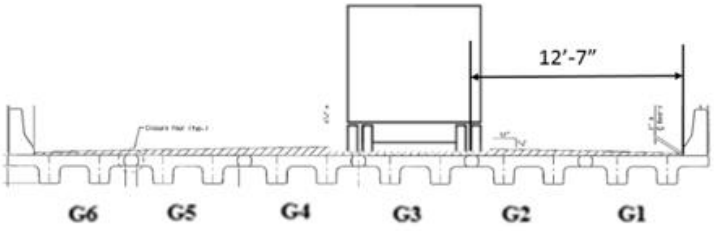

(16)

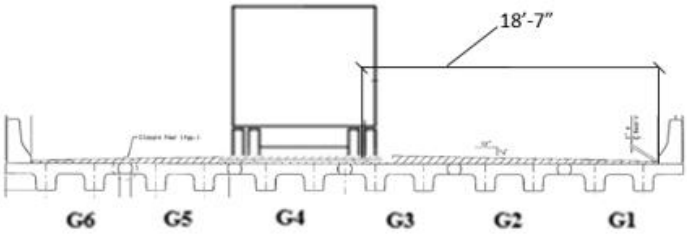

(17)

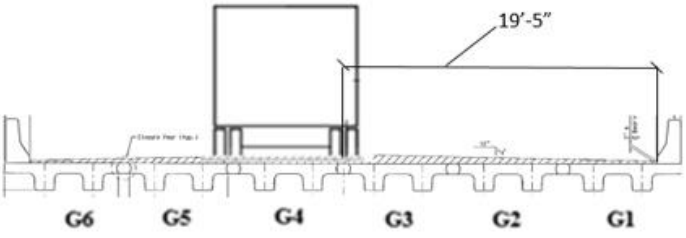

(18)

Figure 74: Truck locations during the torsion LL test

Crawling LL tests were conducted to collect the rosette strain data of the girders during both the shear strain calibration LL test during LL test 3 and the torsion LL test during LL test 4. Using the strain data collected during LL test 3 from the strain transducer rosettes, researchers evaluated the effectiveness of using one diagonal strain transducer per web to collect data from the NEXT-D beams for the calculation of DFVs. The strain data collected from the strain transducer rosettes during LL test 4 allowed the researchers to determine the influence level of torsion on the shear strain data calculated from the strain transducer rosettes.

Chapter 4: Results

Three live load tests were performed on the Hanging Rock Creek Bridge (HRB) to interpret and evaluate the Life-Span Technology (LST) sensors, evaluate the health of the bridge's shear key joints, calculate experimental distribution factors for moment (DFM), and evaluate the method for calculating distribution factors for shear (DFV). Additionally an earlier live load test was performed on the HRB by Filosa (2017) to evaluate the shear key joint health and calculate experimental DFMs. The results from Filosa are referenced where applicable for comparison purposes.

4.1 LST Load Test Results

The stresses and strains in pre-stressed girders are affected by live load, temperature change, and shrinkage and creep of concrete. The strains measured by the LST system at the transverse joints of the pre-stressed girders on the HRB should be reasonably captured within equation 14.

$$\varepsilon_{recorded} = \varepsilon_{temperature} + \varepsilon_{live\text{-}load} + \varepsilon_{shrinkage} + \varepsilon_{creep} + \varepsilon_{electronic\ drift} \qquad \textbf{Equation 14}$$

In this sub-chapter, the time line of major events, LST active/peak strain data, and LST temperature data during the first serviceable year of the HRB is presented. Additionally, the LST load test results (load tests 2 and 3), temperature correlation analysis results, and creep and shrinkage estimates are presented. Finally the condition of the HRB and an analysis of the LST system is discussed.

4.1.1 HRB First Serviceable Year Time-Line of Major Events

A time-line of the HRB bridge major events is essential for estimating shrinkage and creep strains and evaluating abrupt changes in strain measured. Shrinkage and creep strains are time-dependent, thus knowledge of girder casting dates increases accuracy in the estimates by the researchers of the strain due to creep and shrinkage. Regarding significant, immediate changes in strain, researchers may formulate informed estimates of events that influence the girder strains with a complete time-line of major events; such as construction activity, load tests performed, or an unknown event. Figure 75 displays the time-line of known major events on the HRB through its first year of serviceability, which represents the time frame the researchers evaluated the LST data.

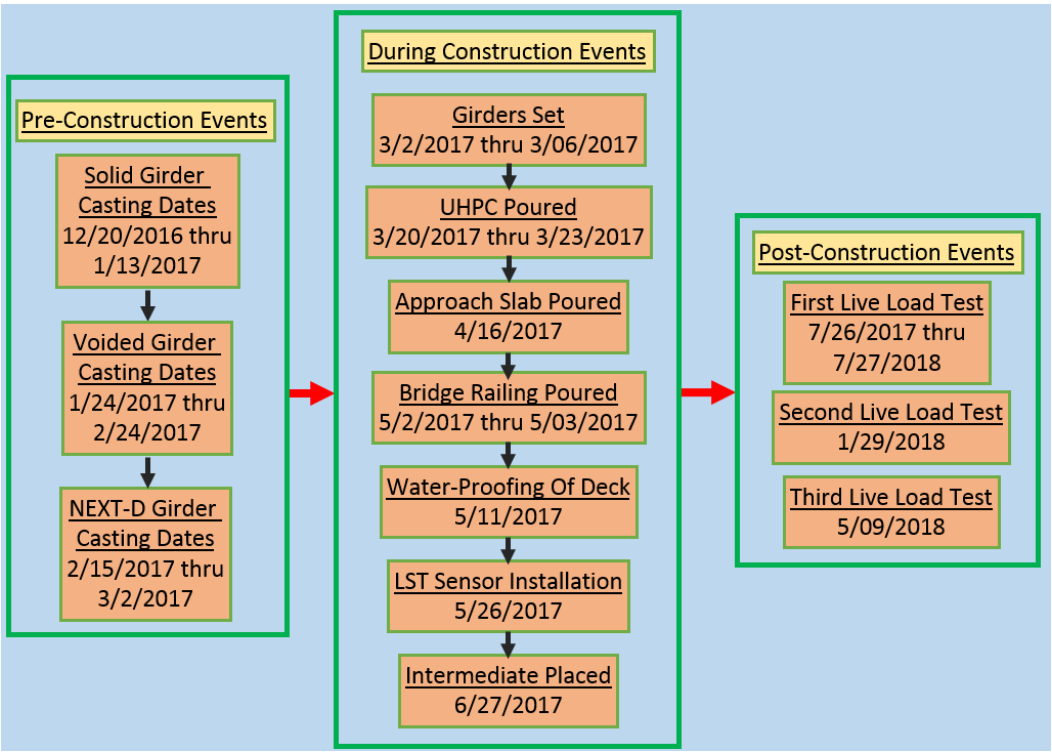

Figure 75: HRB time-line of major events

4.1.2 LST Strain and Temperature Data Collected

Active and peak strain (defined in subchapter 3.2.1) data from each sensor for the first year of the HRB serviceable life is presented. Additionally, the temperature readings from the same year for the NEXT-D span is presented. The sensors on the voided and solid slab spans did not collect temperature readings. The time frame selected for monitoring the LST sensors was chosen for multiple reasons. Firstly, this time frame includes the effects of the "events" recorded in the HRB time-line in figure 75. Secondly, this time frame includes both a hot and cold season to include the thermal effects on the NEXT-D span. Lastly, this time frame provides the data at the time of the second LST load test (LL test 3), allowing for a direct comparison between the results of the LST data and the data collected by linear variable displacement transformers.

The active and peak strains of the NEXT-D span are presented in figures 76 and 77.

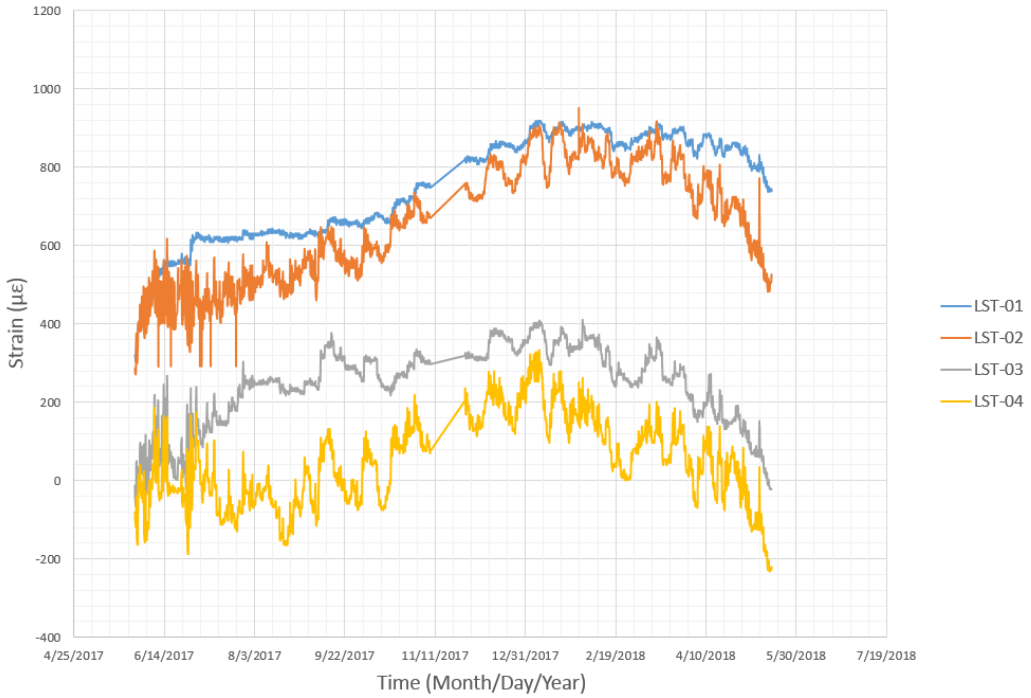

Figure 76: NEXT-D active strain readings from May 27th 2017-May 15th 2018

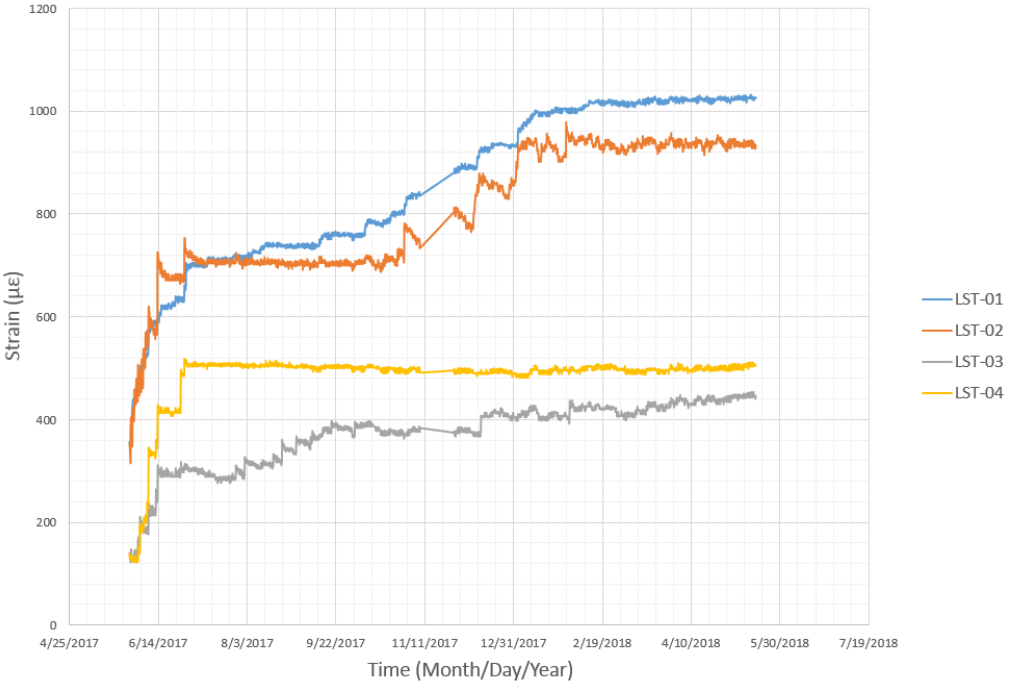

Figure 77: NEXT-D peak strain readings from May 27th 2017-May 15th 2018

The temperatures of the NEXT-D span are presented in figure 78.

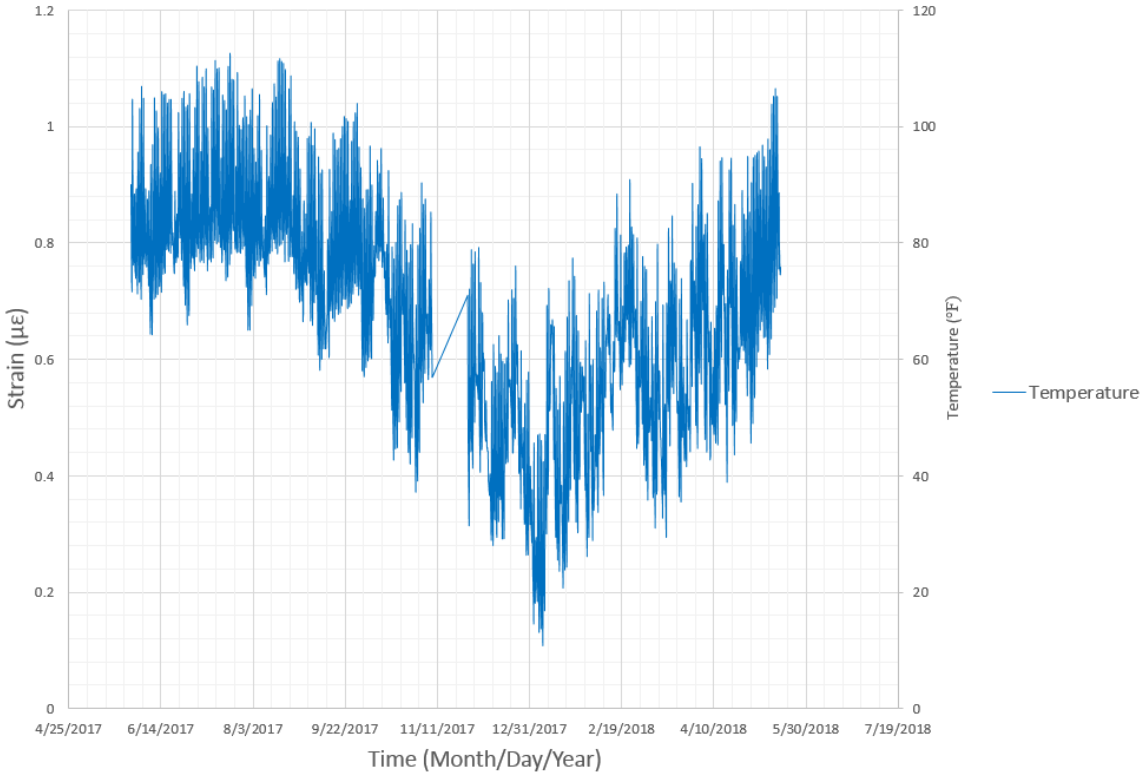

Figure 78: NEXT-D temperature readings from May 27th 2017-May 15th 2018

The active and peak strains of the voided span are presented in figures 79 and 80.

Figure 79: Voided span active strain data from May 27th 2017-May 15th 2018

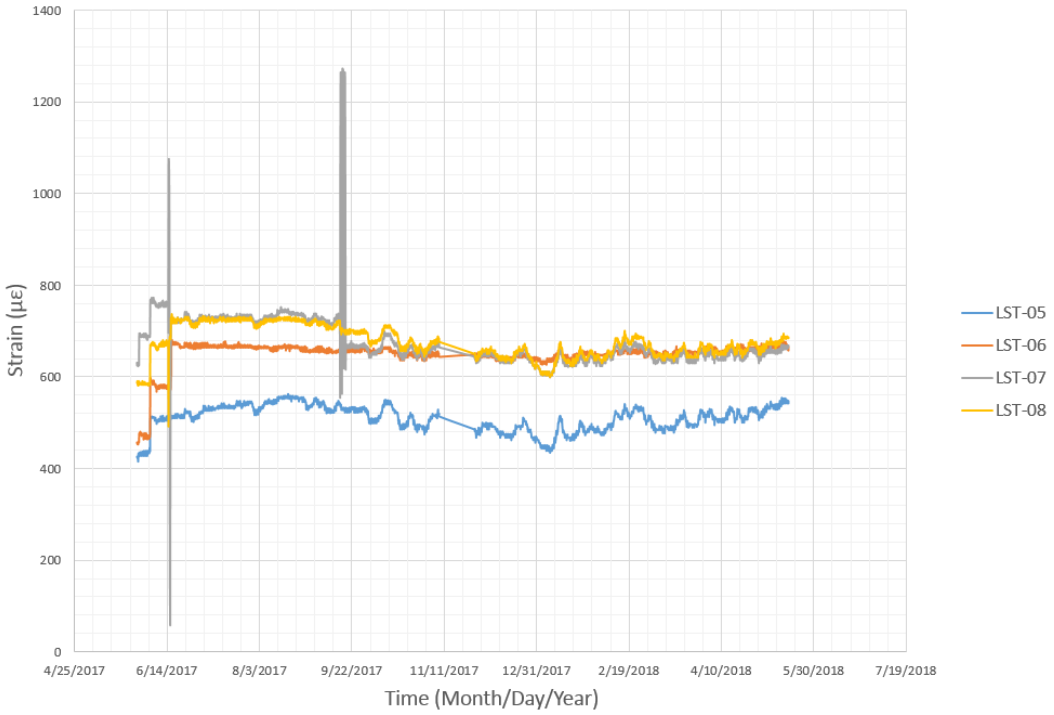

Figure 80: Voided span peak strain data from May 27th 2017-May 15th 2018

The active and peak strains of the solid span are presented in figures 81 and 82.

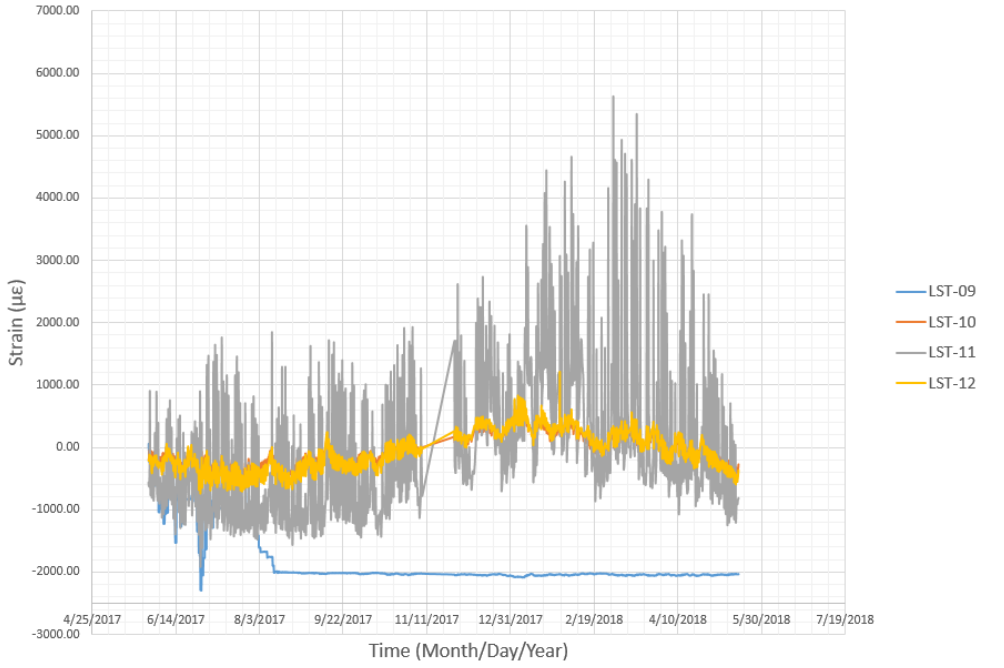

Figure 81: Solid span active strain readings from May 27th 2017-May 15th 2018

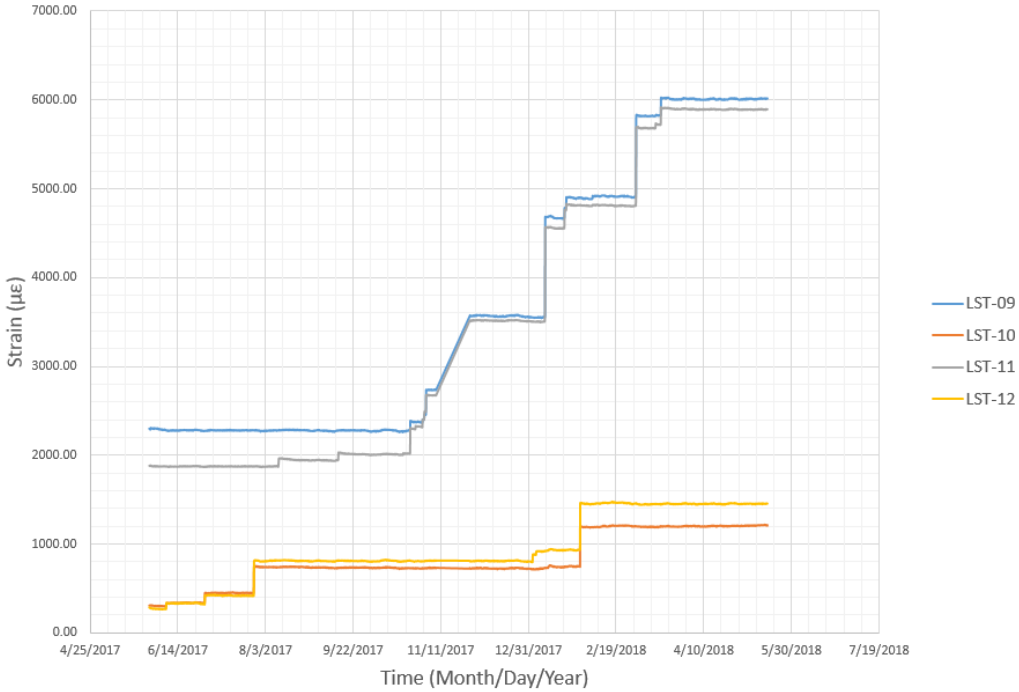

Figure 82: Solid span peak strain readings from May 27th 2017-May 15th 2018

Sudden increases in peak strain by the sensors on each span were not correlated to any major events recorded in the HRB time-line (figure 75). For example, consider the sudden peak strain increase of LST-03 (figure 77) on June 14th, 2017. The time-line of major events shows no major events on the 14th, thus the source of this sudden increase is not one of the major events recorded in the time-line. This process was considered for each sudden increase in peak strain for each sensor. It is concluded that none of the major events in the HRB time-line influenced the strain readings of the LST sensors.

Over the course of the year of LST data collection, several anomalies in the data were observed. Firstly, an anomaly that occurs in every data plot is the lack of data collection during part of October and part of November in 2017. For this reason, the strain and temperature cycles during this time period were not collected, and a trend-line between the data points that bookend the data drought has been assumed. Secondly, sometimes the sensors will report erroneous readings. This is most evident in the peak strain readings of sensor LST-07 which is located on the voided span. When strain readings of these magnitudes were collected, they were discarded and not considered when analyzing the sensors. Additionally, because of the way the peak strain readings are programmed, the peak strain plot should never decrease. Therefore, the decreasing slopes in the peak strain data collected by LST-02, LST-05, LST-07 and LST-08 is of concern. Further, the peak strains do not commence at a relatively similar strain reading as the active strains in any of the sensors. Finally, many of the strain plots do not commence at zero strain, which is another issue in effectively evaluating the strain data presented by the sensors.

4.1.3 Load Test 2 LST Results

A static load test was conducted in January of 2018 to develop known strains due to known truck loadings in the LST strain data. The data from this load test aids in populating the $\varepsilon_{\text{live-load}}$ variable in equation 14. Additionally, peak strain changes due to the applied live load and active strain magnitudes prior to the load test provide an understanding of the significance of live load on the strain measured in the LST sensors. Finally, since the data is not collected continuously, bar charts are used to display the data rather than a plot.

Figures 83 and 84 display the load test 2 results generated from sensors LST-02 (NEXT-D span) and LST-05 (voided span). All sensors on the NEXT-D span were tested during load test 2 and the sensors located at mid-span on the voided and solid spans were tested during load test 2. Figures displaying the results from the other sensors are located in the appendix. In figures 83 and 84, "Initial Peak" describes the peak strain measured before the static load test and "Final Peak" describes the peak strain measured after the static load test. "Delta" describes the change in strain measured by the sensor due to the truck loading. During load test two strain was recorded by the sensors before, during, and after loading. Thus, there are three "bars" in figures 83 and 84 representing the load test strain. In figure 84, the bars are negative which indicates strain recordings at this joint are experiencing compression. A decrease in compressive strain under load indicates that the joint "opened". Table 11 shows the correspondence between each sensor load tested and the respective truck load case.

Table 11: Correspondence between tested sensors and truck load cases (locations)

Sensor Load Tested	Truck Configuration
LST-01 & LST-02	1
LST-03 & LST-04	2
LST-05	5
LST-06	6
LST-09	3
LST-10	4

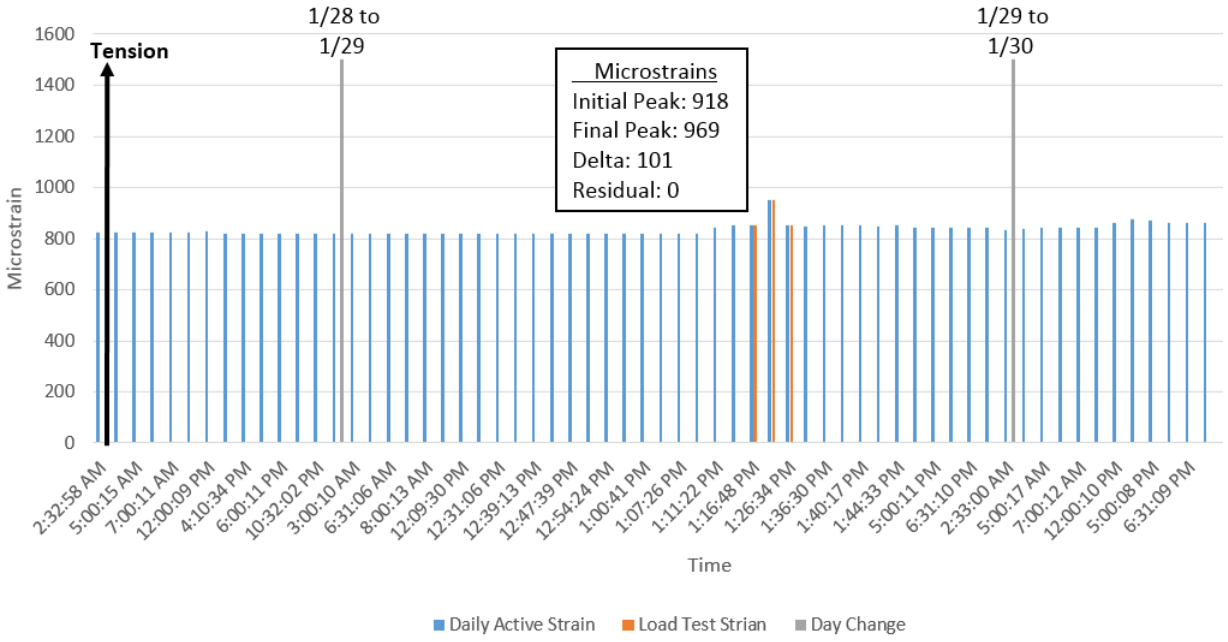

Figure 83: Load test results of sensor LST-02

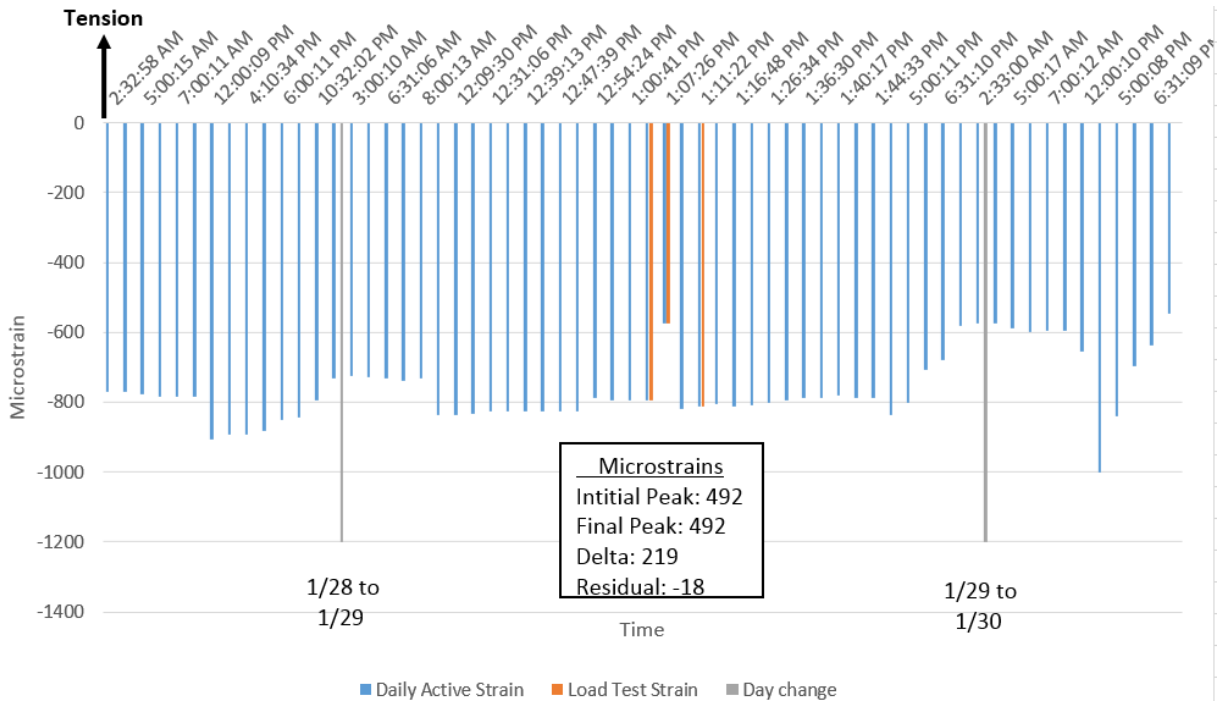

Figure 84: Load test results of sensor LST-05

The changes in strain measured due to the truck loadings are of interest since they are representative of the magnitude of strain influenced by the live load. A summary of the changes in strain measured for each sensor tested is provided in table 12.

Table 12: Change in strain measured due to the truck loading for each sensor tested

Gauge	Δ με due to live load
LST-01	0
LST-02	101
LST-03	11
LST-04	97
LST-05	219
LST-06	442
LST-09	0
LST-10	853

The results indicated that the same live load magnitude horizontally strained the shear key-girder interfaces on the solid and voided spans more than on the NEXT-D span. Assuming rigid body motion, it is expected that larger horizontal strains would be measured on the solid and voided spans since their girders are deeper at the shear key than the girders on the NEXT-D span.

Relative to the absolute magnitudes of the active strains at each sensor, live load did not significantly increase the horizontal strain experienced at the girder-shear key interfaces on the NEXT-D span except at sensor LST-04. The sensor peak strains also did not increase except in LST-02. Thus, on the NEXT-D span live load is not a significant contributor to the strain reported. The data from the sensors measuring live load strains on the voided and solid spans indicates that live load significantly increased the tensile strain measured relative to the current active strains. Peak strain only changed in one of the sensors but at the time of load testing the data indicated that the joints were under compressive strain (negative active strain recorded). Therefore, it is assumed that live load has a significant influence on the strain measured on the solid and voided spans.

Three sensors recorded negligible changes in horizontal strain under live load (sensors LST-01, LST-03, and LST-09). Since the joints are expected to experience some amount of change in strain under load, these sensors were considered suspect. Thus, LST sensors were compared to measurements from other instrumentation in live load test 3.

4.1.4 Load Test 3 LST Results

The purpose of this live load test, regarding the LST sensors, was to compare the LST sensor data to calibrated linear variable displacement transformer (LVDT) data on

the NEXT-D span. A comparison of data was performed because of the anomalies present in the LST data and the suspect LST sensors. The data comparison was restricted to the NEXT-D span to initially evaluate the cause of the LST data anomalies and live load test 2 suspect sensor displacements.

The LST sensors report strain while the LVDTs report displacement. Thus, using the sensor lengths given by LST, the strain was converted to displacement for the purpose of comparing to the LVDTs. Figure 85 shows the LVDT data collected on the NEXT-D span for load case 1. LVDT data was collected for load cases 1 and 2 which cause the maximum response in the LST sensors and LVDTs on the NEXT-D span. Figures 86 and 87 compares the maximum displacements recorded by the LVDTs to the displacements calculated from the LST strain data recorded for truck locations 1 and 2.

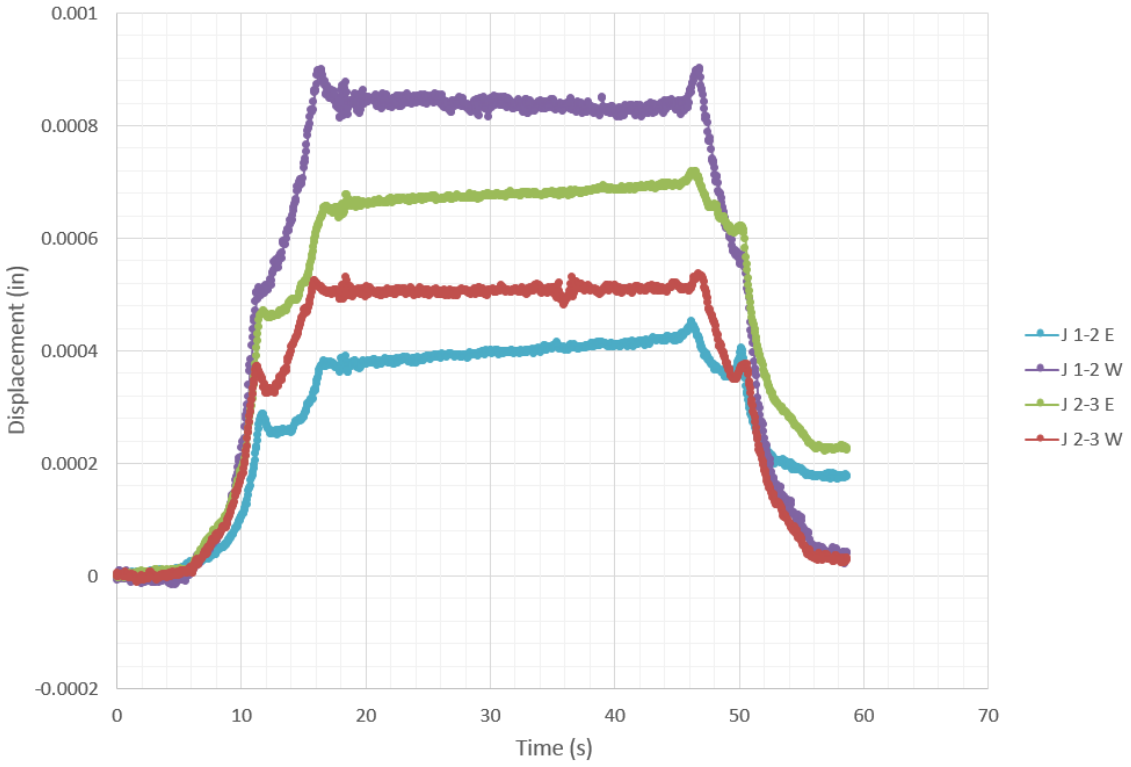

Figure 85: LL Test 2 LVDT data collected for load case 1

The nomenclature for the legend provided in figure 85 is discussed by considering label “J 1-2 E”. In this label, the joint considered is the eastern joint between girders 1 and 2. The LVDT data has an initial plateau when the front wheel passes over the location of the LVDT (approximately 12s) and has an extended plateau while the back axle rests over the location of the LVDT. The extended plateau occurs in the data because LST data was collected while the truck was stationary over the LVDT and LST sensor.

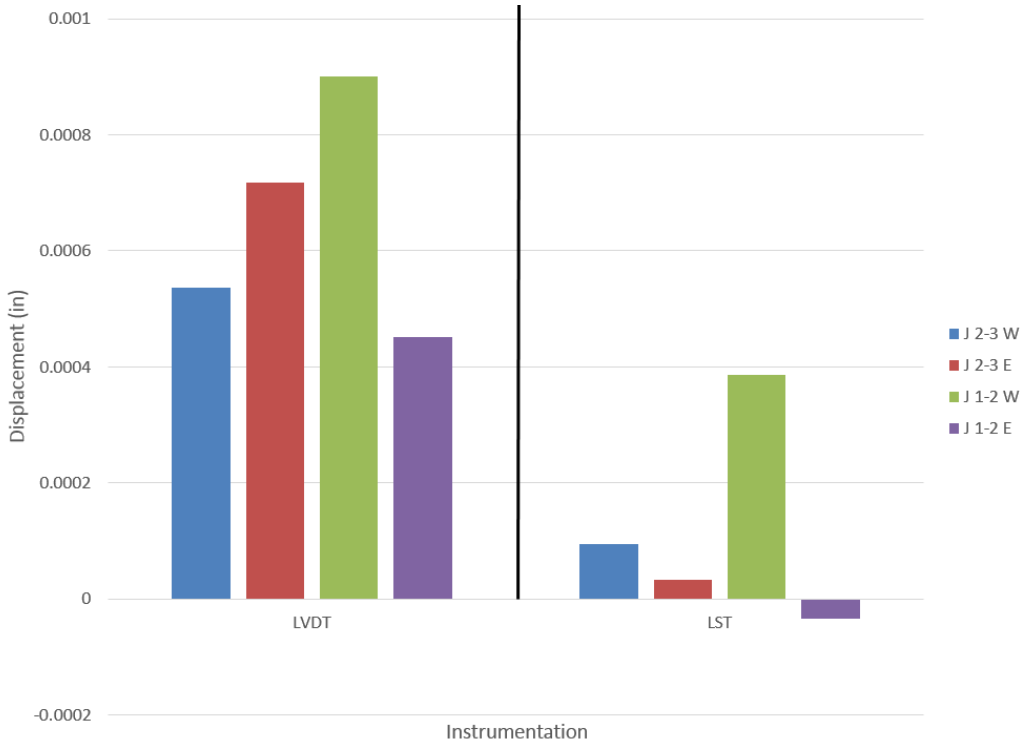

Figure 86: Comparison of LVDT data to LST data for truck location 1

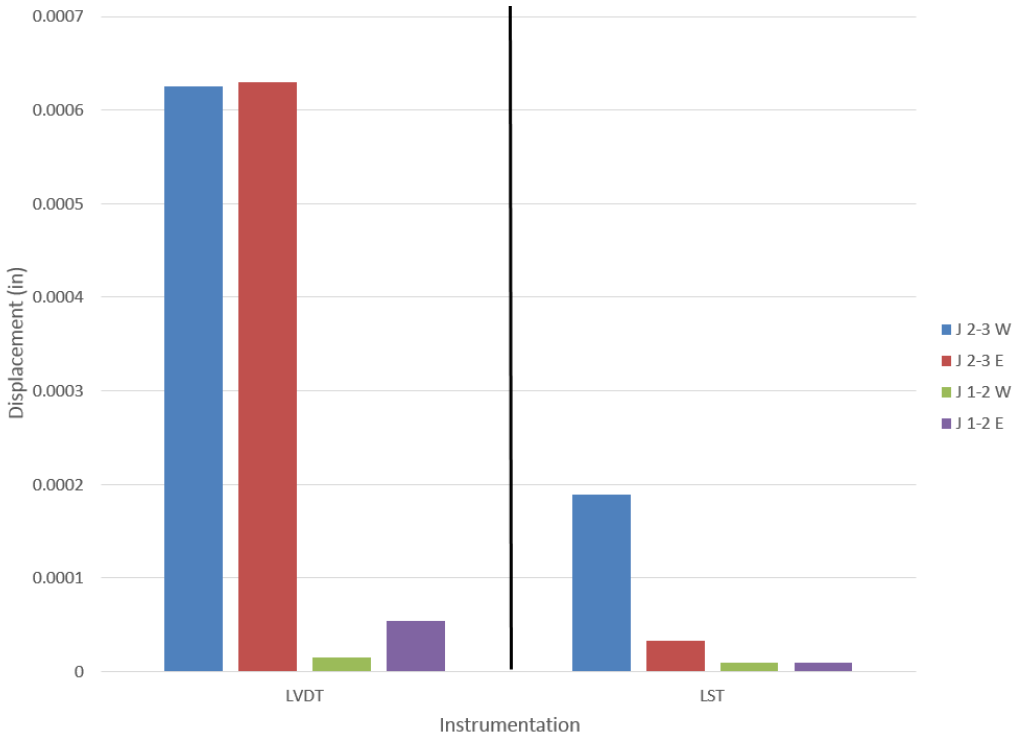

Figure 87: Comparison of LVDT data to LST data for truck location 2

After the initial comparison assessment, it is clear that in several cases the LST data does not report the same change in displacement as the LVDTs. Considering that some LST sensors displayed a negligible response under live load, the LVDTs (which always displayed a response under direct live load) were considered to record more accurate results. The researchers also determined at this point to not compare the LST sensor data on the voided and solid spans to LVDT data because the comparison analysis provided conclusive results on the NEXT-D span.

4.1.5 Temperature-Strain Correlation Analysis Results

Temperature readings were only collected by the sensors on the NEXT-D span. Thus, the correlation analysis is only implemented on the NEXT-D span. In order to accurately attribute strain due to temperature, the temperature gradient between the top

and bottom of the NEXT-D girder flange must be known. This gradient was not measured by the LST sensors, therefore the NEXT-D flange is assumed to experience a uniform temperature gradient between the top and bottom of the flange for the purpose of this analysis, and only rough estimates of the strain measured due to temperature can be evaluated. Before commencing the correlation analysis, it was conservatively estimated that a yearly thermal cycle would contribute 730 micro-strain to the strain measured in the sensors on the NEXT-D span.

Two correlation analyses were considered over a yearly thermal cycle. The first analysis considered the correlation between temperature and active strain and the second analysis considered the correlation between decreasing temperature and peak strain. The correlation coefficients (CC) and r-squared values (R^2) are calculated for each study. A positive CC indicates that the strain increased as temperature increased and a negative CC indicates that the strain increased as temperature decreased. The R^2 value represents what portion of the variability in active strain or increase in peak strain can be attributed to temperature variability or temperature decrease respectively, and is calculated by squaring the CC. Table 13 displays the results of the correlation analysis.

Table 13: Results of the correlation analysis

Temperature Correlation Analysis				
	LST-01	LST-02	LST-03	LST-04
Active CC	-0.678014	-0.90053	-0.54588	-0.67142
Peak CC	-0.95866	-0.95447	-0.81953	-0.30644
Active R^2	0.4597031	0.810962	0.297989	0.450801
Peak R^2	0.9190281	0.911018	0.671632	0.093908

After completing the correlation analysis, it is evident that there is generally a negative correlation between temperature and active strain at the transverse shear key joints and also between temperature and peak strain increase at the transverse shear key joints. The negative correlation is more pronounced in the latter than in the former. Typically, a decrease in temperature causes compressive strain, but it is assumed that because the girders and UHPC fill are stiffer than the bond at the precast-UHPC interface, the compression of the girders and the UHPC fill at the precast-UHPC interfaces cause the interfaces at the joints to experience tensile strain, thus tensile strain increases were measured by the sensor during temperature decreases.

Figure 88 is a plot of active strain, peak strain, and temperature measured by LST-01. This plot exemplifies the negative correlation between measured strains and temperatures on the NEXT-D span (although much stronger in some sensors than others). It is evident that when the temperature begins a decreasing trend, the active and peak strains begin an increasing trend. The significant increase in strain just after installation of the sensors is assumed to be primarily due to shrinkage effects.

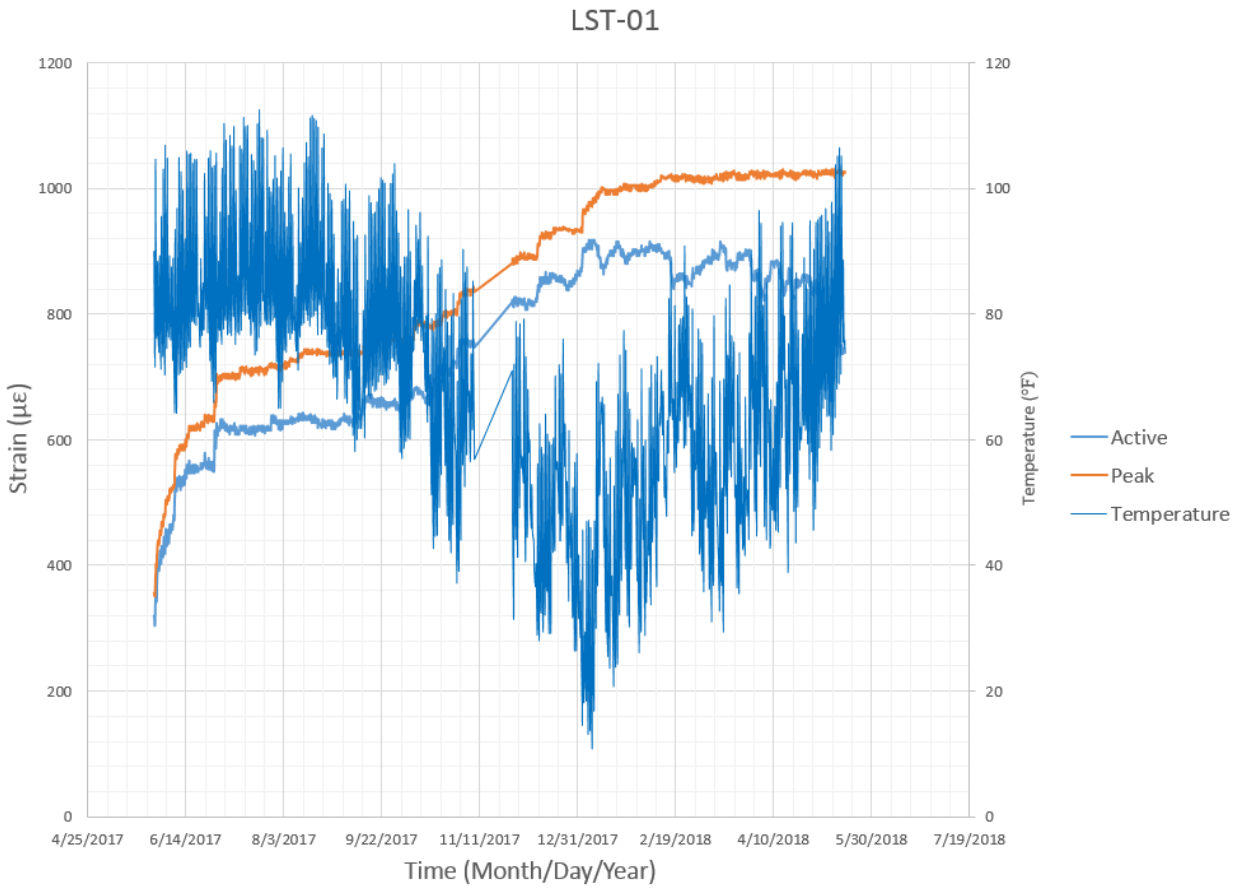

Figure 88: Relationship between active strain, peak strain, and temperature

The r-squared factors calculated from the correlation analysis indicate that up to 91% of the peak strain measured may be due to temperature effects for sensors LST-01 and LST-02. Considering the magnitude of the peak strain measured at the time of the second LST load test, this would result in estimates of up to 930 micro-strain, which is outside of the thermal estimate of 730 micro-strain. Considering the peak strain range measured from sensor installment to load test 3, this would result in estimates of up to 600 micro-strain being attributed to temperature, which is within the thermal estimate of 730 micro-strain. Therefore, the peak strain range is best to consider when estimating the

influence of temperature on the strains measured in LST-01 and LST-02. As discussed before, these are rough estimates since the temperature gradient is unknown, however, it is clear that temperature has a significant effect on the strain measured in sensors LST-01 and LST-02.

The r-squared factors for sensor LST-03 suggest that 67% (200με) of the peak strain measured may be attributed to temperature effects. Sensor LST-04 indicated a negligible correlation between peak strain and temperature.

The difference between the r-squared factors for active strain and peak strain for each sensor may be attributed to active strain continuing to increase and decrease due to events other than temperature change while large peak strain magnitudes remain constant. Peak strain may sometimes increase due to other events as well, however the primary event increasing peak strain is temperature. Temperature may not always be the primary event causing varying active strains.

Due to the significant negative correlations measured between temperature and increasing peak strain, it is likely that temperature is a primary influence on the strain measured by the LST sensors (excluding LST-04) on the NEXT-D span. However, as stated before, it is difficult to accurately attribute the magnitude of strain measured due to temperature since the temperature gradient is unknown. Therefore there is significant uncertainty in the contribution of temperature effects on transverse strain.

4.1.6 Estimated Strain Due to Shrinkage and Creep on the NEXT-D span

A rough estimate of thermal strain at the girder transverse joints was only evaluated on the NEXT-D span. Thus, to evaluate equation 14, shrinkage and creep strain are only estimated for the NEXT-D span.

Creep strain in concrete is caused by sustained compressive stresses. On the HRB the only sustained compressive stress present in the transverse direction of the girders is due to the transverse post-tensioning. Transverse post-tensioning is not applied on the NEXT-D span however, so the creep strain in the transverse direction on the NEXT-D span is considered negligible.

The conservatively estimated shrinkage strain in the girders on the NEXT-D span was determined from equation 15 (Wight, 2016).

$$(\boldsymbol{\varepsilon_{sh}})\mathbf{t} = \frac{\boldsymbol{t}}{\mathbf{35}+\boldsymbol{t}} \times (\boldsymbol{\varepsilon_{sh}})\mathbf{u} \qquad \textbf{Equation 15}$$

$(\varepsilon_{sh})_t$ = Time-dependent strain

t = time (days)

$(\varepsilon_{sh})_t$ = Ultimate strain due to shrinkage (conservatively used as 1070×10^{-6})

To estimate the shrinkage strain in the girders that occurred after the LST sensors were installed, the shrinkage strain that occurred after the girder was cast through the installation of the LST sensors was subtracted from the shrinkage strain that occurred after the girder was cast through one year of LST data reported. The latest girder cast was cast 87 days before the installation of the LST sensors. The time from the casting of the last girder until approximately 1-year passed after the LST sensors were installed was 440 days. Thus, it was determined that a conservative estimate for shrinkage strain in the

NEXT-D girders after the LST sensors were installed is 228 micro-strain. Although a conservative estimate of shrinkage strain on the NEXT-D span is estimated, the exact shrinkage strain of the NEXT-D span is difficult to evaluate.

4.1.7 Discussion of Significant Events and Evaluation of Condition of Each Span

In this section, each span will be discussed regarding the peak strain measured since significant changes in strain are best captured by the peak strain. Thus, considering known peak strain effects for each sensor is best for evaluating the span conditions. Additionally, a discussion regarding the LST system's ability to capture the HRB condition is considered.

On the NEXT-D span, increases in the peak strain could be attributed to live-load, thermal effects, shrinkage, and electronic drift, however, relatively exact estimates can only be attributed to the live load. The maximum strains measured are within the conservative maximum strain estimated using equation 14. For example, the conservative estimates for thermal, shrinkage, and live load strains in sensor LST-02 are shown populated in equation 14 below. The actual maximum strain recorded considering the strain range is approximately 650με. The recorded strain is reasonable considering that the estimate is very conservative and is far from exact. It is difficult to determine exact thermal strains because of the unknown temperature gradient. Additionally the best estimates for thermal strain and the maximum strain recorded are based on the range of the peak strain measurements rather than the magnitude of the peak strain measurements, which makes it difficult to interpret meaning from the strain magnitudes measured. Conservative shrinkage strain estimates indicated that only a fraction of the peak strain

measured may be attributed to shrinkage. Finally, none of the abrupt changes in the peak strain data coincided with significant events on the timeline of the HRB.

$$\varepsilon_{recorded} = \varepsilon_{temperature} = \sim 600\mu\varepsilon + \varepsilon_{live\text{-}load} = \sim 100\mu\varepsilon + \varepsilon_{shrinkage} = \sim 230\mu\varepsilon + \varepsilon_{electronic\ drift} = \sim unkown = \sim 930\mu\varepsilon$$

On the voided and solid spans, increases in the peak strain may be attributed to live-load, thermal effects, shrinkage, and electronic drift, however, relatively exact estimates can only be attributed to the live load. Temperature effects were not measured and thus shrinkage and creep strain was not estimated since without thermal strain estimates equation 14 cannot be evaluated. Finally, none of the abrupt changes in the peak strain data from the voided and solid spans coincided with significant events on the timeline of the HRB.

Since peak strain data does not commence at a magnitude of zero strain in any of the installed sensors, electronic drift may be occurring in the LST data. Additionally, it is difficult to determine the exact magnitude of thermal, shrinkage, and creep strains measured in any of the sensors, which allows for the consideration that electronic drift may be occurring. Finally, considering the other aforementioned anomalies that have occurred over the course of data collection (subchapter 4.1.2), it is assumed that some amount of electronic drift is occurring. Therefore, there is reduced confidence in the meaning of the data collected by the LST sensors.

During live load test 2, some sensors on the NEXT-D and solid spans reported negligible strain under load and were thus considered to be suspect. During live load test 3, two of the three “suspect” sensors’ data on the NEXT-D span was compared to data

from LVDTs instrumented at the same joint. After the evaluation, the suspect LST sensors still reported negligible strain while their LVDT counterparts reported meaningful results. Additionally, none of the sensors reported data within 50% of the LVDT reported data.

The LST system provides strain data over time, however, there is uncertainty regarding the other effects on strain (specifically temperature which is a significant contributor to transverse strain on the NEXT-D span). Also there is not a constant recording of data, so significant responses in strain that do not create "new" peaks are not captured. Finally, the anomalies and apparent electronic drift in the LST system and the discrepancy between the LST sensor data and LVDT data is unexplained. Therefore, the span conditions of the HRB cannot be determined from the LST system data alone.

4.2 Transverse Displacement Results

Relative horizontal displacements at girder-shear key interfaces were measured at select joints on the NEXT-D and solid spans. Displacements were measured on the NEXT-D span during live load (LL) tests 3 and 4 and displacements on the solid span were measured during LL test 3.

4.2.1 NEXT-D Girder Joint Behavior

Relative horizontal displacements were measured at select shear keys on the NEXT-D span to evaluate the health (degradation and cracking) of the NEXT-D shear keys. On the NEXT-D span, if a crack forms at one of the shear key-girder interfaces, the Linear Variable Displacement Transformer (LVDT) instrumented at the cracked interface would experience a significant displacement increase relative to the LVDT at the adjacent

interface (on the same joint), and the displacement would be significantly larger than the displacements of other instrumented interfaces (if they are un-cracked). Five LVDT locations were selected for LL test 3 and six LVDT locations were selected for LL test 4. The number of locations selected correlated to the number of operable LVDTs at the time of the load tests. The locations selected considered the location of the LST sensors for purposes discussed in the previous subchapter and considered the location of the LVDTs instrumented in LL test 1 to allow for a direct comparison to data from LL test 1. Additionally, reflective cracking was considered for the location of the LVDTs during LL tests 3 and 4, however, during visual inspection of the bridge deck just before both load tests, no reflective cracking was evident on the NEXT-D span. Thus, in the end reflective cracking did not influence which NEXT-D joints the researchers chose to instrument.

The LL test 3 real-time displacements of the interfaces instrumented are presented in figures 89 and 90. In figures 89 and 90, the joint interfaces directly below the wheel lines experience tensile displacement (joint opening) and the joint interfaces away from the truck experience compressive displacement (joint closing). Considering the increasing slopes in figure 89, the front axle crosses over the instrumentation at approximately 12s (where the first plateau appears). The back axle is stationary at the joint from approximately 15s to 47s, then the truck completes its crossing of the NEXT-D span. The reason for the back axle remaining stationary for approximately 30s was for the purpose of collecting LST data to compare to the LVDT data as discussed in subchapter 4.1. Similar behavior to case 1 is observed for case 2 (figure 90). In both cases, the joints do not experience a maximum displacement of more than 0.0009 inches. The maximum joint

interface displacement from LL test 1 was 0.001 inches (Filosa, 2017). Additionally, reflective cracking of the bridge deck and effervescence underneath the bridge was not evident. Thus, joint degradation and cracking is assumed to not have occurred on the NEXT-D span of the HRB during its first in-service year (between LL tests 1 and 3).

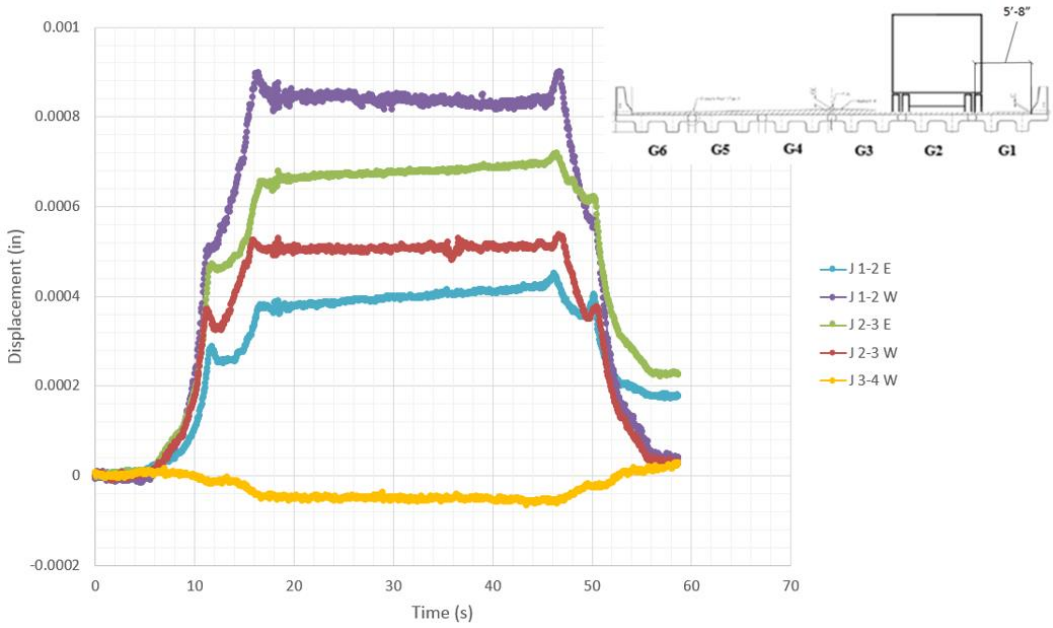

Figure 89: Girder-shear key interface displacements from truck location 1 during LL test 3

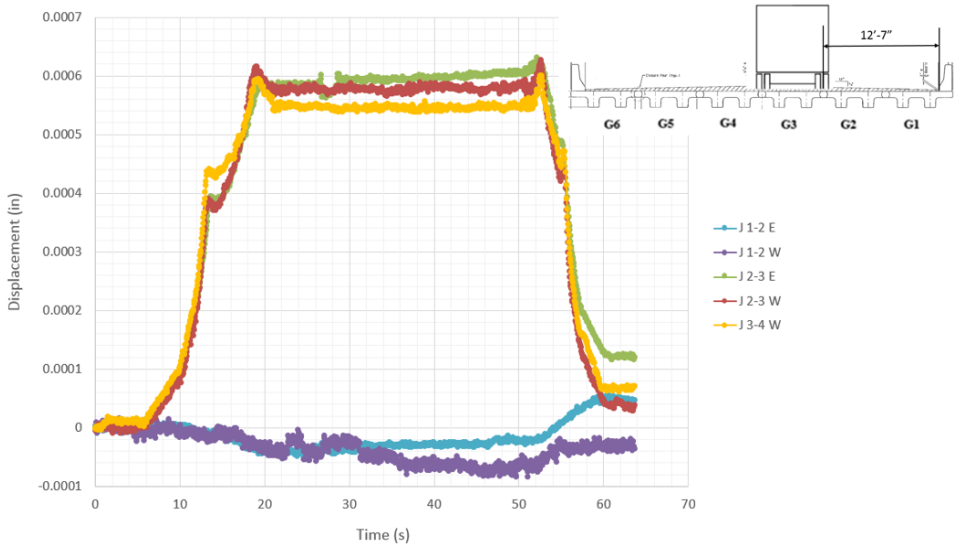

Figure 90: Girder-shear key interface displacements from truck location 2 during LL test 3

The nomenclature of the legend in figures 89-92 is best explained considering “J 1-2 E”. This label is referring the eastern joint between girders one and two. The cross sections shown in figures 89-92 are considering north as “into the page”.

Approximately two weeks before LL test 4, the NEXT-D span was visually inspected and photographed. The photo survey (see appendix) indicates that a transverse crack formed near the western barrier at the interior support (interior bent). Additionally, two patches on the eastern side of the bridge are noted in the photo survey. The two patches were first observed during LL test 2 and the purpose of the patchwork is unknown. No other cracking was evident on the NEXT-D span. During the visual inspection of the NEXT-D span, no effervescence was evident at any of the girder-girder joints beneath the bridge. Thus, the LVDTs were placed at the same locations they were placed during LL test 3 since there were no reflective cracks on the NEXT-D span bridge deck and no effervescence present beneath the NEXT-D span.

The real-time displacements of the interfaces instrumented during LL test 4 are presented in figures 91 and 92.

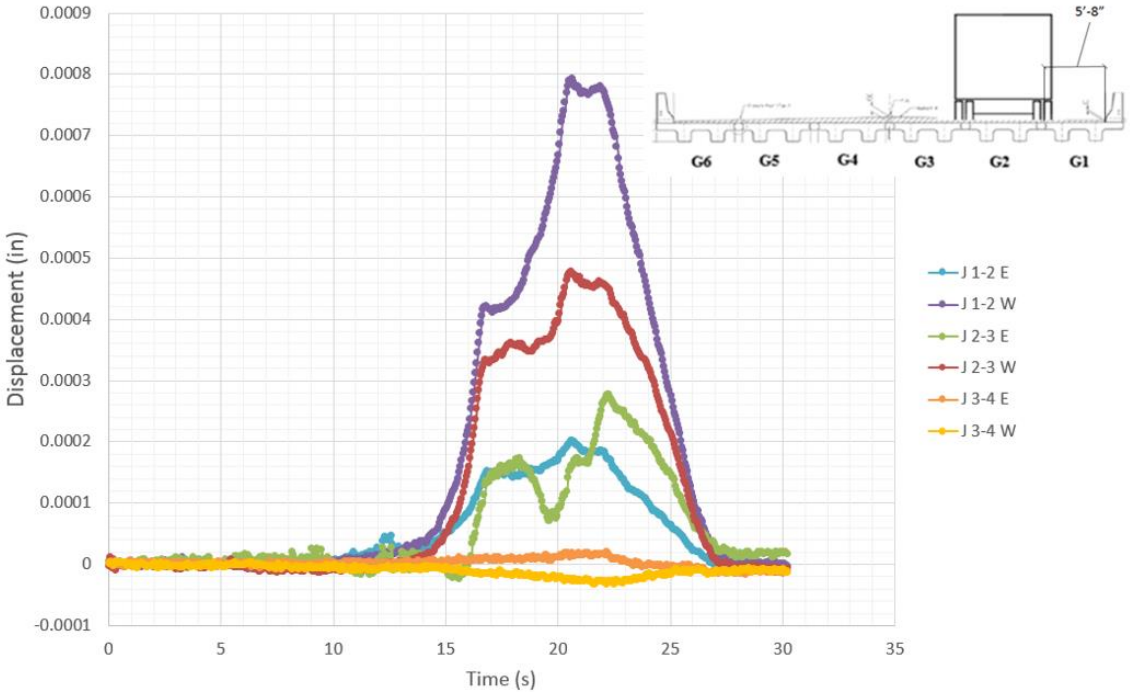

Figure 91: Girder-shear key interface displacements from truck location 1 during LL test 4 load

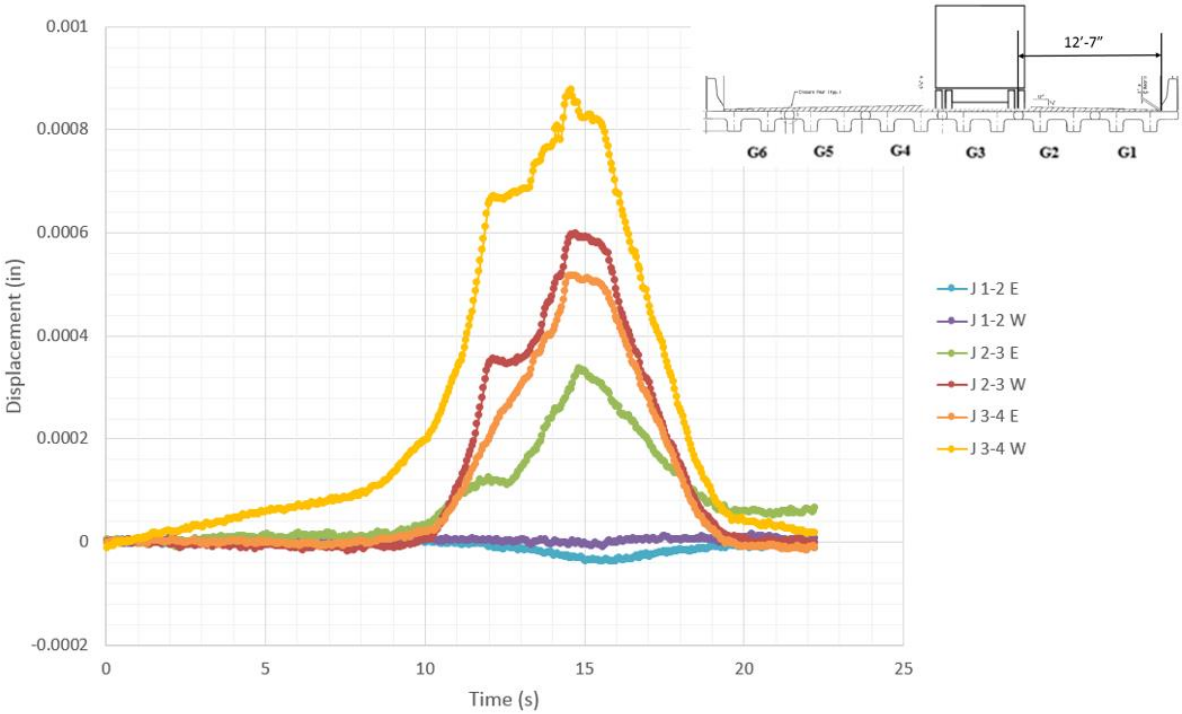

Figure 92: Girder-shear key interface displacements from truck location 2 during LL test 4

The plotted displacement data, of the girder-shear key interfaces at the NEXT-D girder joints, from LL tests 3 and 4 is similar. The “peaks” in the LL test 4 figures are more pronounced than those in the LL test 3 figures because LST data was not collected simultaneously during LL test 4 as it was in LL test 3. In LL test 4 the joint was always either “opening” or “closing” whereas in LL test 3 the joint was in a constant state of remaining “opened” or “closed” while LST data was collected. This is because during LL test 4 the trucks continuously moved at speeds less than 5 mph across the bridge and were never stationary as they were in LL test 3.

A comparison between the maximum, tensile, girder-shear key interface relative horizontal displacements, tested at the NEXT-D girder joints during LL tests 1, 3, and 4, is presented in figure 93. The data from the July test was obtained by Filosa (2017). The comparison indicates that the overall maximum relative horizontal tensile displacement was measured during the LL test 1 at J 1-2.

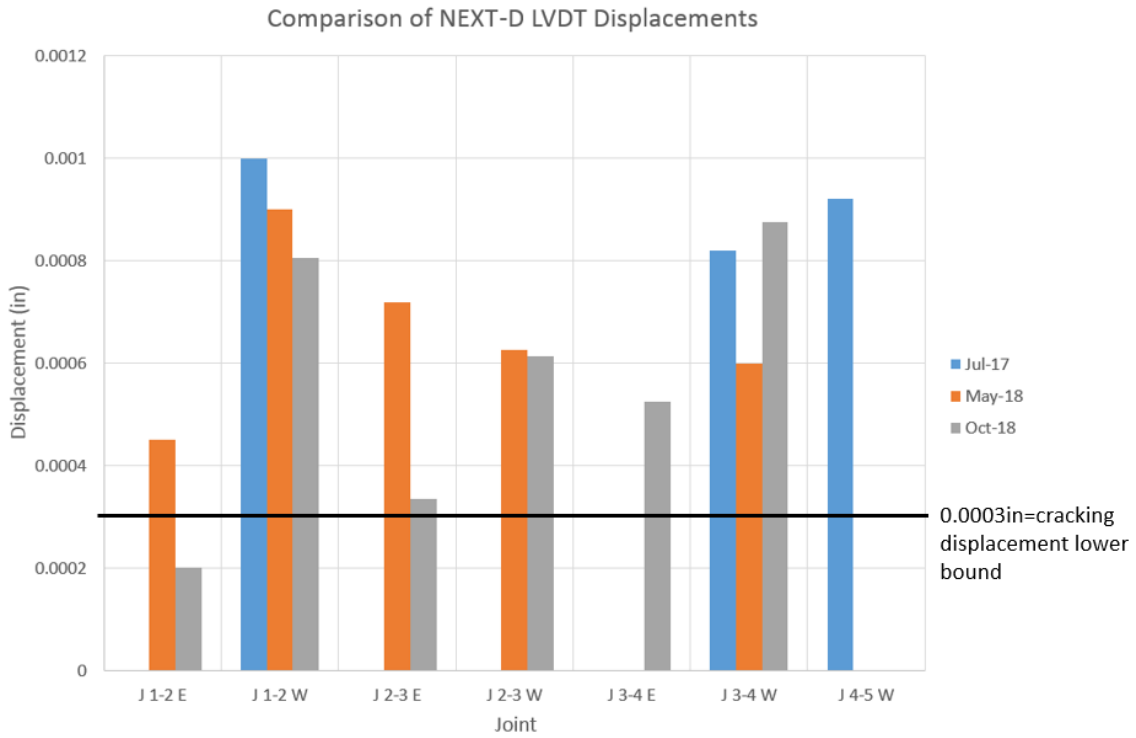

Figure 93: Comparison of maximum relative horizontal displacements during LL tests 1, 3, and 4

The maximum displacements at each joint generally decrease through the progression of the tests. The exception is at joint 3-4W where the displacement during LL test 4 is greater than the displacements measured during LL tests 1 or 3. No significant increase in displacement (an increase by a factor of 4 or greater) in consecutive LL tests is reported at any of the joints instrumented, and all maximum displacements are equal to or less than one thousandth of an inch. Finally, none of the joints displayed displacement behavior significantly greater (factor of 5 or greater) than the other joints.

The black line was determined considering a lower bound of the stress at which the precast-UHPC bond fails and the elastic modulus of the precast girders. From the aforementioned variables, a lower bound "cracking strain" (crack at the bond) was determined using mechanics principles and the corresponding lower bound "cracking

displacement" was calculated considering an estimated gauge length of the LVDTs. The lower bound stress required to cause failure of the precast-UHPC bond (~230 psi) was determined based on multiple experimental results (Filosa, 2017; Halbe, 2014; Joyce, 2014; Sheng, 2013).

Based on the displacement data, the NEXT-D system is performing well. Measured displacements are generally at or above the calculated cracking displacement, however, this displacement is a lower bound. Small cracks at the bond may have formed, but there is no confirmation of cracks developing or existing cracks propagating since the displacement data has only decreased or insignificantly increased over time. Additionally, from visual inspection of the NEXT-D span (see photo survey in the appendix), the research team saw no signs of cracking at the precast-UHPC bond. Thus, the system is assumed to be performing as designed. Regarding the patchwork on the NEXT-D span, the structural behavior at the precast-UHPC joints has not been influenced by the patchwork since no significant changes in the displacement data has occurred.

4.2.2 Solid Span Girder Joint Behavior

Relative horizontal displacements of the girder-girder transverse joints on the solid span were reported to evaluate the health (degradation and cracking) of the solid span girder shear keys. Cracks may have developed at the solid span joints if a particular joint experiences a significantly larger displacement than another joint under the same loading (factor of 4 or greater was considered as significant). Three joints were selected for instrumentation based on the solid span relative horizontal displacement results of LL test 1 and visible reflective cracking on the solid span bridge deck.

Solid span displacement results from LL test 1 are shown in table 14 (Filosa, 017). In table 14, J 13-14 M represents the joint between girder 13 and 14 at mid-span. "N" in table 14 represents the respective joint approximately 5 feet north of mid-span. During LL test 1, on the solid span, the load applied at the joint between girders 13-14 (joint 13-14) from load scenario 1 is approximately the same as the load applied at joint 12-13 from load scenario 3. Considering the displacements differ by at least a factor of 7, researchers instrumented joints 13-14 and 12-13 during LL test 3 to determine if the relative horizontal displacements reported would be similar to those reported in LL test 1. If a significant difference in displacement under the same loading between joints 13-14 and 12-13 were to be reported again, this would indicate that a crack at the joint between girders 13-14 likely has formed. Additionally, joint 10-11 was instrumented for an additional comparison to joint 13-14.

Table 14: LL test 1 horizontal displacement results of the solid span (Filosa, 2017)

		Load Scenario									
		#1	#2	#3	#4	#5	#6	#7	#8	#9	#10
LVDT	J10-11M	-0.00063	0.0023	0.0051	0.00054	0.0017	0.0045	-0.00011	-0.00014	-0.00036	-0.00055
	J11-12M	0.0060	0.0046	0.0027	0.0056	0.0039	0.0018	-0.00015	-0.00016	-0.00042	-0.00055
	J12-13M	0	0.00083	0.0017	0	0.00092	0.0018	0	-0.00001	-0.00005	-5.5E-05
	J12-13N	0	0.00082	0.0015	0	0.00092	0.0017	0	0	-2.3E-05	-3.5E-05
	J13-14M	0.012	0.0086	0.0053	0.012	0.0097	0.0064	-2.3E-05	-0.00003	-0.00048	-0.00055
	J13-14N	0.012	0.0085	0.0053	0.011	0.0095	0.0064	0	0	-0.00038	-0.00039

An example of the strain measured on the solid span during LL test 3 is presented in figure 94. The results shown in figure 94 consider load case 7. The results are sensible since the wheel-line is directly over joint 13-14 and the truck is away from joint 10-11. Joint 12-13 is between the two wheel lines and thus experiences little displacement.

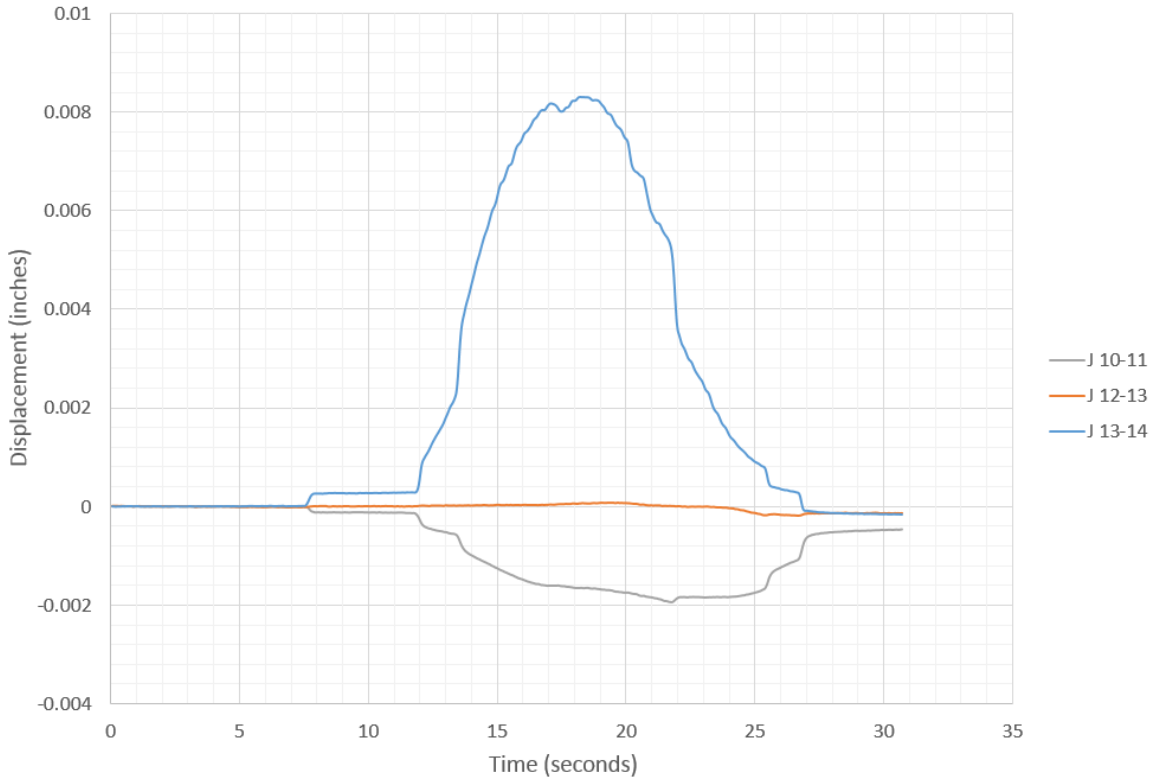

Figure 94: Girder-Girder displacements from load case 7 during LL test 3

Table 15 shows the maximum displacements for each load scenario at each joint during LL test 3. The joint nomenclature is the same as used in table 14, however, all displacements were measured at mid-span and thus an "M" or "N" is not necessary as it was in table 14. From table 15 it is clear that, just as in LL test 1, the reported displacements indicate the solid span continues to experience a significant difference in displacement (factor of ~10) between joint 13-14 and joint 12-13 under similar loading. Since these displacements were calculated to differ by almost a factor of 10 under similar loading, it is assumed that joint 13-14 has undergone some degradation and cracking.

Table 15: Maximum displacements for each load scenario at each joint

LL Test 3 Displacements		
	Load Scenario	
Joint	7	8
J 10-11	0.000049	0.005970
J 12-13	0.000109	0.000841
J 13-14	0.008308	0.001109

During the visual inspection performed in September 2018 (approximately 2 weeks before LL test 4), longitudinal cracking was evident at the approximate location of joint 13-14. Thus the results from LL test 3 were confirmed. It is noted that joint 13-14 recorded displacements that differ by a factor of 1.78 between LL tests 3 and 4. This difference may be due to truck position, longitudinal LVDT location, or some other factor but ultimately is unexplained.

4.3 DFM Test Results

Experimental DFMs were calculated using the strain data collected on the NEXT-D span in May and October of 2018 (LL tests 3 and 4). The strain data collected, the calculation process of the experimental DFMs, and the comparison of the experimental DFMs to AASHTO LRFD design DFMs will be presented in this sub-chapter. Positive strain reported by the strain transducers indicates a tensile strain occurring and negative strain reported by the strain transducers indicates a compressive strain occurring.

4.3.1 Bending Strain Data Results

Strain data was collected considering five different transverse truck locations (load cases 9-13) during LL tests 3 and 4. For each truck location, three different trials were considered to minimize data error. Figure 95 displays the bending strain data collected for load case 9 during LL test 3. The truck location for load case 9 is displayed in the top right corner of the figure. Each curve follows the strain data collected by a specific strain transducer and is denoted with the girder web to which the strain transducer was attached. In the figure's legend, the number represents the girder to which the strain transducer was attached and "E" or "W" display whether the strain transducer was attached to the eastern or western web of its respective girder (north is into the page for the cross section shown in figure 95). Thus, there is one strain transducer attached to each web and two strain transducers attached to each girder since each girder possesses two webs.

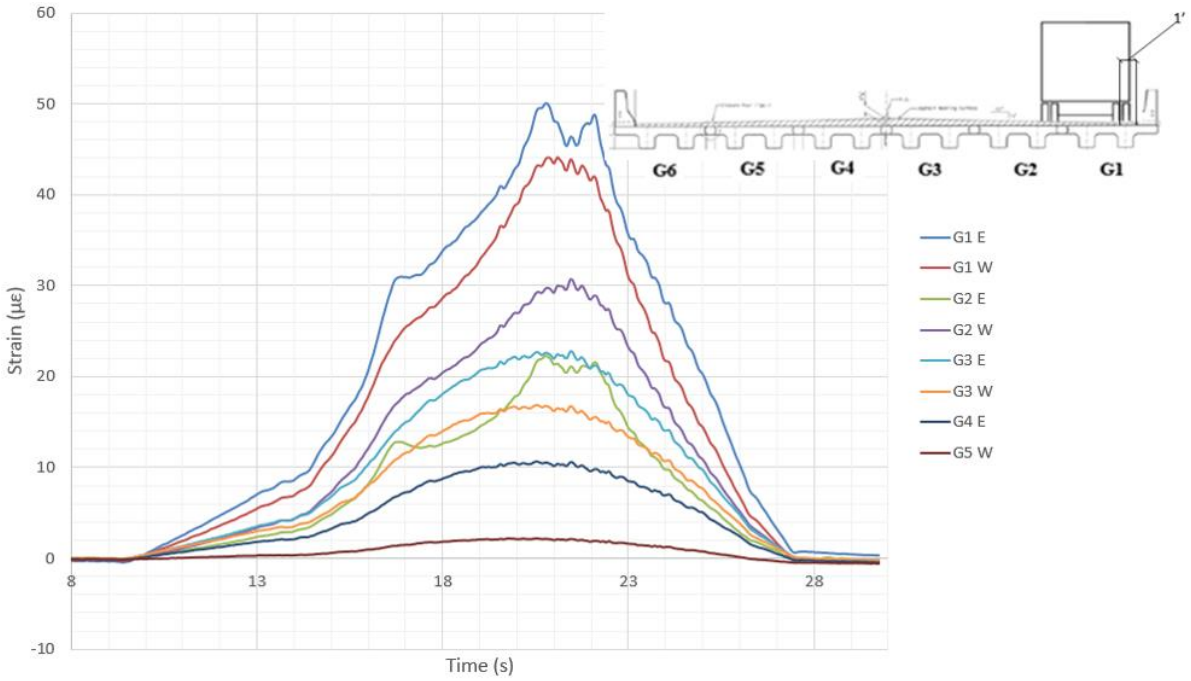

Figure 95: Bending strain collected during LL test 3 considering load case 9

Strain data curve G1E clearly indicates when the front axle and back axles of the truck crossed over the strain transducers. The first leveling of this curve, at approximately 16.5s, is the front axle's crossing mid-span (where the strain transducers were located) and the peaks of the curve is the back axle's crossing mid-span. As expected, the strain transducers located directly beneath the truck crossing measured the largest bending strain and generally as the strain transducers become more distanced from the crossing truck the maximum strain measured decreases. This concept is more clearly shown in figure 96. In this figure, the strain in girder webs 8 and 9 is linearly interpolated since these webs were not instrumented. Additionally, no strain is shown in girder webs 11 and 12. This is because these webs were not instrumented, however very small bending strain was likely experienced by girder webs 11 and 12. Finally, it is noted that the strain recorded by G2 E (shown in figure 95) is not as expected. It is expected that the G2 E

strain data would result in a smoother curve and would be closer to the strain data of G2 W. The unexpected strain data of G2 E is consistent for all truck crossings, but is unexplained.

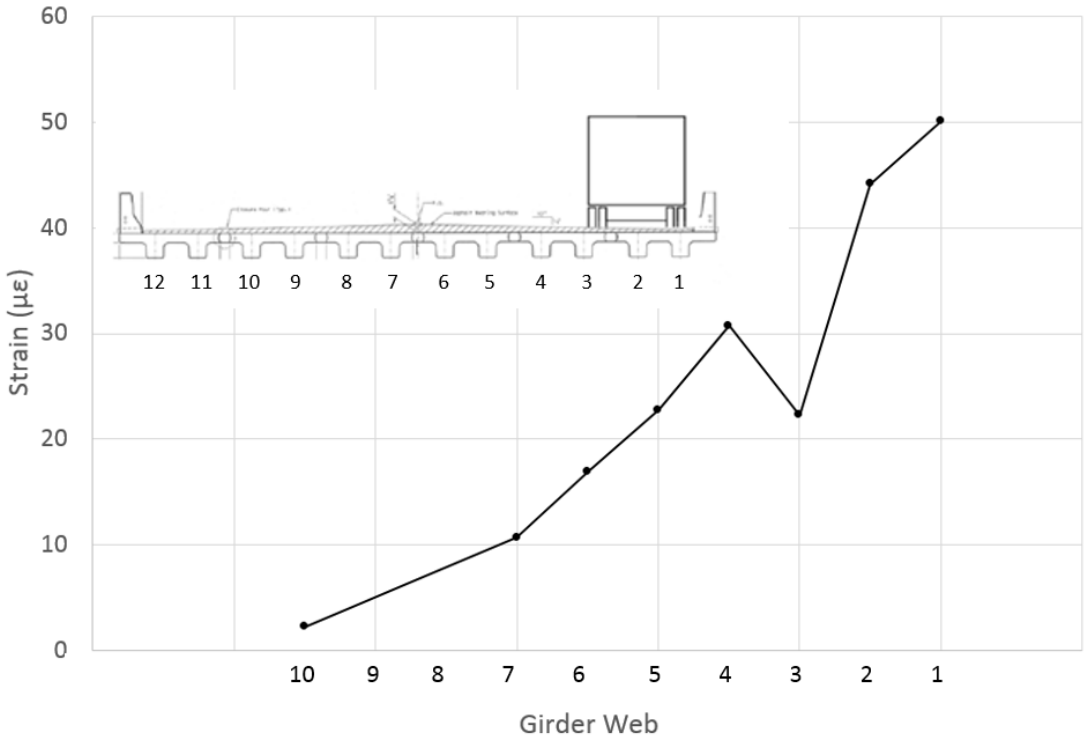

Figure 96: Girder web maximum strains for load case 9 during LL test 3

4.3.2 DFM Calculation Procedure

On the HRB, each NEXT-D girder contains two webs. DFMs for each NEXT-D girder web were calculated using equation 13, outlined in the literature review, and the DFMs of the webs corresponding to each particular girder were summed to calculate a girder DFM for each of the six NEXT-D girders employed on the HRB. On a subject NEXT-D girder, the maximum bending strain measured on one of its webs during LL testing may not occur simultaneously with the maximum bending strain measured on its other web during LL testing, thus both time independent and time dependent calculation

procedures were considered for calculating the girder DFMs of the NEXT-D girders on the HRB.

The time independent and time dependent methods are best outlined considering a subject NEXT-D girder. To exemplify the calculation process for the two methods, consider the subject NEXT-D girder's webs denoted as "a" and "b". For the time independent method, the researchers calculated a girder web DFM for girder web "a", considering the maximum bending strain measured in all of the webs, and then, the same calculation was performed for girder web "b". Finally, the two girder web DFMs were summed to calculate an experimental girder DFM. For the time dependent method, the researchers first calculated a girder web DFM for girder web "a". The maximum strain measured in girder web "a" was used in the numerator of equation 13 and the strain that was measured in all of the other girder webs simultaneously with the maximum strain measurement of girder web "a" was used in the denominator of equation 13. Next, using equation 13 a girder web DFM was calculated for girder web "b". The strain measured in girder web "b" at the time of the maximum strain reading in girder web "a" was used in the numerator of the equation, and the strain measured simultaneously with the maximum strain measurement of girder web "a" in all of the other girder webs, including the maximum strain in girder web "a", was used in the denominator of the equation. The two web DFMs calculated were summed to attain a girder DFM. The time dependent DFM calculation process discussed considered only the maximum strain in girder web "a". A second time dependent DFM considering only the maximum strain in girder web "b" was calculated as well in the same fashion. Thus, for the time dependent method, two DFMs

were calculated. The two calculation methods were considered to evaluate how the calculation process influenced the final experimental DFMs calculated. For every NEXT-D girder on the HRB, the two calculation procedures resulted in essentially the same experimental DFMs. This is clearly evident in table 16 which shows the experimental DFMs calculated from data collected considering truck location 9.

Table 16: Experimental DFMs calculated for truck location 9 strain data

Moment Distribution Factors			
Girder	Time Independent	Time Dependent (a)	Time Dependent (b)
1	0.443	0.443	0.446
2	0.249	0.25	0.246
3	0.186	0.189	0.19
4	0.087	0.089	0.089
5	0.034	0.035	0.035
6	N/A	N/A	N/A

A final discussion regarding the experimental DFM calculation process is necessary regarding the consideration of single lane loading and multi-lane loading. For experimental cases (12 and 13) with two design lanes loaded, the DFMs were calculated using equation 13 and were then doubled. This is because distribution factors are presented in terms of [lanes / girder] in the AASHTO LRFD design code. Using equation four, the DFM calculated is in terms of [lanes / (2 girders)] for cases 12 and 13 since two design lanes are loaded. Thus, the experimental DFM is multiplied by 2 in these cases, so that the experimental DFMs are in terms of [lanes / girder], and may be accurately compared to the design DFMs calculated using the AASHTO LRFD design code.

4.3.3 DFMs Calculated During LL Tests 3 and 4

Five different transverse truck locations and two different calculation procedures were considered in determining experimental DFMs on the NEXT-D span of the HRB.

Thus, many DFMs were calculated, but after a sorting of the DFMs calculated, maximum interior and exterior experimental girder DFMs for single lane loading and double lane loading were established after both LL tests. These DFMs were of importance because they may be directly compared to AASHTO LRFD design DFMs. The experimental DFMs from both LL tests are compared to design DFMs attained considering standard bridge typologies "i" and "k" since these are the two design typologies that best resemble the NEXT-D beam. Also, the experimental DFMs calculated from both LL test data sets are compared to each other and to the experimental DFMs calculated from the LL test data measured in July of 2017 by Filosa (2017) (LL test 1). Figures 97 and 98 present the comparison below.

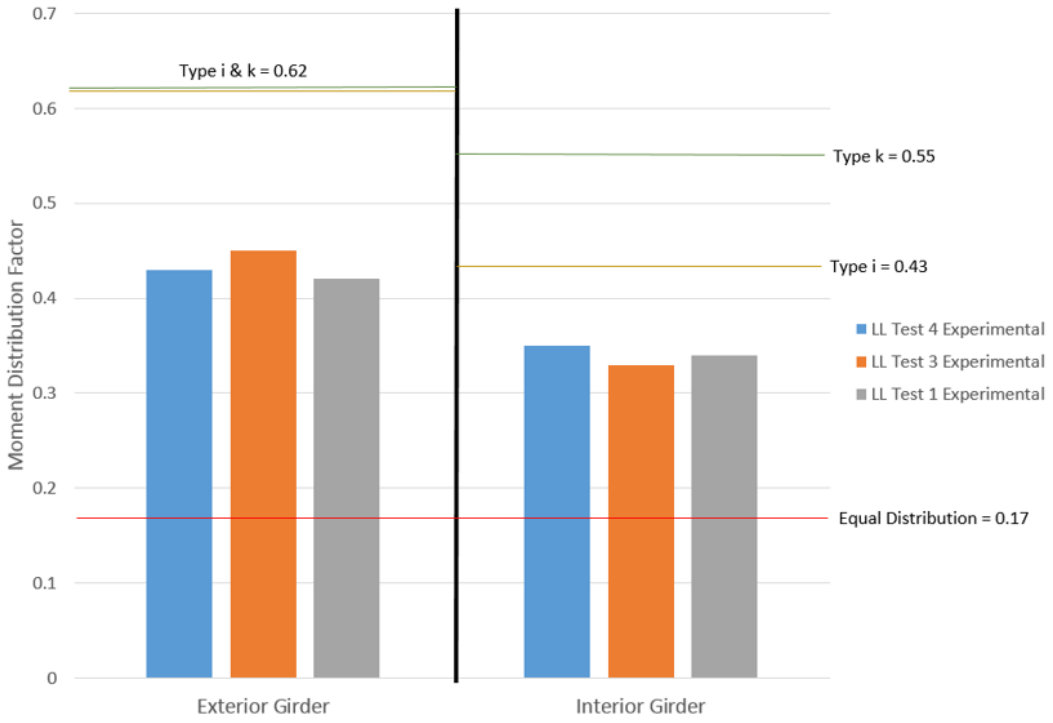

Figure 97: Comparison of single truck experimental DFMs and design DFMs

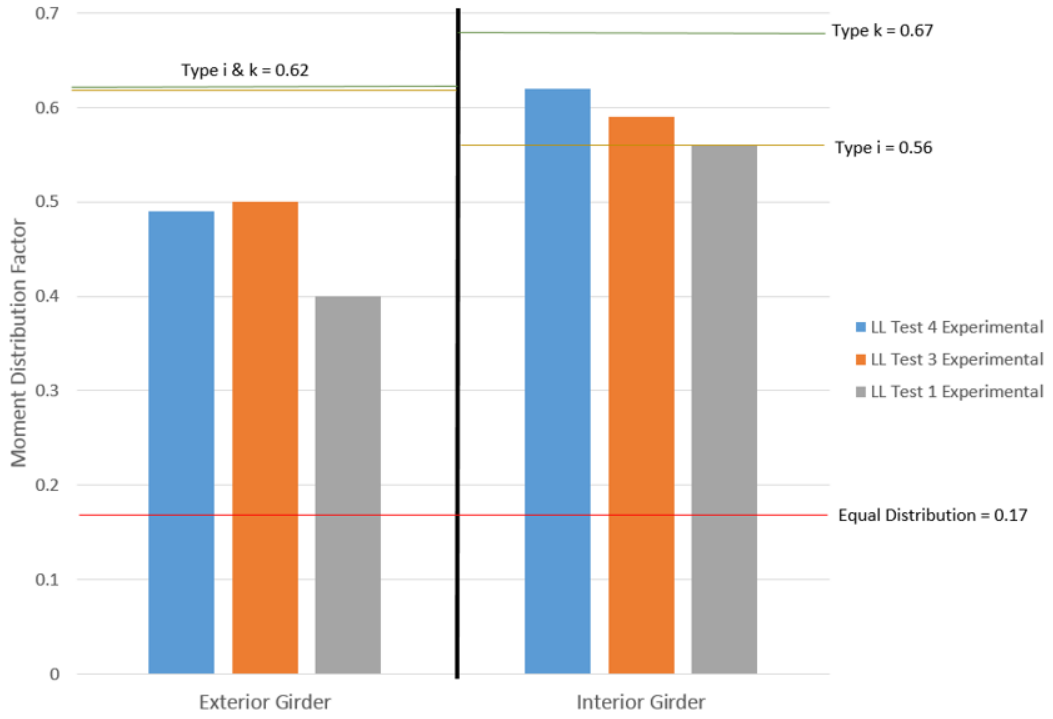

Figure 98: Comparison of double truck experimental DFMs and design DFMs

After the three live load tests, the exterior and interior DFM for the single truck loading experienced little change. The interior DFM for the double truck loading experienced little change as well, however a change occurred in the reported experimental exterior DFM between LL test 1 and LL test 3 (little change occurred between LL tests 3 and 4). The reason for the change in the reported exterior DFM is because opposite transverse sides of the NEXT-D span were tested, considering a double-truck loading, during LL tests 1 and 3. During LL test 1 both sides of the bridge for the single-truck loading were considered and the experimental exterior DFMs reported differed by 0.06 (Filosa, 2017). Thus it is reasonable that for the double truck loading the experimental exterior DFMs differed by 0.1 between LL tests 1 and 3.

The experimental DFMs for the single truck load cases were always less than the AASHTO LRFD DFMs for typologies “i” and “k”. For the double truck load cases, the interior DFM calculated using standard bridge typology “i” was less than or equal to the experimental DFM calculated for this same load scenario and girder location. DFMs calculated using standard bridge typology “k” were always greater than the respective experimental DFMs calculated. Thus, considering the HRB is just a little over one year old and has experienced little degradation, it is prudent to design future NEXT-D bridges similar to the HRB with design DFMs calculated considering standard bridge typology “k”.

4.4 Distribution Factor for Shear Calibration and Torsion Test Results

Shear strain was calculated from the reported strains of strain transducer rosettes instrumented on the NEXT-D span during LL test 3. The purpose was to evaluate the effectiveness of calculating distribution factors for shear (DFV) on the NEXT-D span using the strain data of one diagonally (45°) oriented strain transducer per girder web. The strain transducer rosettes were required to calculate shear strain because the bending (horizontal) and vertical strains of the beam (in addition to the shear strain of the beam) at the location of the rosette effect the strain measured in the diagonal transducer. Using a rosette, the bending, vertical, and diagonal strains are known, thus shear strain may be accurately calculated. It is accepted that a single strain transducer would not report strain reflecting the actual shear strain of a NEXT-D girder web, but the aim was to determine the difference between the strain in a single strain transducer and the shear strain calculated from the strain transducer rosettes. Positive strain in the strain transducers is

representative of tensile strain while negative strain in the strain transducers is representative of compressive strain.

In theory, at the neutral axis of a beam, shear strain is maximized and bending strain is equal to zero. It is difficult to place a strain transducer at the exact location of the NEXT-D girder neutral axis and generally there is some compressive strain present as live load crosses the NEXT-D span, therefore it is very difficult if not impossible to measure the shear strain with a single strain transducer. Thus, rosettes are necessary to determine the actual shear strain of a subject girder. On the NEXT-D span of the HRB, shear strain attained from strain transducer rosettes will be compared to the strain measured in the diagonal strain transducer of the rosettes. If the difference is negligible, it may be plausible to use a single diagonal strain transducer to measure shear strain for calculating DFVs. Equations 16 to 18 (strain transformation equations for rosettes) outline how shear strain may be calculated from rosette strains. Figure 99 presents a rectangular rosette. If ε_a and ε_c in figure 99 are very small, then the difference between the actual shear strain in the girder, and the strain measured by the diagonal strain transducer will be negligible. ε_a is at 0 degrees in figure 99 which is in the direction of horizontal strain (ε_{xx}).

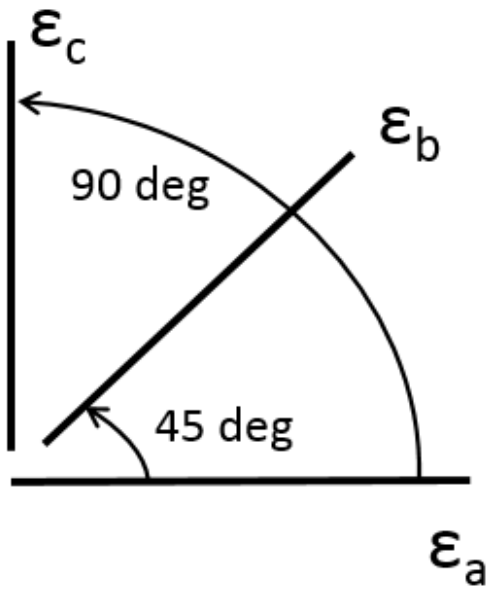

Figure 99: Orientation of strain transducers in a rectangular rosette (Boresi, 2003)

$$\varepsilon_a = \varepsilon_{xx}\cos^2(\theta_a) + \varepsilon_{yy}\cos^2(\theta_a) + 2\varepsilon_{xy}\cos^2(\theta_a) \quad \textbf{Equation 16}$$

$$\varepsilon_b = \varepsilon_{xx}\cos^2(\theta_b) + \varepsilon_{yy}\cos^2(\theta_b) + 2\varepsilon_{xy}\cos^2(\theta_b) \quad \textbf{Equation 17}$$

$$\varepsilon_c = \varepsilon_{xx}\cos^2(\theta_c) + \varepsilon_{yy}\cos^2(\theta_c) + 2\varepsilon_{xy}\cos^2(\theta_c) \quad \textbf{Equation 18}$$

Considering the angle from the horizontal to ε_a (θ_a), ε_b (θ_b), and ε_c (θ_c) of a rectangular rosette (0°, 45°, and 90° respectively), the horizontal (ε_{xx}), vertical (ε_{yy}), and shear (ε_{xy}) strain of the girder at the location of the rosette may be calculated using equations 19 to 21.

$$\varepsilon_{xx} = \varepsilon_a \quad \textbf{Equation 19}$$

$$\varepsilon_{yy} = \varepsilon_b \quad \textbf{Equation 20}$$

$$\varepsilon_{xy} = \varepsilon_b - 0.5*(\varepsilon_a + \varepsilon_c) \qquad \textbf{Equation 21}$$

4.4.1 Strain Data Collected on the NEXT-D Span

Shear strain data was collected during the May 2018 LL test (LL test 2) by three strain transducer rosettes on girders 1, 2, and 3 (one rosette per girder). Shear strain data collected for only single truck locations (locations 9, 10, and 11 shown in figure 73) is considered for this analysis. The shear strain data resulting from truck locations 9 to 11 is shown in figure 100.

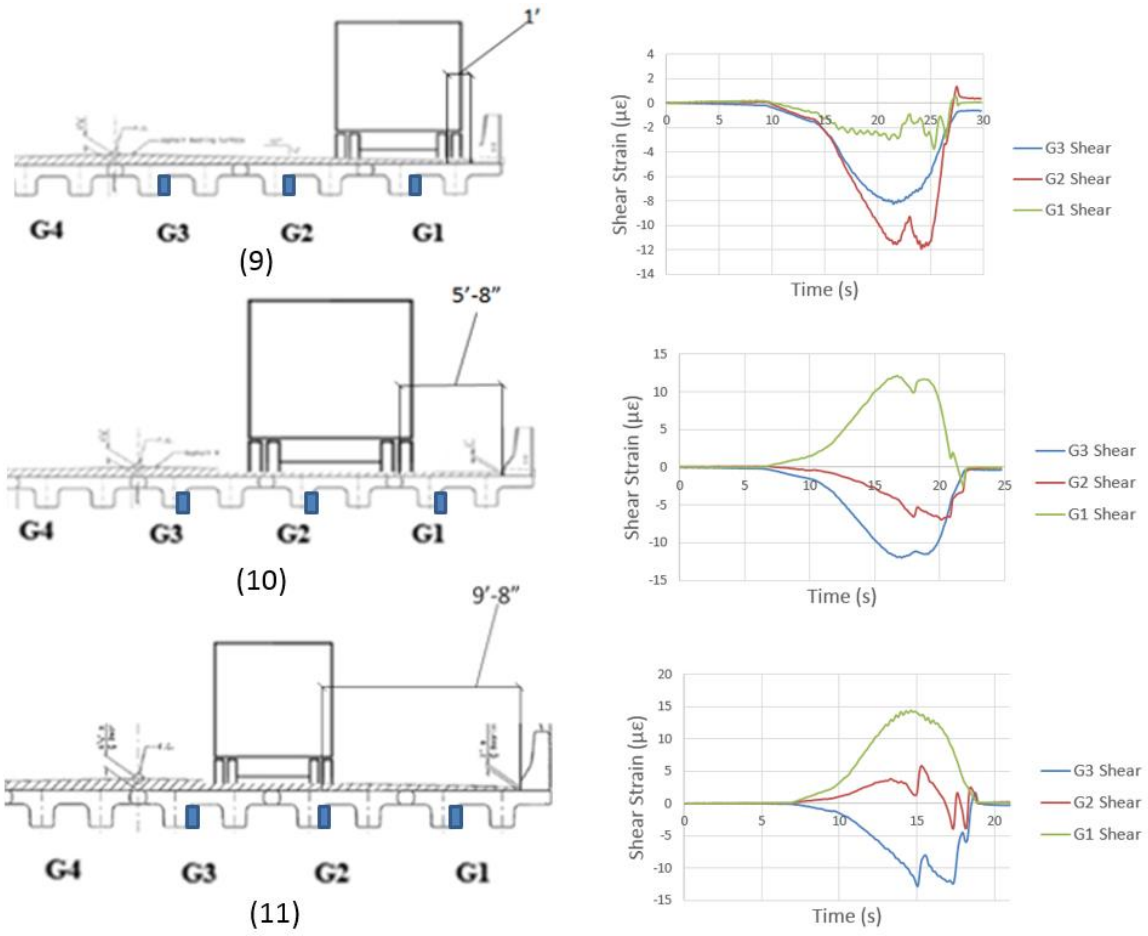

Figure 100: Calculated LL shear strain data for truck locations 9 to 11

The shear strain data peaks are during the time range when the trucks are passing directly over the rosettes. For truck location 9, this is approximately between 18 and 25s. The data indicates that the shear force generated by the LL was transferred transversely and shared amongst the NEXT-D girders. It is expected that the shear strain would be negative since the diagonal strain transducers were oriented parallel to the principle compressive stress. However, reported positive shear strain provides evidence for other factors influencing the strain data. Therefore, the shear strain data is difficult to fully interpret and it is difficult for the researchers to confidently evaluate how the shear force distributes transversely. It is likely that torsion is an influential additional factor effecting the shear strain data measured other than the shear force itself. Another factor that may be influencing the shear strain data of the exterior girders is the barrier rails, which stiffens the bridge and may carry some of the shear force applied by the LL. However, barrier rails only carried at the most 19% of exterior girder shear forces in previous analyses (Dymond, 2015).

4.4.2 Discussion of Shear Strain Data

For truck location 9, the shear strain measured in girder one is significantly less than the shear strain measured in the other girders, which is not as expected considering the truck location. Also, the girder one maximum shear strains measured for truck locations 10 and 11 are positive and the girder two maximum shear strain measured for truck location 11 is positive which is not expected due to the orientation of the diagonal strain transducers. Because of the transverse locations of the trucks corresponding to the shear strain data considered, it is hypothesized that an eastward twisting may cause

torsional girder strains that add to the shear strain due to the vertical shear force resultant, leading to increased negative shear strain calculated from the reported rosette strains. Conversely, a westward twisting may cause torsional girder strains that subtract from the shear strain due to the vertical shear force resultant, leading to positive shear strain calculated from the reported rosette strains. This is exemplified considering the shear strain calculated from the rosette strains recorded on girder two. In figure 100, the girder 2 calculated shear strain becomes less and less negative as the truck location moves west transversely on the bridge deck. In truck location 9, the truck is east of the girder 2 instrumented web and in truck location 11, the truck is mostly west of the girder 2 instrumented web.

Torsion strains on bridge girder webs add to shear strain on one side of a girder web and oppose shear strain on the other side of a girder web. To exemplify this effect consider two strain rosettes positioned on either side of a girder web. If torsion was influencing the shear strain measurements, the rosettes would measure strains leading to a calculation of different shear strains. The average calculated shear strain from the rosettes would theoretically be the actual shear strain due to the vertical shear force resultant in the girder. Thus, to accurately measure shear strain due to only the vertical shear force resultant, rosettes may be needed on either side of a subject girder web.

4.4.3 Evaluation of Distribution Factor for Shear Method Analyzed

The purpose of the shear LL test (during LL test 3) was to determine if using one diagonally oriented (45°) strain transducer per girder web on the NEXT-D span of the HRB would result in shear strain measurements accurate enough to calculate reasonable

DFVs. A comparison of the absolute maximum (maximum magnitude regardless of sign) shear strain measured to the absolute maximum strains measured by the diagonal strain transducer rosettes is shown in tables 17 to 19 for each girder.

Table 17: Shear strain comparison for truck location 9

Truck Location 9 Strain Measurements			
Girder	Shear strain	Diagonal Strain	Percent Difference
1	-3.9	-2.3	42%
2	-11.8	-9.7	18%
3	-8.0	-9.0	12%

Table 18: Shear strain comparison for truck location 10

Truck Location 10 Strain Measurements			
Girder	Shear strain	Diagonal Strain	Percent Difference
1	12.1	13.2	9%
2	-6.6	-5.0	24%
3	-12.1	-13.3	10%

Table 19: Shear strain comparison for truck location 11

Truck Location 11 Strain Measurements			
Girder	Shear strain	Diagonal Strain	Percent Difference
1	14.3	15.0	5%
2	-5.8	-2.2	42%
3	-12.9	-13.0	1%

The shear strain compared relatively well with the diagonal strains measured, however, three cases differed by more than 20% and two cases resulted in a significant difference (42%). Thus, in the majority of the scenarios bending and compressive strains

are not strongly influencing the shear strain measured, however, the three cases with significant differences will cause different DFVs to be calculated considering the two methods (strain transducer rosette and single diagonal strain transducer).

The shear strain in each girder based on the truck locations was not always as expected. Considering truck location nine, the shear strain experienced by girder one should be greater than the shear strain experienced by girder three. For truck location 11, the shear strain experienced by girder two should be closer to the shear strain experienced by girder three. Finally, positive shear strains were not expected to be measured, therefore there is not confidence in the strain data for calculating accurate distribution factors for shear.

Considering tables 17 to 19, the significant percent differences between diagonal strain and shear strain and the sign change in the diagonal strain recorded and calculated shear strain is best hypothesized to be due to torsion. Additionally, torsion effects would reasonably explain the positive diagonal strain and unexpected shear strain in each girder. Because torsion, in addition to the vertical shear force resultant, influences the strain measurements on the NEXT-D girders of the HRB, the researchers decided that DFVs are unable to be calculated accurately with the equipment available (i.e. one strain transducer per girder web). However, a torsion test is performed with the available equipment to evaluate the hypothesis that torsion is strongly influencing the strain measured by the diagonal strain transducers in the rosettes.

4.4.4 Torsion Test Results and Evaluation of Measuring DFVs

The rosette strain data from LL test 3 indicated that torsion significantly influenced the strain reported form the diagonal strain transducers. A torsion test was performed during LL test 4 to evaluate the effect of torsion on the strain reported by the diagonally oriented strain transducers. In order to determine the strain due to the torsion experienced by a subject NEXT-D girder web, rosette strain data must be collected on each transverse side the subject girder web. Using the strain transformation equations (equations 16 to 18), the torsional strain and the shear strain can be calculated for each side of the subject girder web. Torsional strain adds to the strain calculated from the strain transformation equations on one side of a girder web and subtracts from the strain calculated from the strain transformation equations on the other side of a girder web. The average of the total strain calculated (sum of the torsional and shear strain) for each side of the girder web is equal to the shear strain. Half of the difference between the total strains calculated for each side of the subject girder web is equal to the torsional strain.

The results of the torsion test are shown in figures 102 to 106. In each figure, the calculated rosette shear strain for the eastern and western rosettes instrumented on girder 3 are shown. Additionally, the shear strain, and the torsion strain for girder 3 is shown in each figure. In figures 102 to 106, the rosette shear strains are calculated using equation 21, the shear strains are calculated as the average of the calculated rosette shear strains, and the torsion strain is calculated as the difference between the shear strain and the eastern calculated rosette shear strain. Figure 101 defines the strains necessary to calculate the rosette shear strain by considering the strains measured from truck location

six. In figure 101, strains necessary to calculate the rosette shear strain (6.07με) using equation 21 are ε_a= 5.68με, ε_b= -3.53με, and ε_c= -0.61με. The rosette shear strains are generally not equal to the maximum shear strain present but the difference between the rosette shear strain and maximum shear strain is negligible (<1με).

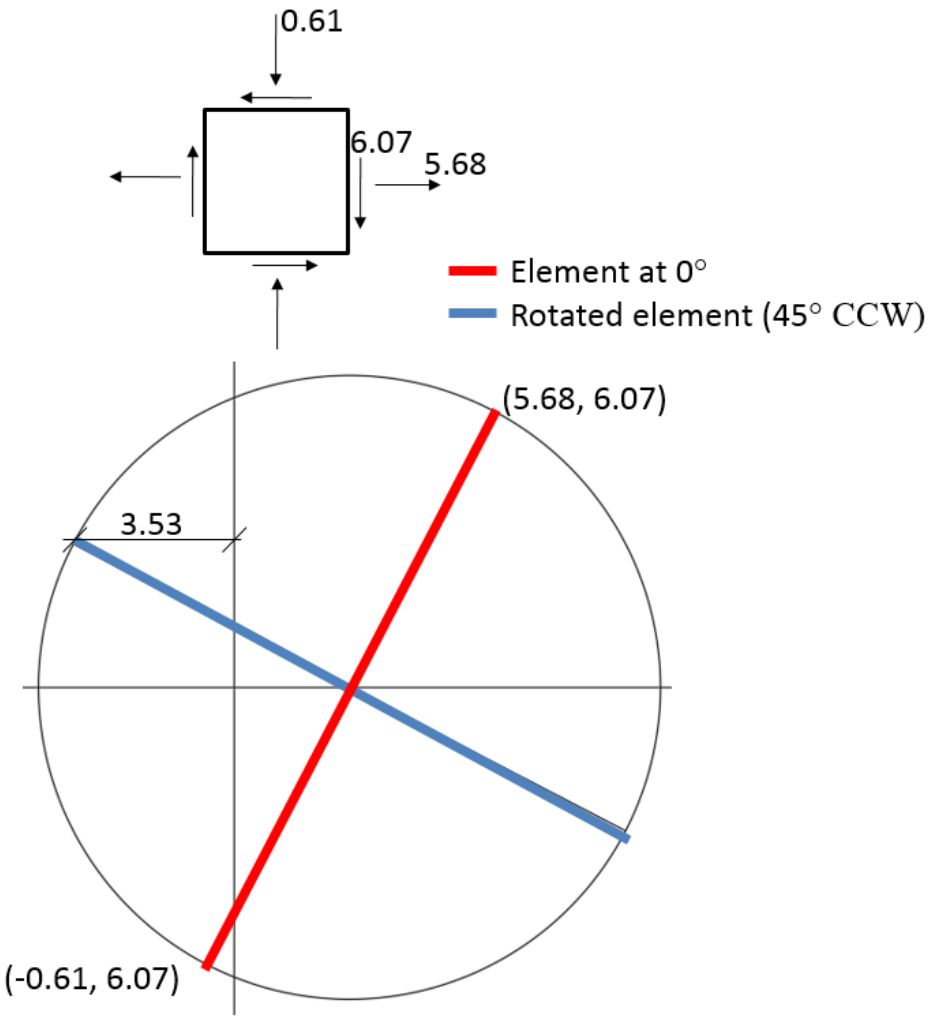

Figure 101: Strain element and Mohr's circle of strain for truck location 16

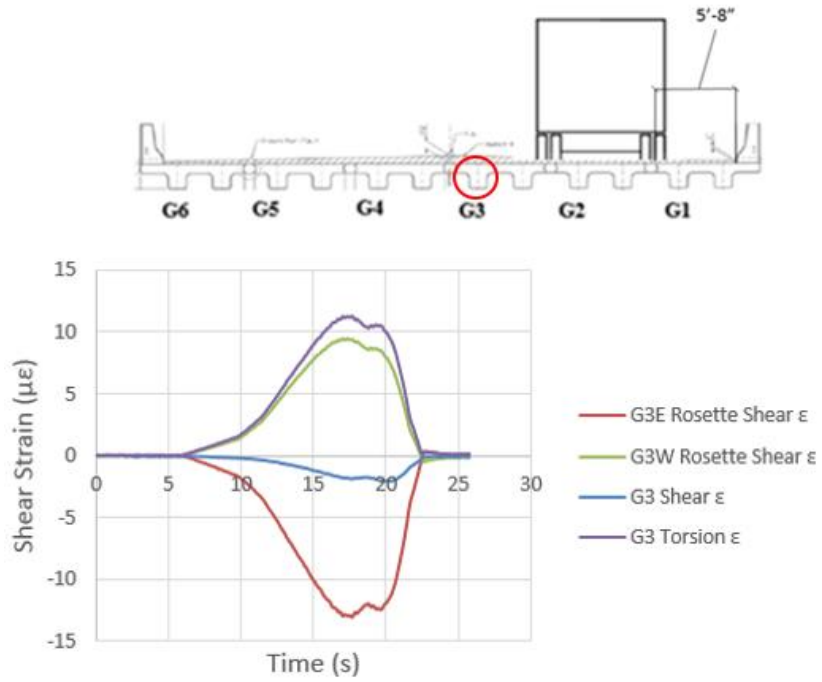

Figure 102: Strain calculated during the torsion test for truck location 14

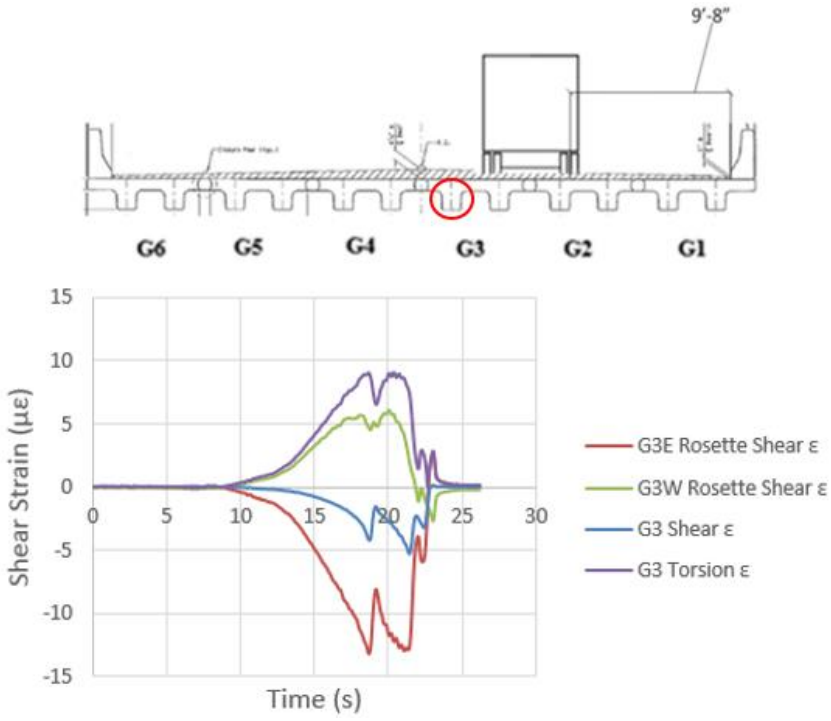

Figure 103: Strain calculated during the torsion test for truck location 15

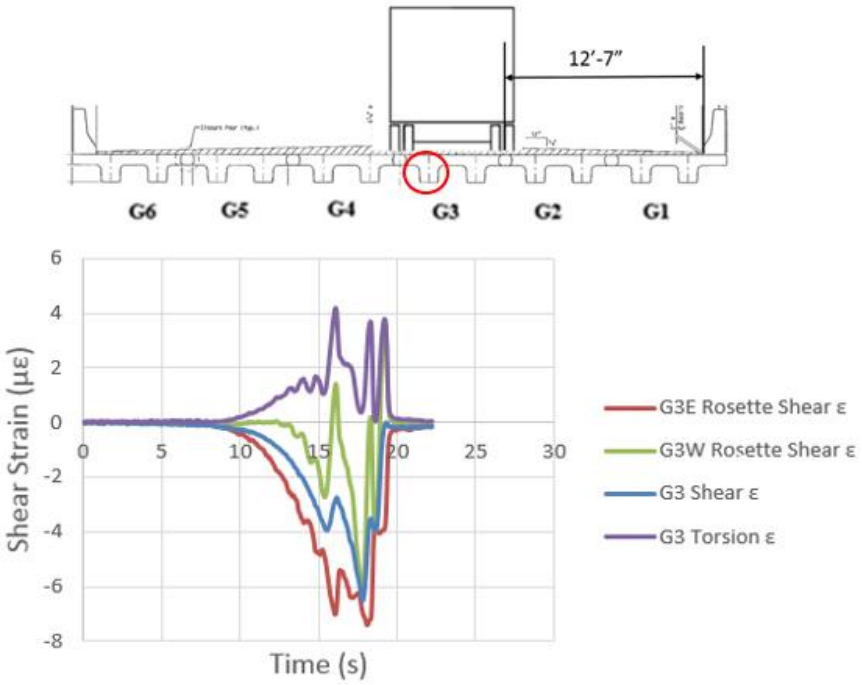

Figure 104: Strain calculated during the torsion test for truck location 16

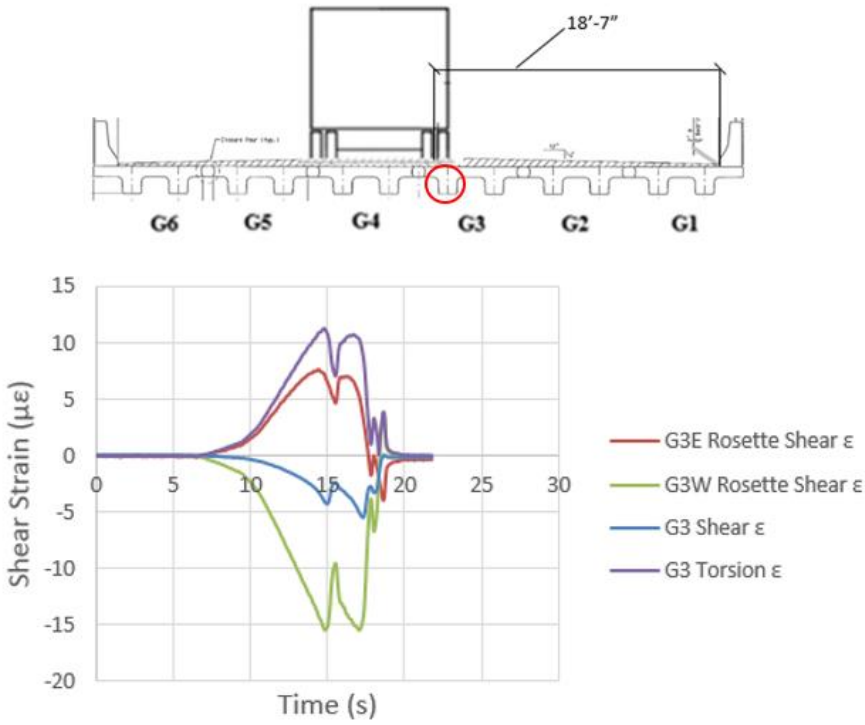

Figure 105: Strain calculated during the torsion test for truck location 17

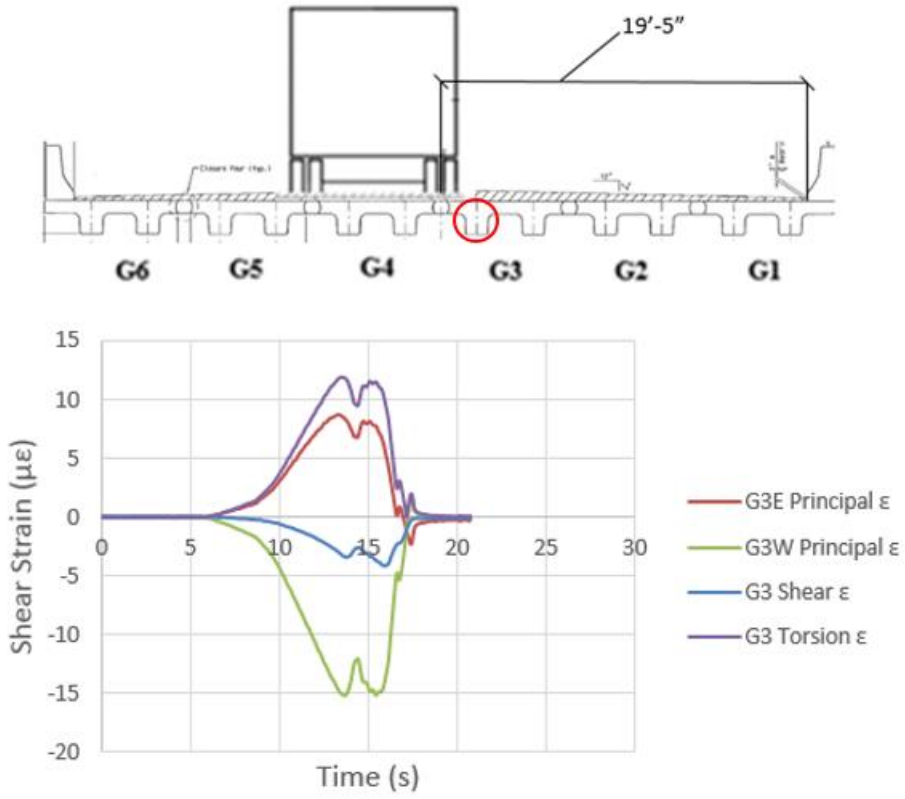

Figure 106: Strain calculated during the torsion test for truck location 18

Considering figures 102 to 106, the shear strain calculated for every truck location is negative. This is expected since the strain transducers were oriented parallel to the principle compressive stress. Additionally, it is clear that torsion is significantly influencing the calculation of the shear strain from each rosette. When the truck is away from the instrumented web (i.e. truck locations 14, 15, 17, and 18) torsional strains are greater than shear strains. Conversely, when the truck is straddling the instrumented web (i.e. truck location 16), shear strain is greater than torsional strain. Significant torsion also causes the total strain calculated from each rosette to change sign depending on which side of the instrumented web the truck is located. Finally, the shear strain calculated is greatest when the truck is closest (i.e. truck location 16) to the instrumented web.

Considering the evaluation, because torsion has a large effect on the strain calculated considering the strain transducer rosettes, it would be necessary to instrument each side of each girder web to accurately calculate distribution factors for shear.

Chapter 5: Conclusions and Recommendations

The conclusions of this thesis are split into three parts. The first part considers the transverse durability of the shear keys on the solid and NEXT-D spans and considers the effectiveness of the Life Span Technology (LST) sensors to monitor these shear keys. The second part considers the experimental distribution factors for moment (DFM) determined on the solid and NEXT-D spans and how they compare to the theoretical DFMs outlined in AASTHO LRFD. The third part considers the effectiveness of measuring DFVs using just one strain transducer per web and considers the results of the torsion test.

Recommendations are presented in the final subchapter.

5.1 LST and Transverse Durability Conclusions

Conclusions regarding the LST sensor data in general, and from the LL tests and temperature correlation analysis are presented below. Sensors from all of the spans were tested via LL in January of 2018. Only the sensors on the NEXT-D span were tested via LL in May of 2018.

- Several anomalies were observed in the general LST strain data.
- The sudden changes in strain in the LST data did not correlate with any of the known major events.
- In LL test 2, sensors LST-01 and LST-09 did not report a change in strain due to truck loading. Additionally LST-03 reported a negligible change in strain.
- In LL test 2, the responsive sensors on the solid and voided spans recorded maximum changes in strain of 853με (0.0047in) and 442με (0.0024in)

respectively. The responsive sensors on the NEXT-D span only recorded a maximum change in strain of 101με (0.0006in). LL did not fully account for the transverse shear key strain on any of the spans.

- During LL test 3, LST data differed from the LVDT data. Additionally, some of the LST data provided a negligible response to LL. Therefore, the LST sensors are not effective for short-term LL testing and are difficult to calibrate for LL.
- Inverse correlations were observed between temperature and strain for the sensors on the NEXT-D span. Correlation coefficients between temperature and active strain ranged from -0.55 to -0.90. Correlation coefficients between temperature and peak strain for three of the four sensors ranged from -0.82 to -0.96. These results suggested that temperature is a significant contributor to the LST-reported strain readings on the NEXT-D span, however, relatively exact estimates of thermal strain could not be measured.
- General conclusions regarding the HRB health cannot be made solely on the basis of the LST-reported strain data due to its data anomalies, ineffectiveness in short term LL testing, and other loads' unknown level of influence on the strain readings.

Conclusions regarding the transverse durability of the NEXT-D and solid spans are presented below.

- NEXT-D Span: The transverse displacement responses to load during LL tests 1, 2, and 3 are very similar. In all tests the girders experienced very little residual relative horizontal displacement and the displacement data displayed clearly when

the trucks' front and back axles passed over the LVDTs. Also, in both tests LVDTs away from the applied load displayed compressive displacements.

- NEXT-D Span: Maximum measured displacements in all tests are generally at or above the cracking displacement. Significant cracking does not appear to be occurring since the maximum relative horizontal displacements measured generally decrease through the progression of the LL tests and the maximum relative horizontal displacements of each joint interface measured do not differ by a significant factor (factor of 4). Additionally, no reflective cracking was observed on the NEXT-D span. Thus, it is believed that little deterioration has occurred in the NEXT-D shear keys on the HRB.
- Solid Span: Joint 13-14 recorded the largest relative horizontal displacements (0.012in and 0.008in during LL tests 1 and 3 respectively) on the solid span during both tests. This joint continues to record displacements greater than joint 12-13 by a significant factor under similar loading conditions. During the July test this factor was 7 and during the May test this factor was 10. Since the factor is significant (>4) and has increased, it is believed that this joint is experiencing cracking or delamination. Reflective cracking observed during visual inspection confirmed this assumption.
- Solid Span: The remainder of the joints experience relative horizontal displacements no greater than 0.006 in. The small displacements and relatively similar magnitudes of displacement under similar loading indicate that there is likely no cracking or delamination occurring at any of the remaining joints.

5.2 DFM Conclusions

The following conclusions regard the experimental and theoretical DFMs determined on the NEXT-D span. These conclusions are based on the results of LL tests 3 and 4 and reference the results from LL test 1.

- Experimental DFMs from LL tests 1, 3, and 4 compare within a magnitude of 0.06 in all design cases excluding the side-by-side truck exterior case. No DFMs changed by more than 0.03 in consecutive LL tests.
- In the design case where the experimental DFM values do not compare as reasonably, the difference may be attributed to testing the eastern side of the HRB, which has previously produced larger experimental DFMs than the western side of the bridge. The small differences in magnitude of the experimental DFMs between the two LL tests indicate that the bridge has not changed its behavior in dispersing LL transversely.
- Both the "k" and "i" section typologies produce code-calculated DFMs greater than the experimental DFMs determined during LL tests 1, 3, and 4 except in one design case. For the interior girder side-by-side truck design case, the theoretical DFM determined from section type "i" is equal to the experimental DFM determined during LL test 1 and less than the experimental DFMs determined in LL tests 3 and 4. Thus, section typology "i" is not conservative for the design of NEXT-D beams and section typology "k" is conservative for the design of NEXT-D spans similar to that employed on the HRB.

5.3 Calibration of DFVs Testing Method and Torsion Test Conclusions

The following conclusions regard the experimental shear strain data measured on the NEXT-D span. These conclusions are based on the results of LL tests 3 and 4. The conclusions from live load test 3 are as follows:

- The shear strain in girder one was primarily positive for two of the three transverse truck load locations and the shear strain in girder two was primarily positive for one of the three transverse truck load locations. Positive strain is not expected since the strain transducers were oriented parallel to the principle compressive stress.
- Significant percent differences between the diagonal transducer strains recorded and shear strains calculated were observed. Sign changes were observed in the diagonal transducer strains recorded and shear strains calculated. Thus, it is very difficult to accurately determine shear distribution factors considering only one diagonal strain transducer per girder web.
- Because both positive and negative strain of similar magnitude was measured by the diagonal transducers, it is assumed that torsion is influencing the strain readings of the diagonally oriented strain transducers.

The conclusions from live load test 4 are as follows:

- The shear strain from the shear force was observed to always be negative, which is expected since the diagonal strain transducers were oriented parallel to the compressive stress.

- Calculated rosette shear strains were observed to exhibit opposite signs (+/-) for all truck locations excluding truck location 16.
- The G3E calculated rosette shear strains were observed to be negative for truck locations 14 and 15 and positive for truck locations 17 and 18. The G3W rosette shear strains exhibited the opposite behavior.
- The calculated shear strain due to torsion was observed to be greater than the calculated shear strain due to the shear force for all truck locations excluding truck location 16.
- Based on the above observations, it is concluded that torsion significantly influences the calculated rosette shear strain. Thus, it is necessary to instrument a strain transducer on either side of each girder web to accurately calculate DFVs.

5.4 Recommendations

Considering the above conclusions, recommendations resulting from the research for the purpose of this thesis are as follows:

- LST should be used in conjunction with other instrumentation to measure strain and evaluate bridge health.
- SCDOT should consider NEXT-D girders for future short to medium span flat slab girder bridges. There was no visible sign of significant cracking at any of the shear keys on the NEXT-D span however the solid span exhibited signs of significant cracking at one of its shear keys.

- When designing NEXT-D spans similar to that utilized on the HRB, AASHTO LRFD typology “k” should be considered for calculating moment distribution factors.
- Longer span lengths (>40 feet) should be tested to evaluate the use of NEXT-D girders for medium to long spans.
- The NEXT-D UHPC shear keys are assumed to have undergone little deterioration since the girder relative horizontal displacements and DFMs did not significantly change over one and a half years. Additionally there were no visual signs of joint deterioration on the NEXT-D span. Thus, UHPC is recommended to be used as the shear key fill for future NEXT-D spans.
- Single diagonal strain transducers do not always measure strains approximately equal to the shear strain present. It is recommended that a rosette be used to calculate shear strain for determining DFVs.
- Under LL, significant torsion strain relative to the shear force strain was present in the NEXT-D girders on the HRB. Therefore, to measure accurate DFVs, it is recommended that a rosette be instrumented on either side of each subject girder web to calculate the shear strain in each subject girder web.

APPENDICES

Appendix A

Calculation of AASTHO LRFD Moment Distribution Factors

Moment distribution factors (DFM) were calculated using the AASTO LRFD design code for the NEXT-D span. These code-calculated DFMs were calculated considering AASTHO section typologies "i" and "k" since PCI recommends these section typologies be considered for NEXT-D girder design. The NEXT-D code calculated DFMs are compared to the experimental DFMs to evaluate the PCI recommended AASHTO section typologies. DFMs were calculated for interior and exterior girders for one design lane loaded and two design lanes loaded.

A.1 Hanging Rock Creek Bridge NEXT-D Span

The NEXT-D span on the Hanging Rock Creek Bridge (HRB) spans 40 feet and the girders have an average spacing of 6.8 feet. Figure 107 below shows the geometry of the interior and exterior NEXT-D girders. Considering the geometry of the NEXT-D girders, their span, and their average spacing, DFMs were calculated using AASHTO LRFD.

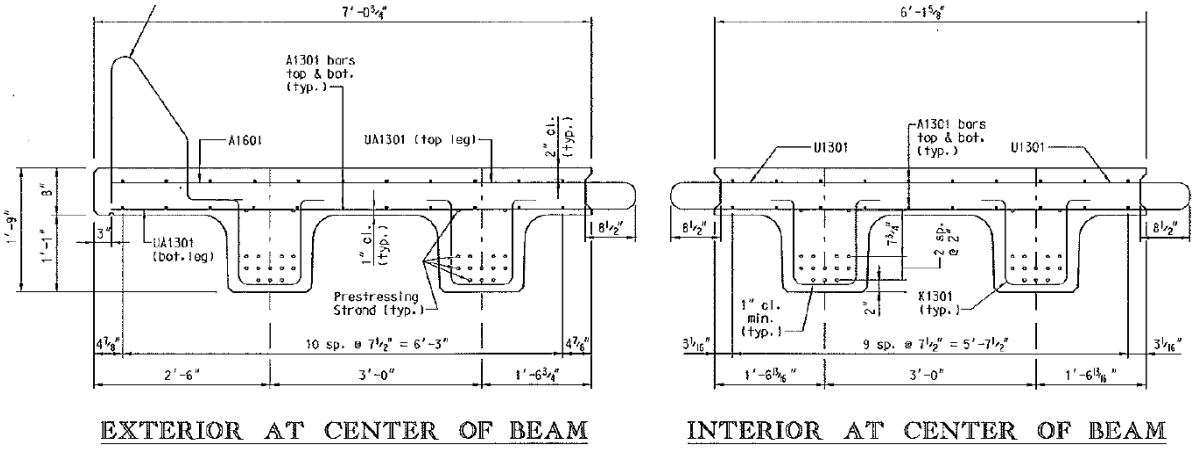

Figure 107: NEXT-D girder cross sections

A.2 Section Typology "i" and "k" Code-Evaluated DFM Calculation Process

The calculation process for determining interior DFMs considering section typologies "i" and "k" are shown below (NEXT-D interior DFMs). For section typology "k", a single stem is considered and the average stem spacing (center of stem to center of stem) is considered in the typology "k" equation to calculate DFMs. The calculated DFM is then doubled. For section typology "i", both stems are considered and the average girder spacing (center of girder to center of girder) is considered in the typology "i" equation to calculate DFMs. The equations for calculating DFMs considering section typologies "i" and "k" are outlined in the literature review.

Interior Girders

type "k"

$b_{stem} := 14in \quad h_{stem} := 13in \quad A_{bs} := b_{stem} \cdot h_{stem} = 182 \cdot in^2$

$I_{bs} := \frac{b_{stem} \cdot h_{stem}^3}{12} = 2563.167 \cdot in^4 \quad \eta := 1 \quad e_g := 10.5in$

$K_g := \eta \cdot \left(I_{bs} + A_{bs} \cdot e_g^2 \right) = 22628.667 \cdot in^4 \quad S := 3.4 \quad L := 40 \quad t_s := 8$

$K_g := 22630$

$$InteriorDFM_1 := 2 \cdot \left[0.06 + \left(\frac{S}{14} \right)^{0.4} \cdot \left(\frac{S}{L} \right)^{0.3} \cdot \left(\frac{K_g}{12 \cdot L \cdot t_s^3} \right)^{0.1} \right] = 0.547$$

$$InteriorDFM_2 := 2 \cdot \left[0.075 + \left(\frac{S}{9.5} \right)^{0.6} \cdot \left(\frac{S}{L} \right)^{0.2} \cdot \left[\frac{K_g}{\left(12 \cdot L \cdot t_s^3 \right)} \right]^{0.1} \right] = 0.669$$

type "i"

$A_{bs} := A_{bs} \cdot 2 = 364 \cdot in^2$ $I_{bs} := I_{bs} \cdot 2 = 5126.333 \cdot in^4$ $S := 6.8$

$K_g := \eta \cdot \left(I_{bs} + A_{bs} \cdot e_g^2 \right) = 45257.333 \cdot in^4$ $K_g := 45357$

$$InteriorDFM_1 := \left[0.06 + \left(\frac{S}{14} \right)^{0.4} \cdot \left(\frac{S}{L} \right)^{0.3} \cdot \left(\frac{K_g}{12 \cdot L \cdot t_s^3} \right)^{0.1} \right] = 0.432$$

$$InteriorDFM_2 := \left[0.075 + \left(\frac{S}{9.5} \right)^{0.6} \cdot \left(\frac{S}{L} \right)^{0.2} \cdot \left[\frac{K_g}{\left(12 \cdot L \cdot t_s^3 \right)} \right]^{0.1} \right] = 0.56$$

The calculation process for determining NEXT-D exterior DFMs considering section typologies “i” and “k” required application of the lever rule for both one and two design lanes loaded. The lever rule (figure 108) was employed by assigning a hinge at the center of the interior beams and summing moments about the most exterior hinge (“x”) to calculate the reaction at the center of the exterior beam (“R_A”). Considering the load applied and the moment arms from summing moments about the hinge shown in figure 108, R_A is calculated to be 0.62P. Thus the exterior DFM is 0.62.

The lever rule was calculated considering section typology “i”. The lever rule calculation was not calculated separately for section typology “i” and “k” because for section typology “k”, a hinge would be placed at the first interior web, and this condition would not reflect the load that exists in the first interior web. Thus, the DFM calculated using the lever rule considering section typology “i” is more accurate for the actual load

condition of the webs in the exterior beam, and was deemed acceptable for section typology “k” as well.

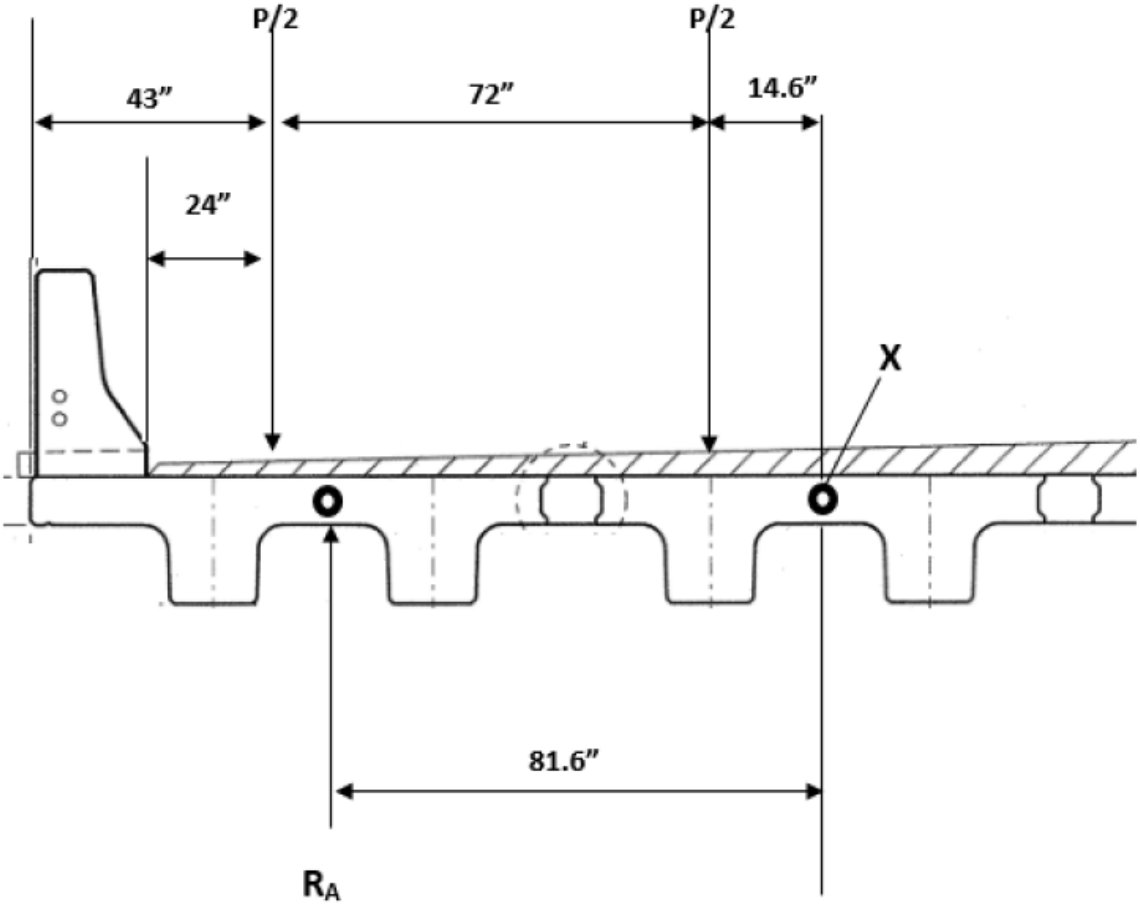

Figure 108: Lever rule application for NEXT-D beams (Filosa, 2017)

Appendix B

Predicted NEXT-D Bending Strain

The NEXT-D girders on the Hanging Rock Creek Bridge span 40 feet. Considering the weight of the heavier truck used in live load test 1 (Filosa, 2017) for the moment calculation, the mid-span NEXT-D girder web bending strain was predicted as follows:

$b_{flg} := 6ft \quad h_{flg} := 8in \quad h_{stem} := 13in \quad b_{stem} := 14in$

$A_{flg} := b_{flg} \cdot h_{flg} = 576 \cdot in^2 \quad A_{webs} := 2 \cdot h_{stem} \cdot b_{stem} = 364 \cdot in^2$

$$y_{bar} := \frac{A_{flg} \cdot 4in + A_{webs} \cdot 14.5in}{A_{flg} + A_{webs}} = 8.07 \cdot in$$

$$I := \left[\frac{3ft \cdot (8in)^3}{12} + 3ft \cdot 8in \cdot \left(y_{bar} - 4in\right)^2 + \frac{14in \cdot (13in)^3}{12} + 14in \cdot 13in \cdot \left(14.5in - y_{bar}\right)^2 \right] \cdot 2 = 32789.24 \cdot in^4$$

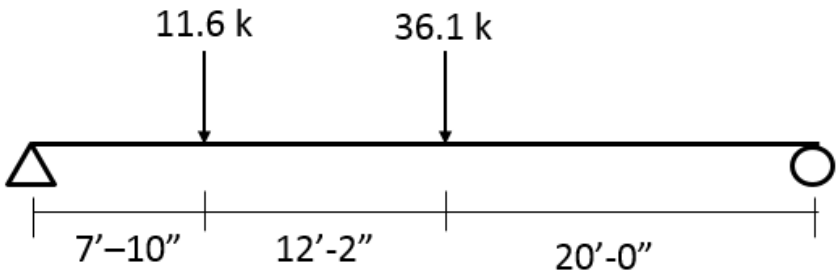

The moment at mid-span is calculated to be>>>>>>>>>>>>>>> $M := 27.38kip \cdot 20ft - 11.6kip \cdot 12.167ft = 406.46 \cdot kip \cdot ft$

$M_{girder} := 0.34 \cdot M = 1658.37 \cdot kip \cdot in$ Maximum interior girder moment distribution factor from LL Test 1 Results (Filosa, 2017)

$$f_{tensile} := \frac{M_{girder} \cdot \left(21in - y_{bar}\right)}{I} = 0.65 \cdot \frac{kip}{in^2} \qquad f_c := 6500psi$$

$$E := 57 \cdot \sqrt{f_c \cdot psi} \cdot 1000 = 4595.49 \cdot \frac{kip}{in^2} \qquad \boxed{\mu\varepsilon := \frac{f_{tensile}}{E} \cdot 1000000 = 142.35}$$

Appendix C

Predicted NEXT-D Neutral Axis Location and Predicted Shear Strain

The NEXT-D girder web neutral axis (from the top of the section) was predicted as shown below. The girder reinforcement was neglected in the calculation.

$$A_{flg} := b_{flg} \cdot h_{flg} = 576 \cdot in^2 \qquad A_{webs} := 2 \cdot h_{stem} \cdot b_{stem} = 364 \cdot in^2$$

$$y_{bar} := \frac{A_{flg} \cdot 4in + A_{webs} \cdot 14.5in}{A_{flg} + A_{webs}} = 8.07 \cdot in$$

Considering the weight of the heavier truck used in live load test 1 (Filosa, 2017) for the shear calculation, the NEXT-D girder web shear strain at two feet from the face of the support was predicted as follows:

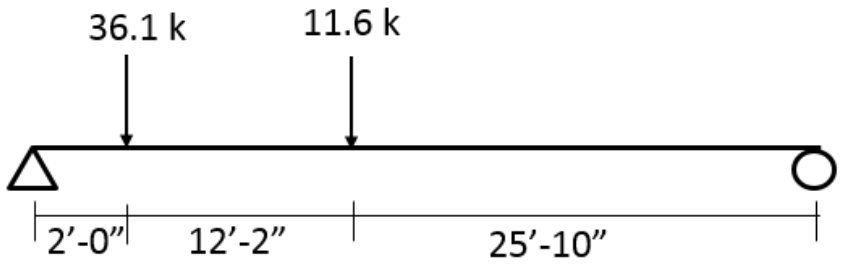

$V_{LL} := 41.8kip$ Use 0.4 as Distribution Factor (Estimate Considering DFMs from Previous LL Tests (Filosa, 2017))

$V_{beam} := V_{LL} \cdot 0.4 = 16.72 \cdot kip$

$A_{flg} := 6ft \cdot 8in = 576 \cdot in^2$ $A_{webs} := 2 \cdot 13in \cdot 14in = 364 \cdot in^2$

$$y_{bar} := \frac{A_{flg} \cdot 4in + A_{webs} \cdot 14.5in}{A_{flg} + A_{webs}} = 8.07 \cdot in$$

$$Q := A_{flg} \cdot (y_{bar} - 4in) + (y_{bar} - 8in) \cdot 14in \cdot \left(\frac{y_{bar} - 8in}{2}\right) \cdot 2 = 2342.05 \cdot in^3$$

$$I := 2\left[\frac{3ft \cdot (8in)^3}{12} + 3ft \cdot 8in \cdot (y_{bar} - 4in)^2 + \frac{14in \cdot (13in)^3}{12} + 14in \cdot 13in \cdot (14.5in - y_{bar})^2\right] = 32789.24 \cdot in^4$$

$t := 30in$ (Two times the width of a web)

$$\tau := \frac{V_{beam} \cdot Q}{I \cdot t} = 0.04 \cdot \frac{kip}{in^2}$$ $G := 3 \cdot 10^6 \frac{lbf}{in^2}$ Estimated Shear Modulus of Concrete

$$\mu\varepsilon := \frac{\tau}{G} \cdot 1000000 = 13.27$$

Appendix D

LL Test 2 Additional Figures and Thermal Strain Estimate

The results LL test 2 for sensors LST-01, LST-03, LST-04, LST-06, and LST-10 are shown below.

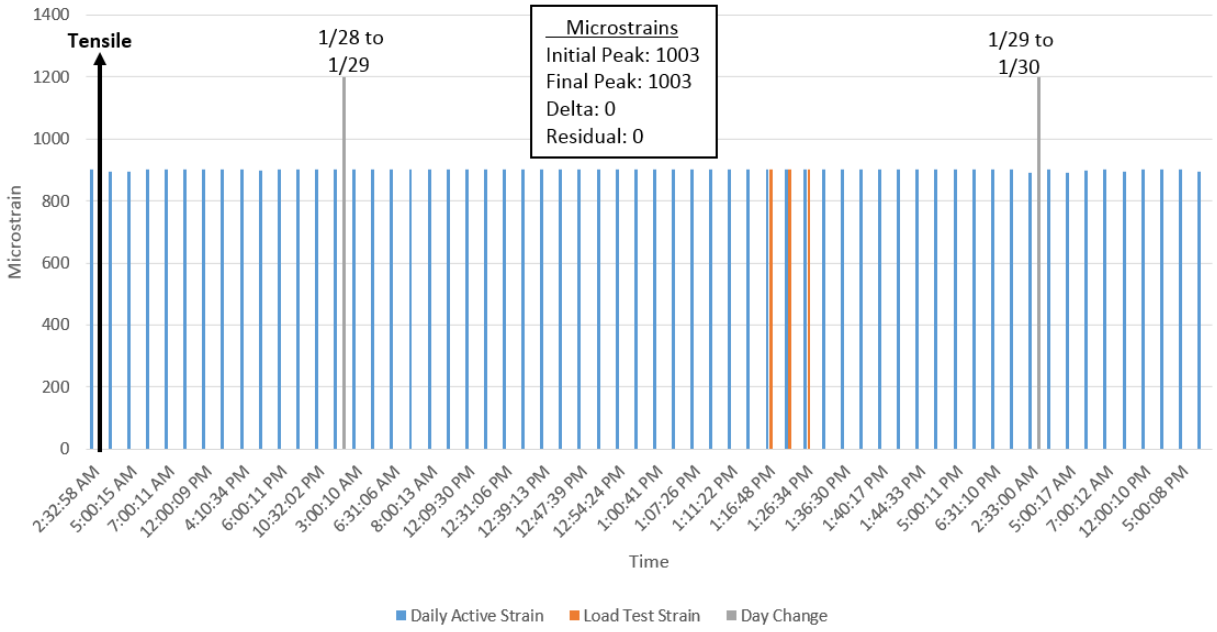

Figure 109: Load test results of sensor LST-01

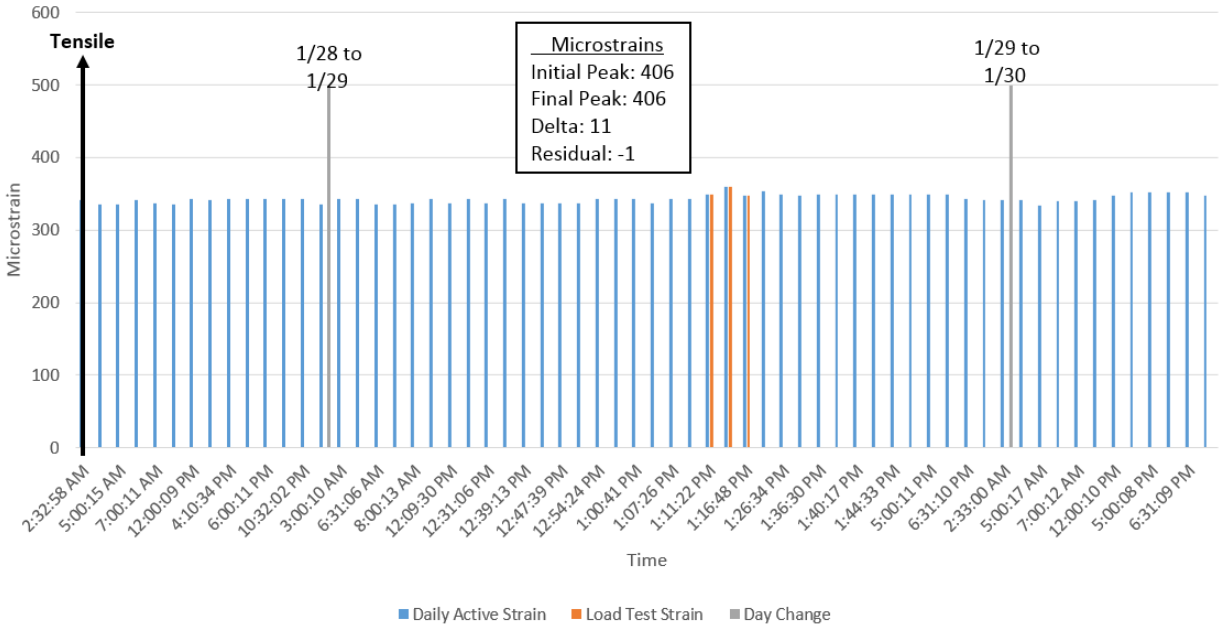

Figure 110: Load test results of sensor LST-03

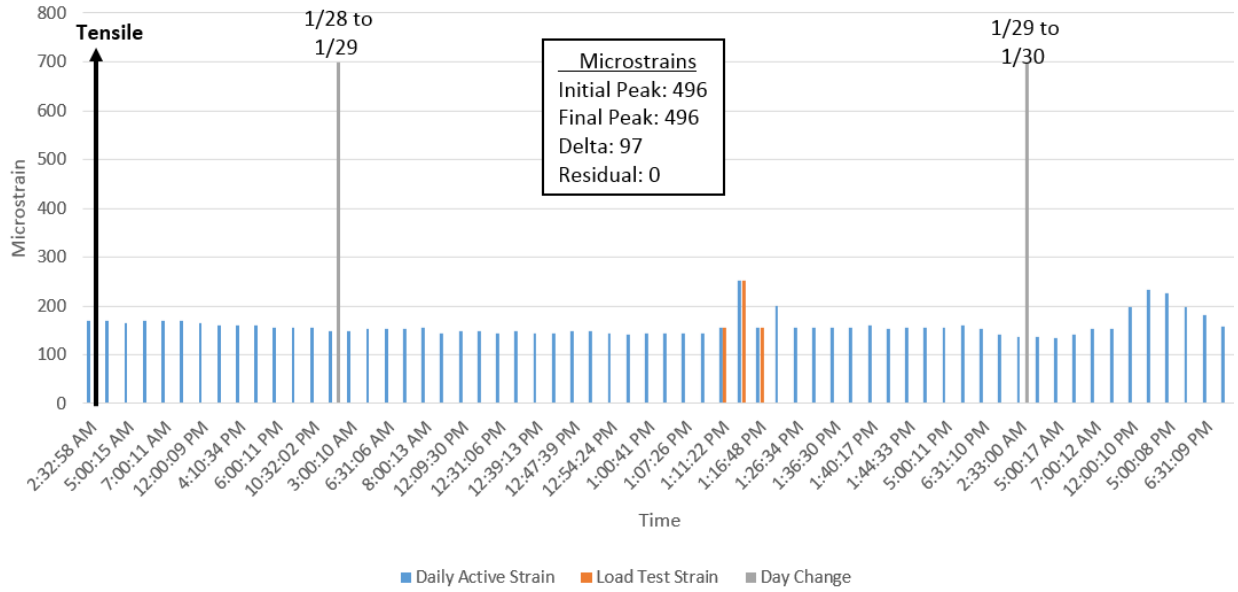

Figure 111: Load test results of sensor LST-04

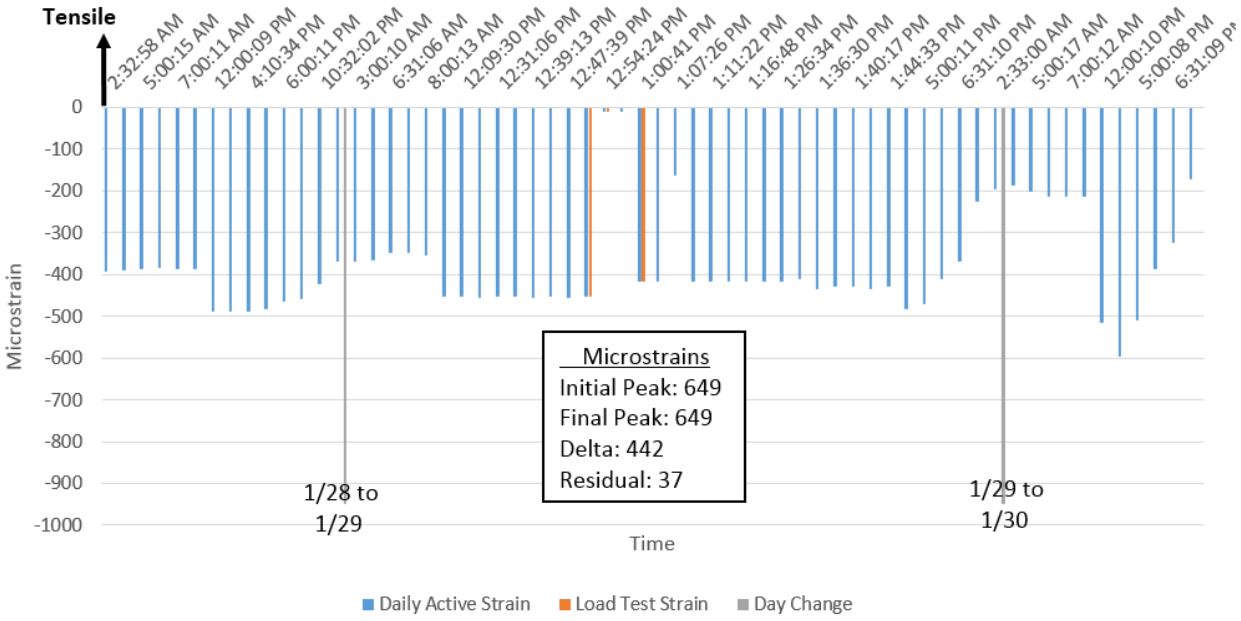

Figure 112: Load test results of sensor LST-06

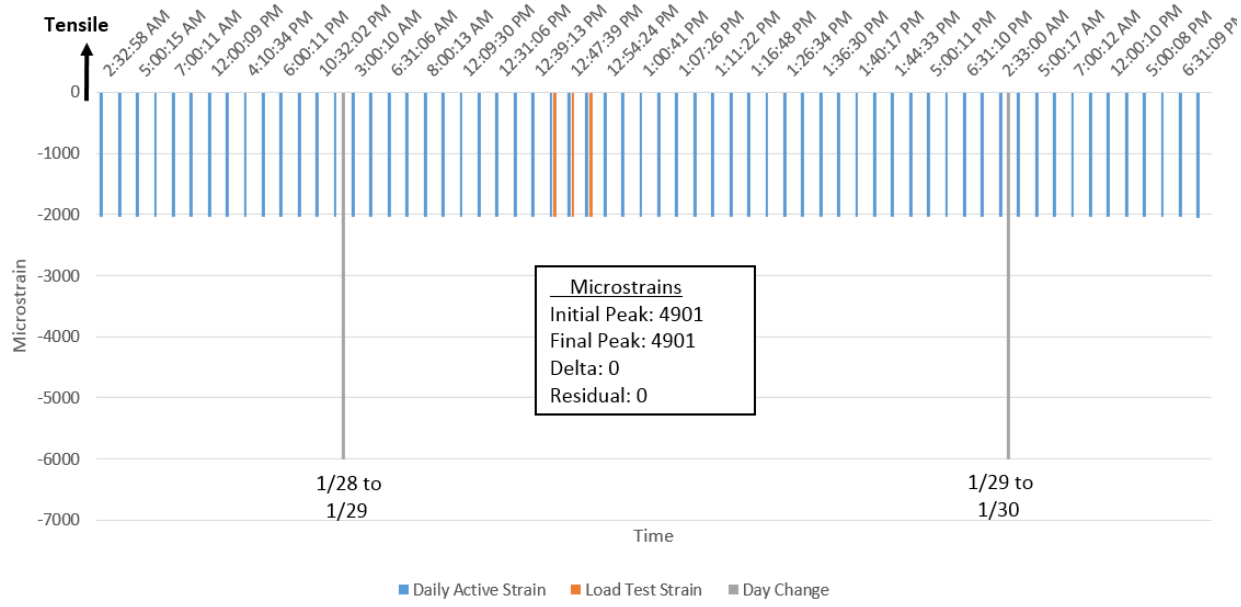

Figure 113: Load test results of sensor LST-09

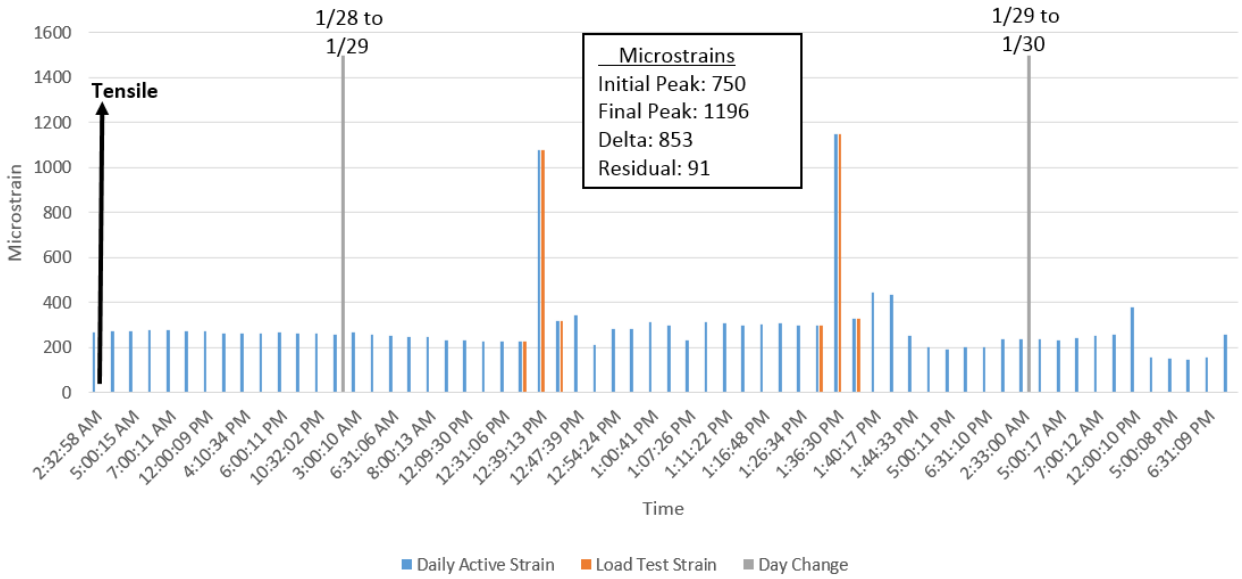

Figure 114: Load test results of sensor LST-10

Thermal Strain Estimate:

Coefficient of Thermal Expansion (COE) = $7.3*10^{-6}$ (Portland Cement....: Federal Highway)

Estimated Temperature Change for Kershaw, SC (T) = 100°

$\varepsilon = (COE)*T = (7.3*10^{-6})*(100°) = 730\mu\varepsilon$

Appendix E

September 2018 Photo Survey

Bridge Deck Photo Survey (all deck photos facing south)

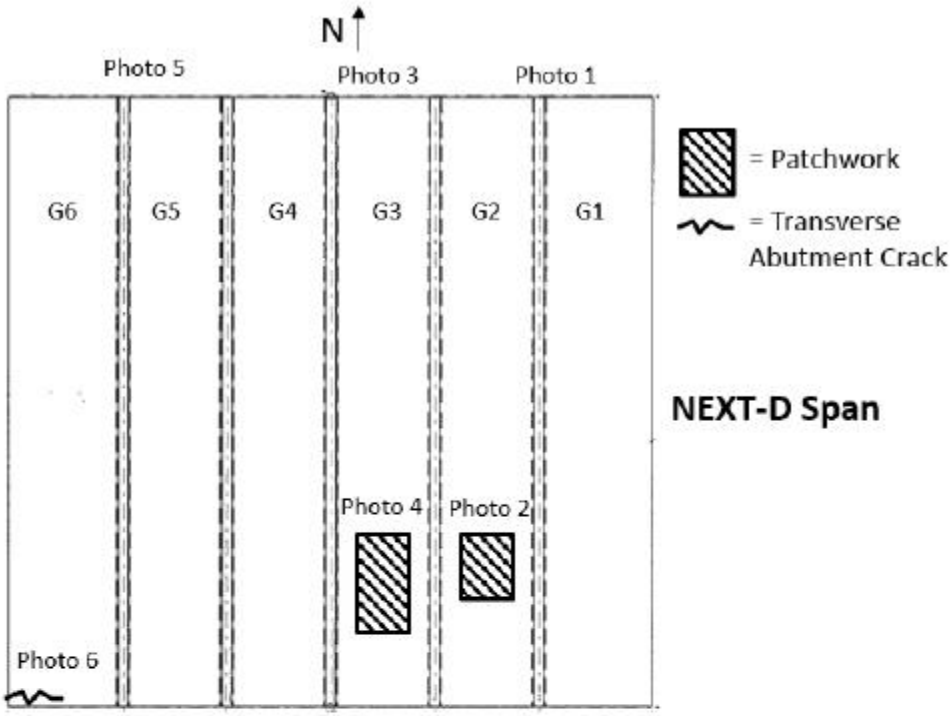

Photo 1

Photo 2

Photo 3

Photo 4

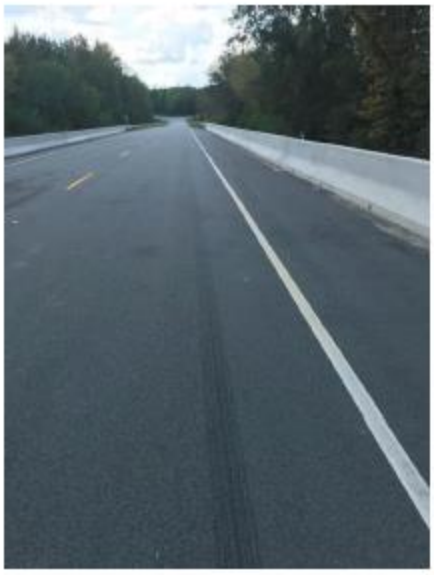

Photo 5

Photo 6

Photo 7

Photo 8

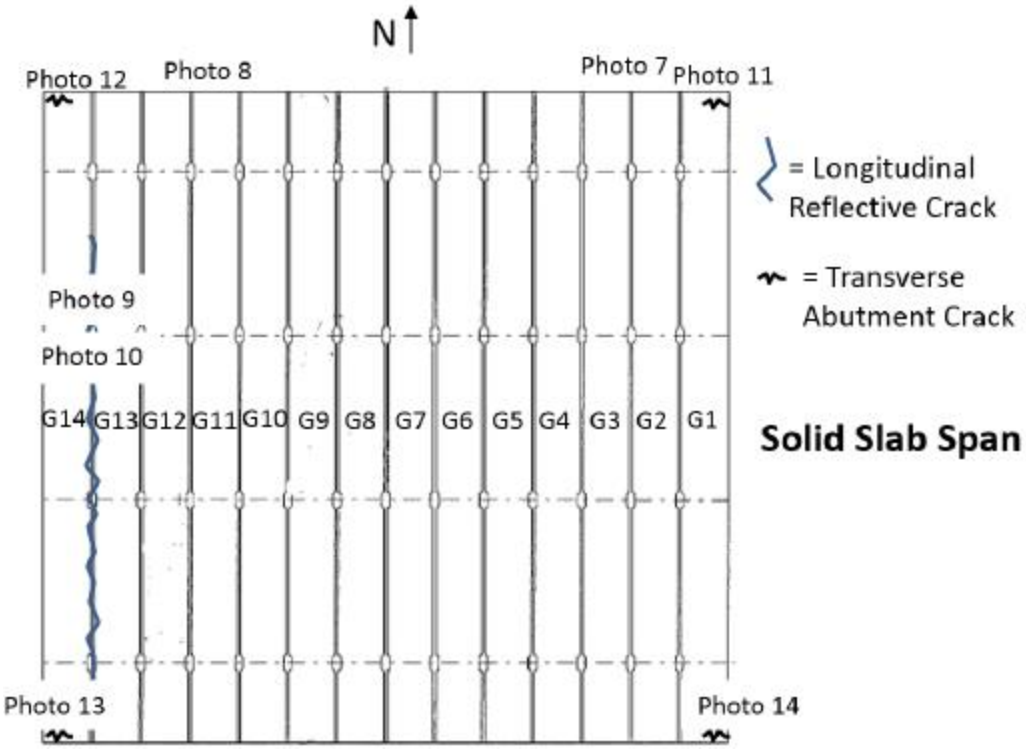

Photo 9

Photo 10

Photo 11

Photo 12

Photo 13

Photo 14

Bridge Underside Photo Survey

Photo 15: NEXT-D girder 6 facing north

Photo 16: NEXT-D girder 6 facing south

Photo 17: NEXT-D joint between girders 5 and 6

Photo 18: Solid slab girder 14 facing south

Photo 19: Solid slab girder 14 facing north

Photo 20: Solid slab joint between girders 13 and 14

Works Cited

AASHO LRFD Bridge Design Specifications. Washington: AASHTO, 2012. Print.

AASHTO LRFD Bridge Design Specifications. Washington: AASHTO, 2014. Print.

"A Guide to Important National Bridge Inventory Terms." *The National Bridge Inventory Database*. N.p.: 2018. Web 31 May 2018.

Barker, Richard M., and Jay A. Puckett. *Design of Highway Bridges: An LRFD Approach*. Hoboken, N.J.: Wiley, 2007. Print.

Boresi, A. P., & Smith, R. J. (2003). *Advanced mechanics of materials* (6th ed.). New York: Wiley.

"Bridges." *ASCE's 2017 Infrastructure Report Card.* N.p.: 2017. Web. 31 May 2018.

Chajes, Michael, Harry Shenton, and Dennis O'Shea. (2000). "Bridge-condition Assessment and Load Rating Using Nondestructive Evaluation Methods." *Transportation Research Board: Journal of the Transportation Research Board*, Vol. 2, No. 1696, 83-91. Web.

Culmo, Michael P., and Rita L. Seraderian. "Development of the Northeast Extreme Tee (NEXT) Beam for Accelerated Bridge Construction." *PCI Journal* (2010): 86-101. Summer 2010. Web. 18 December 2017.

"Deficient Bridges by Highway System 2017." *US Department of Transportation Federal Highway Administration*. N.p.: 2018. Web 31 May 2018.

Dreery, Daniel Patrick. *Investigation of Northeast Extreme Tee (NEXT) D Beam Bridges as an Alternative to Precast Hollow Core Bridges: An Exploration of Appropriate Slab Design Forces*. Thesis. Clemson University, 2010. N.p.: n.p., n.d. Print.

Dymond, Benjamin C. *Shear Distribution in Prestressed Concrete Girder Bridges*. Dissertation. University of Minnesota. 2015. N.p.: n.p., n.d. Print.

Filosa, Francis Vincent. *Live Load Distribution Factors and UHPC Shear Key Performance of SCDOT NEXT D Beam and Solid Slab Bridges*. Thesis. Clemson University, 2017. N.p: n.p., n.d. Print.

Fu, C.C., Elhelbawey, M., Sahin, M.A., and Schelling, D.R. (1996). "Lateral Distribution Factor from Bridge Field Testing." *Journal of Structural Engineering*, Vol. 122, No. 9, 1106-1109.

Fu, C.C. "Introduction of Non-Destructive testing [Powerpoint]." *Department of Civil & Environmental Engineering. University of Maryland College, Park*. n.d.: n. pag. Web. 25 June 2018.

"Guidelines for Northeast Extreme Tee Beam." *PCI Northeast* (2012): n. pag. 2012. Web. 5 June 2018.

Graybeal, Benjamin A. "Behavior of Ultra-High Performance Concrete Connections between Precast Bridge Deck Elements". CBC (2010): n. pag. Web. 21 June 2018.

Halbe, Kedar Ram. *New Approach to Connections between Members of Adjacent Box Beam Bridges.* Dissertation. Virginia Polytechnic Institute and State University, 2014. N.p.:n.p.,n.d. Print.

Hartle, Raymond A., Balan, Toader A., Wingate, Frank B. "Remote Health Monitoring and Load Modeling of Cracked Fracture Critical Bridge Components." FHWA-PA-2006-036-040207-1 (2006): n. pag. March 2007. Web. 20 Dec. 2017.

Idriss, R and Z. Liang (2010). "In-Service Shear and Moment Girder Distribution Factors in Simple-Span Prestressed Concrete Girder Bridge." *Transportation Research Record: Journal of the Transportation Research Board* 2172(-1): 142-150.

Joyce, Patrick C. *Development of Improved Connection Details for Voided Slab Bridges*. Thesis. Virginia Polytechnic Institute and State University, 2014. N.p.: n.p., n.d. Print.

Kassner, Bernard L. *Shear Strength of Full-Scale Prestressed Lightweight Concrete Girders with Composite Decks*. Dissertation. Virginia Polytechnic Institute and State University, 2012. N.p.: n.p., n.d. Print.

Moore, Mark., Rolander, Dennis., Graybeal., Phares, Brent., Washer, Glenn. "Highway Bridge Inspection: State-of-the-Practice Survey." *FHWA* FHWA-RD-01-033 (2001): n. pag. April 2001. Web 21 June 2018.

Neely, W. Douglas, Thomas E. Cousins, and John L. Lesko. "Evaluation of In-Service Performance of Tom's Creek Bridge Fiber-Reinforced Polymer Superstructure." *Journal of Performance of Constructed Facilities* 18.3 (2004): 147-58. Web. 25 June 2018.

"Northeast Extreme Tee Beam Guidelines." *PCI Northeast* (2017): n. pag. 2017. Web 31 May 2018.

Nowak, A.S. (1993) *Calibration of LRFD Bridge Design Code—NCHRP Project 12-33*, University of Michigan, Ann Arbor, MI.

"Portland Cement Concrete Pavements Research." *Federal Highway Administration* (n.d.): n. pag. Web. 11 October 2018.

"Rebuilding our Roads." *South Carolina Department of Transportation*. N.p.: n.d. Web 31 May 2018.

Seraderian, Rita L. "Northeast Extreme Tee Beam [Powerpoint]." *PCI Northeast* (2016): n. pag. 2 Feb. 2016. Web. 18 December 2017.

Sharpe, G.P. (2010). Reflective cracking of shear keys in multi-beam bridges. *Masters Thesis*, Texas A&M University.

Sheng, Huan, Bryant G. Nielson, Weichiang Pang, and Scott D. Schiff. "Precast Alternative for Flat Slab Bridges." *Home – Transport Research International – TRID*. N.p., 30 Sept. 2013. Web. 13 June 2017.

Smolenski, Peter J. *Field Instrumentation and Live load Testing to Evaluate Behaviors of Three Reinforced Concrete Bridge Decks*. Thesis. Montana State University, 2004. N.p.: n.p., n.d. Print.

Wight, James K. *Reinforced Concrete: Mechanics and Design*. London, U.K.: Pearson, 2016. Print.

Yang, Y. and Meyers, J.J. (2003). "Live-Load Test Results of Missouri's First High-Performance Concrete Superstructure Bridge." *Transportation Research Board: Journal of the Transportation Research Board*, No. 1845. 96-103.

Zoakie, T., T.A. Osterkamp, and R.A. Imbesen (1991). *Distribution of Wheel Loads on Highway Bridges, Final Report Project 12-26/1, National Cooperative Highway Research Program*, Transportation Research Board, National Council, Washington, DC.